

POLITECNICO DI TORINO

MASTER's Degree in ENERGETIC ENGINEERING



MASTER's Degree Thesis

Preliminary redox assessment study on
double perovskite structure

$Sr_2FeNi_{0.4}Mo_{0.6}O_{6-\delta}$ by experimental
investigation in TGA and microreactor

Supervisors

Prof. MASSIMO SANTARELLI

Dr. DOMENICO FERRERO

Dr. SALVATORE CANNONE

Candidate

MARCO DEQUINO

MARCH 2021

Summary

The ever-increasing demand for energy is generating a consequent increase of the energy production in the years to come. This currently comes mostly from power plants that use fossil fuels as their main fuel. Natural gas or coal-based power plants continue to improve from the point of view of efficiency, reducing emissions and wastes per unit of energy more and more. With a view to following international agreements in limiting the rise in global average temperatures, mitigation actions against CO_2 emissions are becoming increasingly fundamental. Carbon capture and further uses are one of the leading themes of scientific research, especially when retrofitting pre-existing plants. A possible route consists in chemical looping processes that involve the use of an oxygen carrier that alternates between a reduced state and an oxidized state creating a syngas as a useful product. Metal oxides are the family of materials that is more used in chemical looping processes, but recently many studies have been conducted to find alternatives that can achieve better performance in terms of CO_2 capture and consequently higher syngas yields. These materials must avoid deactivation problems that are common during redox cycle processes. Carbon deposition creates a surface layer that prevents oxygen ions from penetrating inside the matrix and thus occupying the vacancies previously created in the reduction step. Perovskites have a structure very favorable to the transport of oxygen, especially if in the presence of doping that weakens the link between B-sites and oxygen allowing the greater creation of vacancies. It has been seen that working with a sub-stoichiometric structure further favors this process. Doping in B sites results in exsolution phenomena on cations by moving from the bulk to the surface thus increasing performance and acting as a catalyst for CO_2 capture. This thesis presents the first results obtained on a new material with composition $Sr_2FeNi_{0.4}Mo_{0.6}O_{6-d}$ (SFNM04) through TGA tests and subsequent microreactor

tests. It can be seen from the first results how the effect of CO_2 is evident in the oxidation stage, but still reversible in the presence of a reductive atmosphere with hydrogen. Nevertheless, the material present problems related to the formation of carbonates with an oxidating environment in the simultaneous presence of carbon compounds such as CO_2 at different concentration. Post-mortem analysis of the sample shows the presence of strontium carbonate formation $SrCO_3$ and strontium molybdate $SrMoO_4$. The first inhibits the carbon monoxide formation as it is created from the interference of the CO_2 molecule with the SrO oxide. The second phase, has insulating characteristics, generally inhibiting the re-oxidation of the material. These compounds were seen disappearing by subjecting the material to air treatment at 800 °C for one hour. The formation of Fe-Ni alloys by exsolution phenomena has only been achieved for reductions in H_2 perpetuated for more than 30 minutes in TGA. This suggests that more time is needed to allow the Fe^{3+} and Ni^{3+} ions to be reduced to Fe^{2+} and Ni^{2+} and exsolve on the surface of the sample catalyzing the oxidation. In conclusion, this work is part of a preliminary study to determine the reproducibility of redox cycles for SFNM-04 perovskite and to form the basis of information for more in-depth and targeted analysis with the prospect of opening new pathway towards systems with less expensive materials.

To everyone who, in any way, has helped and supported me in this work.

Thank you.

Table of Contents

List of Tables	IX
List of Figures	X
Acronyms	XVIII
1 Introduction	1
1.1 The problem of carbon dioxide and the Chemical Looping solution .	1
1.2 Material for Chemical Looping CO_2 reuse	7
2 Literature review	10
2.1 Carbon capture, storage and sequestration	10
2.2 The use of carbon dioxide in chemical looping	15
2.3 Chemical looping processes for the dissociation of CO_2 and H_2O or carbonaceous fuels	20
2.3.1 Carbon formation in chemical looping processes	24
2.4 Different types of oxygen carriers	26
2.4.1 Phase-changing metal oxide (volatile)	27
2.4.2 Non-volatile oxygen carrier	28
3 Experimental Methods	50
3.1 Thermogravimetry Analysis (TGA) method	50
3.1.1 Components for the measure of mass	51
3.1.2 Components for the temperature measurement	54
3.1.3 Reliability of the data collected in during the TGA	54
3.1.4 Gas Spectrometer included in the bench setup	57

3.1.5	TGA setup created for this study work	59
3.1.6	Characterization of the material through TPR and TPO analysis	59
3.2	Microreactor setup with Gas Analysis method	61
3.2.1	The furnace	63
3.2.2	Data collection through Gas Analyzer	65
3.2.3	Data collected in the microreactor setup	71
3.2.4	X-ray diffraction (XRD) analysis (post-mortem analysis) . .	73
4	Presentation and discussion of the results	75
4.1	SFNM-04 as new material for chemical looping application	75
4.2	Experimental analysis: TG characterization	81
4.2.1	Test WHITE1: white curve of the crucible	81
4.2.2	Test PRE1: Air pre-treatment of the first sample	82
4.2.3	Test TPR1: single TPR of the pre-treated sample	84
4.2.4	Test TRP4-air: 4 consecutive cycles with re-oxidation in air	85
4.2.5	Test TPR4-50% CO_2 : 4 consecutive cycles with re-oxidation in CO_2 at 50%vol	87
4.2.6	Test TPR10: 10 consecutive cycles after pre-treatment of a new sample	94
4.2.7	Test TPR6-oxy: 6 cycle with a final longer oxidation	103
4.2.8	Test TPR6-oxy/red: 6 cycle with a final longer oxidation and subsequent reduction	105
4.3	XRD analysis post-mortem of the TG tested samples	109
4.4	Experimental analysis: microreactor characterization	114
4.4.1	Test S1: TPR with isothermal CO_2 oxidation	114
4.4.2	Test S2: Isothermal redox at 850°C with CO_2 oxidizing environment at 20% vol	116
4.4.3	Test S3: Isothermal test with oxidation in wet environment with 50% H_2O molar fraction	118
4.5	XRD analysis of samples tested in micro-reactor	121
5	Summary of the results and further considerations	125
5.1	Resume of the result obtained	125

5.2 Comparison with similar material tested in literature	127
6 Conclusion and future prospects	131
Bibliography	135

List of Tables

4.1	Summary table of tests conducted in TGA.	81
4.2	Mass variation of SFNM from figure 4.12 summarized.	91
4.3	Resume of the values of mass change during the reduction and oxidation steps of the 10-loop test. The first reduction and oxidation has not been considered.	98
4.4	Delta of mass in [mg] of reduction and oxidation steps. Is included the final longer oxidation in segment 5 with a noticeable higher number.	104
4.5	Variation of mass in the last oxidation and subsequent reduction segments.	106
4.6	Summary table of the three microreactor tests conducted.	114

List of Figures

1.1	CO_2 capture capacity currently on market. Data elaborated from [12].	4
1.2	Representation of the kaya index together with its indicators.	5
1.3	Carbon dioxide emission in Italy differentiated by sectors. Data elaborated from [14].	6
1.4	Forecasts of the development of carbon capture and storage technologies in the future according to two different scenarios. Case a) development of the clean technology scenario; case b) development of the reference technology scenario. Data elaborated from	7
2.1	Representation by power and year through historical progression of oxyfuel combustion plants from small scale pilot up to large scale [28]. The plants with the presence of capture systems are highlighted in red, while the blue ones are exclusive to carbon capture systems.	12
2.2	Converter unit for direct solar reduction of CO_2 [36]. The gas path is indicated by the arrow as well as the jet feed injection is shown. .	16
2.3	Example of chemical looping made by three reactors with recirculation of the oxygen carrier.	17
2.4	Example diagram of the possible catalyst regeneration procedure in an FCC process	19
2.5	Schematic image representing the reduction mechanism of a perovskite with methane as reductant [39].	22
2.6	Representation of the mole fraction of CO_2 and CO in the Boudouard equilibrium as function of temperature.	25

2.7	Zinc oxide reactor for water splitting and hydrogen production. . .	28
2.8	Fe_2O_3 oxidation pathways. Starting from the diffusion-limited regime (a), upon the magnetite start to segregate or $\gamma - Fe_2O_3$. Then in (c) is shown the transition to the nucleation-limited regime, ending with (d) where the oxidation result in hematite $\alpha - Fe_2O_3$ [50].	29
2.9	Representation of the ideal cubic perovskite structure. Left (a) shows a 3D representation; right (b) shows representation on a plane. Spheres represent A-site cations. B-site cations are placed inside the octahedral shapes [52].	31
2.10	Generation rate-time of CO at 1100°C for the perovskite $LaFe_xCo_{1-x}O_3$ at 25%wt on SiO_2 with x=0.5,0.7,0.9,1 [53].	34
2.11	Evolution of production of oxygen (a) and hydrogen (b) of the perovskite $La_{1-x}Sr_xMnO_{3-\delta}$ with different concentration of Sr [54]. Different peaks were positioned in series on a x-axis to have better comparison of the time needed for each reaction to occur.	36
2.12	Evolution of oxygen in perovskite $La_{0,5}Sr_{0,5}MnO_3$ and $La_{0,5}Ca_{0,5}MnO_3$ [55].	37
2.13	H2-TPR results of different perovskites studied by [57].	39
2.14	Results of different TGA test of $La_{1-y}Ca_yNi_{0,9}Cu_{0,1}O_3$ performed in H2-TPR [57].	40
2.15	Mass change and DTG plot of perovskite $La_{1,6}Sr_{0,4}FeCoO_6$ from [58].	41
2.16	Temperature programmed reduction in H_2 (a), followed by temperature programmed oxidation in CO_2 (b) [59].	42
2.17	Production rates of CO measured in oxidation at 40% CO_2 in volume at 1000°C. All the sample where thermally reduce in He atmosphere at 1350°C. The numbers in the parenthesis represent the total amount of the production [67].	44
2.18	Total amount of CO produced in each cycle for SLMA2 with a reduction at 1350°C in He and oxydation in 40% CO_2 in volume at 1000 °C. Each reduction and subsequent oxydation lasts for a total time of 30 minutes divided in 15 min for reduction and 15 min for oxidaiton.	45

3.1	Mechanism of the balance inside the TG instrument STA 2500 Regulus [73].	52
3.2	Crucibles positioned upon the plates. Thermocouples are under the sample holder in contact with it.	53
3.3	STA Regulus 2500 machine.	55
3.4	Gas Analysis Spectrometer QGA from Hiden Analytical.	58
3.5	Scheme of the setup created for the TG analyses.	60
3.6	Microreactor setup scheme with the gas lines connected to the main stream. Note the two three-way valves: the first for choosing flow in the reactor rather than in the hood, the second determines the choice between dry flow or wet flow.	62
3.7	On the left, bench setup with with the Carbolite Gero furnace as core componente. On the right, power conditioning unit and temperature sequences controller	63
3.8	SFNM sample under the Al_2O_3 crucible before been inserted in the center of the tubular furnace.	64
3.9	Inside overview scheme of the furnace Carbolite Gero [78].	65
3.10	Classification of gas sensing methods by [79]	66
3.11	Electronic scheme of a TCD detector. Figure taken from the site at the bottom left of the image.	67
3.12	Typical differences between the filament temperature and the detector block temperature [82].	69
3.13	Calibration point correlated with a 1st order equation.	72
3.14	On the left: representation of the distances $\lambda/2$ between the atom in the lattice and the perpendicular line to the x-ray beam direction. On the right: representation of the main parameters that determine the Bragg's Law.	74
4.1	Scheme of the Ruddlesden-Popper perovskite structure with diferent numbers of ABO_3 cubic layer covered by a rock-salt structure [88].	76
4.2	XRD spectra of the as synthesized SFNM-04 sample.	77
4.3	First analysis with 4 subsequent reduction and oxidation cycles. [76].	78

4.4	(a) XRD spectra of SFNM-04 sample after different cycles in order to assess the evolution of the phase in a reductive environment. (b) Identification in detail of the SFNM-04 after 4 cycles. It is possible to notice a magnification image in 43° and 45°	79
4.5	White curve of the platinum crucible in TGA until 900°C	82
4.6	Air pretreatment of the first sample until 900°C for the complete oxidation of the SFNM material.	83
4.7	First TP-Reduction experiment in $H_2 1\%/N_2$ in temperature ramp from 500°C to 900°C	85
4.8	4 consecutive cycles of TPR and subsequent re-oxidation in air environment. During the first loop are highlighted the reduction and oxidation steps separated by argon flow during the temperature swing.	87
4.9	hydrogen reacted as function of temperature during the TPR in: a) 1st cycle; b) 2nd cycle; c) 3rd cycle; d) 4th cycle.	88
4.10	Overlapping of the hydrogen reacted in all the 4 cycles performed in TPR.	89
4.11	Maximum oxygen released for each cycle. Calculated considering the best rate of hydrogen consumed.	90
4.12	Mass variation of SFNM sample during the 4 cycles with reoxidation at $50\%CO_2$ vol.	90
4.13	Hydrogen reacted for each cycle performed during the 4-loop test with CO_2 at $50\%\text{vol}$ in oxidation step.	91
4.14	Trend of hydrogen reacted in the 4-loop cycles test with $50\%\text{vol } CO_2$ overlapped. No such increment in reaction is shown between the 2nd and 4th cycle.	92
4.15	Comparison of the 4th and 5th TGA test by overlay the mass-change curves. The CO_2 oxidation curve is shifted with respect to the air oxidation ones because of the different behaviour performed. red sample mass was already pre-treated before the TG experiment, while the blue sample mass has seen firstly a pre-treatment in air at 500°C	93
4.16	Peak of possible CO production taking as hypothesis that the change of mass is indeed oxygen lattice acquisition by CO_2 splitting.	94

4.17	Pre-treatment of the sample mass before the 10 cycles test. The sample gain 1% in mass after the TPO in CO_2 environment.	95
4.18	Mass variation during the 10 cycles test performed in TGA. The number refers to the % of mass evaluated in each end of reduction and oxidation, with respect to the initial sample mass.	97
4.19	Total hydrogen reacted in [ml] for each reduction segment of the 10 cycles test.	98
4.20	H_2 reacted in all the 10 cycles. Curves are superposed to evidence the difference between the reduction segments.	99
4.21	Hydrogen reacted in each reduction step of the 10-loop cycle test with 20% CO_2 in oxidizing environment.	100
4.22	Estimation of the maximum rate of oxygen lost for each gram of perovskite material. On the left y-axis there is the corresponding maximum rate of hydrogen consumed, again per unit mass of the sample. Data refers to the sixth TGA test with 10 cycles.	101
4.23	Estimation of peak CO production in each oxidation of the 10-cycle redox cycles. Calculation determined by the assumption that all of the initially acused mass is driven by an accumulation of oxygen in the lattice.	102
4.24	Mass % as function of time in the 6 cycles test with longer final oxidation (Seventh TGA experiment). The curve increase finally with the longer exposure of the sample in the oxidising environment. The number are captured at the end of each segment both reduction and oxidation ones.	104
4.25	6 cycles of TPR and TPO followed by a long oxidation always with $CO_2@20\%$ at $500^\circ C$ and a last reduction in $H_2(1\%)/N_2$ flow in temperature ramp until $900^\circ C$. Picture refers to the Eighth TGA experiment.	105
4.26	Hydrogen reacted in each reduction step of the 6-cycles test with last longer oxidation and subsequent reduction with 20% CO_2 in oxidizing flow. The last picture shows almost doubled consume of the H_2 by the sample mass.	107

4.27	H_2 reacted in all the cycles of the eighth TGA test. The overlay shows how the first cycle is out of temperature range compared to the following ones. The last reduction lasts for a longer time and consequently for a much higher temperature range reaching almost 800°C before the reaction tail.	108
4.28	XRD peaks of the fresh SFNM-04 sample as synthesized.	109
4.29	XRD curves of the first trio of samples tested. On the right is highlighted the peak of the main perovskite structure common to every sample. This indicates that the primary structure is maintained and does not change during testing.	110
4.30	XRD curves of the first trio of samples tested a). While b) is a zoom on the 44-45° where peak attributed to Ni-Fe alloy should present.	111
4.31	XRD curves of the first trio of samples tested a). While b) is a zoom on degrees where strontium molybdate should be seen.	112
4.32	XRD curves of the second trio of sample analyzed. With the (+) sign is highlighted the good behavior of the material corresponding to the formation of FeNi alloy. Unlike, the (-) sign shows the formation of $SrMoO_4$ in all the three sample showed.	113
4.33	Reading value from spectrometer in ppm. the sampling from 40 to 85 regards the bypass section of the gas and the stabilization of the signal near 2200 ppm taken as 0 value. The convexity of the curve indicates the time when the flow returns to the reactor where only Argon atmosphere had previously remained. After sampling 97, one would expect a spike in CO produced.	117
4.34	sampling of two successive reductions and oxidations at 5% H_2/N_2 and 50% mol of H_2O , respectively. One can see the reductive steps where hydrogen settles at about 5000 ppm. No particular hydrogen production activity due to water splitting was detected in oxidation.	120
4.35	XRD signal of the Sample S1 after the emulation of the TGA condition in the micro-reactor setup.	122
4.36	XRD data of the Sample S2. This sample has seen 2 isothermal redox loop at 850°C with oxidation in CO_2 environment at 20%.	123

4.37	XRD analysis of Sample S3 and S4. Both present similar trend of the data-curves which correspond to the peaks of the fresh-SFNM sample as synthesized.	124
5.1	Diagram of the transformations that occurred in the material in the reducing phase. The segregation of molybdate is not considered. . .	128
5.2	Comparison of weight lost in TPR by materials tested in [91] versus tests performed in TGA in this thesis work. The 10-cycle test, the 4-cycle test (both with oxidation in the presence of CO_2), and the 4-cycle test with oxidation in air were chosen.	129

Acronyms

SFNM

Strontium-Iron-Nickel-Molibdenum perovskite

TGA

Thermogravimetry Analysis

DTA

Differential thermal analysis

MFC

Mass flow controller

TPR

Temperature programmed reduction

TPO

Temperature programmed oxidation

UNIUD

University of Udine

SOFC

Solid oxide fuel cell

PCU

Power conditioning unit

TCD

Thermal conductivity detector

FID

Flame ionization detector

IR

Infrared detector

SMR

Steam methane reforming

LSM

Lanthanum-Strontium-Manganate perovskite

TCES

Thermochemical energy storage

EOR

oil recovery

ASU

Air separation unit

MEA

Monoethanolamine

CLC

Chemical looping combustion

FCC

Fluid catalytic cracking

P2G

Power to gas

CLR

Chemical looping reforming

WGS

Water gas shift

BET

Brunauer-Emmett-Teller number

TRL

Technology readiness level

Chapter 1

Introduction

1.1 The problem of carbon dioxide and the Chemical Looping solution

Anthropogenic CO_2 emissions, derived from the burning of fossil fuels, have long been recognized as one of the major contributions to climate change with an emission projection of 30.6 Gt of CO_2 issued in 2020 [1]. Despite being a lower figure than in previous years, the world governments still have to work hard to reverse the growth trend. The good news is that the price of renewable energy, together with substantial investments, is leading to a greater role for renewable sources in the energy sector. However, from the studies we can notice that the role of sources remains firmly anchored in the overall energy landscape [2]. So, although it can be said that the global trend is declining, it should not be confused with the impressive role that fossil sources continue to play, especially in developing countries. It is also pointed out that, among the major sources of CO_2 emissions into the atmosphere, the plants dedicated to energy production are among the most emissive, followed by the transport sector. In this respect, large-scale industrial processes will increasingly be targets for the development of applications for carbon dioxide capture. Captured CO_2 can be reused through new technologies that see their possible application in a retrofit context from pre-existing industrial plants. Indeed CO_2 can be a protagonist in the market in this regard. It can be adopted in the context of carbon capture and utilization (CCU), as a source of carbon for

the production of synthetic hydrocarbons. Redox chemical looping (CL) can be an interesting and economical options for the use/reuse of carbon dioxide. This technology allows the splitting of exhaust gas components (i.e. CO_2 and H_2O) from fossil power plants, using renewable sources (i.e. solar energy, electrolysis hydrogen) for syngas production, which can be upgraded to chemicals or fuels. Therefore, this technology helps to create a renewable to fuel chain with a dual objective of recycling CO_2 emissions and as a renewable energy storage mechanism. With these few premises, it is easy to recognize how the demand for hydrocarbons, used as a primary source, will still grow in the future. This will eventually lead to a further increase in carbon dioxide emissions, unless measures are taken for a faster transition to different primary sources [3]. In this sense, it is highlighted in a IEA report on the impacts of global warming [4] that these fast-transition interventions are already taken into account in several strategic plans that provide for rigorous efforts in changing energy policies. These policies include a special focus on carbon capture and storage (CCS) technologies, with a special focus on CCS adopted with a view to retrofitting from existing production facilities. However, it is pointed out that these retrofitting actions are not enough to solve the problem of the amount of CO_2 generated by the same plants that determine its production. In other words, it would not be possible to think of such large accumulations of CO_2 , for which the most popular technologies to date (such as accumulation in exhausted oil sites or geological formations), also have safety implications with regard to long-term accumulation [5]. Technological efforts to facilitate the sequestration of CO_2 , should go hand in hand with policies for the reuse of most of the CO_2 produced. In terms of reuse, we can think of the production of synthetic gas derived precisely from emissions into the atmosphere. This gas can be useful as raw material for different purposes [6]. At the moment, this synthetic gas is produced using biomass, natural gas and coal, also thanks to several technologies now known [7]. Other methods to produce synthetic fuels, including syngas and H_2 , can occur in combination with solar energy. In this case we can talk about "solar fuels" for which you can find different references in the literature [8, 9]. These technologies are finding more and more success due also to the constant search for improvement in terms of materials and application methods. Thus, as knowledge is developing, , the relative cost of these methods is decreasing. Indeed, it is coming to competition with steam

methane reforming (SMR) processes. The degree of SMR technology development does not allow to achieve greater efficiency. This will lead to a strong use of fossil fuels as raw materials [10]. In theory, the easiest way to obtain syngas from CO_2 and/or H_2O is direct thermal splitting. However, this process requires temperatures close to 2400 °C which are not achievable with current technologies. Moreover, there is still the majority problem of the separation of H_2 and O_2 to avoid explosive mixtures, which is still difficult to achieve in an economic way. To solve these problems, the alternative solution is to predict the thermochemical process divided into two steps: one reduction and one oxidation of a metal oxide. This allows you to drastically reduce the temperatures in play. The aim of this technology is to contribute to the mitigation of greenhouse gas emissions from the energy sector. This is done by promoting efficient redox-active oxygen carriers for the chemical loop (CL), possibly enhanced by hydrogen. The ultimate goal is to achieve an efficient conversion from renewable to fuel, under conditions relevant to industrial applications. Therefore, in redox cycles characterized by two steps, the solid reagent is typically a metal oxide. It performs the function of "oxygen carrier", hence it's also called with this nominative. This metal oxide changes its oxidation state by capturing and releasing oxygen, in such a way that it can repeat the operation cyclically. Among the most promising materials to carry out the task of oxygen transporter, we find ferrites, ceria-based materials and perovskites. A lot of work is being done on all these materials in order to increase their transport effects and thus their oxide-reducing properties, acting on the crystalline matrix and then doping the starting materials with elements that allow to achieve better performance [11]. To better describe the context in which chemical looping technologies are addressed, an overview of CO_2 uses and emissions is proposed below, analyzing historical data. Indeed, it is particularly important to understand what proportion of CO_2 emissions would be affected in its use by these technologies and from which sectors its origin derives. Currently, the percentage diffusion of technologies concerning CO_2 capture is distributed as shown in figure 1.1 elaborated from IEA in 2019 [12]. The sector in which these technologies have found easier application is the Gas Processing one, which represents two thirds of the total. Also the production of synfuel (10%) and power (8%) have interesting development prospects. Instead, all the other sectors are still affected by the backwardness in the studies of these

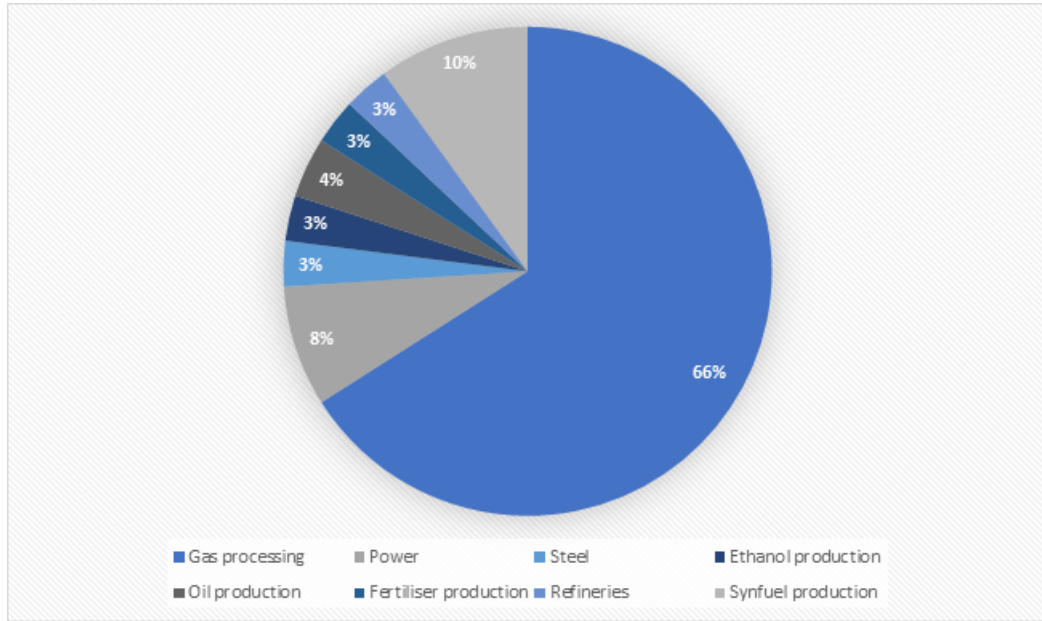


Figure 1.1: CO_2 capture capacity currently on market. Data elaborated from [12].

technologies and the technical and economic difficulties in facing them. If we want to identify parameters influencing emissions, we can use the Kaya Identity, whose purpose is to calculate the country's carbon dioxide emissions through economic and social indicators. It represents a concrete method to calculate the human impact on emissions. The factors considered are the energy used, GDP (Gross Domestic Product) and the population [13]. This expression is a simple identity (simplifying the terms we would get in fact $CO_2 = CO_2$ equality), however it is useful to have an effective overview of the factors that have influenced the trend of Italian emissions. The graph was created using indices, in which the value 100 is attributed to each factor in the year chosen as a reference (1990). The increase or decrease of this index, in the other years, therefore indicates the increase or decrease in the incidence of the specific factor on the total value. From the graph it can be inferred that until 2005, a large weight on the increase in emissions is dictated by the increase in GDP per capita. Even though, there was a slight decline in correspondence with the 2008 crisis, it got back up in recent times. The population growth is rather limited and has an almost negligible impact on the total. As for energy intensity, the decline from Seventies to date is remarkable and

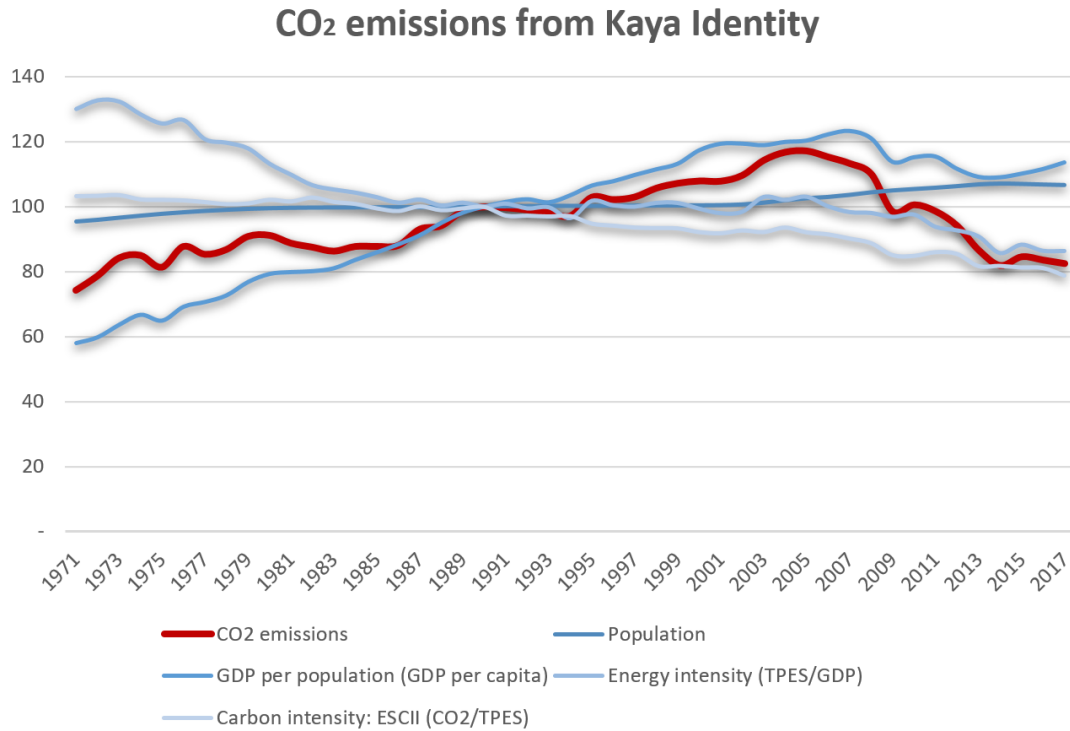


Figure 1.2: Representation of the kaya index together with its indicators.

substantially constant, thanks to an ever-greater energy efficiency and a conscious use of energy. Lastly, the intensity of CO_2 has also a decreasing trend, but in a less marked way, compared to energy intensity. The combination of these four factors allows to obtain the curve representing the CO_2 emissions in figure 1.2. More in detail, figure 1.3 allows to have a precise idea of the emission impact of the various economic sectors over time. The largest decrease is recorded in electricity generation, despite a slight increase starting from 2014. As regards the industrial sector, it was the largest emitter until 1982 (in 1974, the peak year, it exceeded 125 Mt), but has achieved a constant decrease over time, up to much lower values: in 2014 emissions were just over 46 Mt. In the transport sector, after a growth exponential until 2005, there is a significant reduction. However, in the last year reported in the graph, a slight rise also in this sector can be noticed. Finally, the curve that represents the buildings presents a substantially constant trend. According to the IEA [15], in 2060 these technologies could contribute 24% to

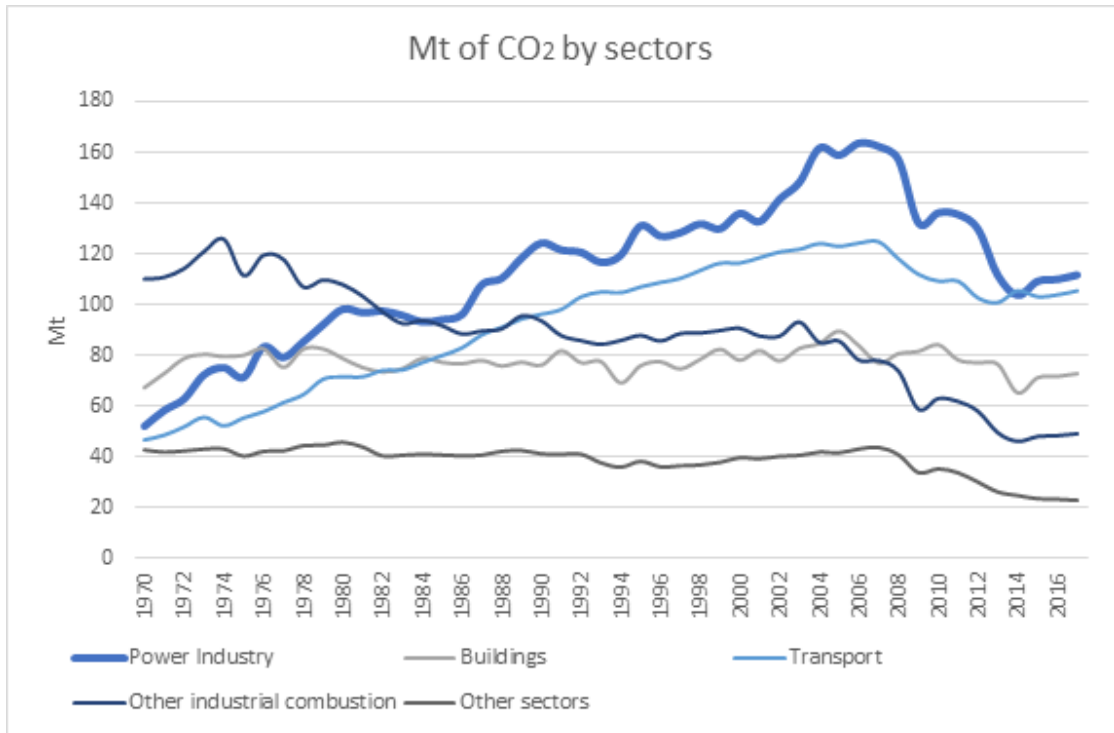


Figure 1.3: Carbon dioxide emission in Italy differentiated by sectors. Data elaborated from [14].

the reduction of emissions. Therefore, they represent a fundamental ally for the achievement of environmental objectives. However, it must be considered that even less restrictive scenarios than that dictated by the CTS, cannot in any case ignore these emission limitation techniques. The steel, cement and chemical subsectors are responsible for 70% of total emissions. Therefore, it is good to focus attention on these subsectors. In these areas, considering the Clean Technology Scenario (figure 1.4a), through the CCUS supply chain, the overall emissions are almost 1.3 Gt. It is estimated that around 0.4 Gt could be removed for both the cement and the steel industry, while for the chemical industry this value would almost reach 0.5 Gt. However, even in the RTS scenario (1.4b), CCUS techniques cannot be ignored, but their development would be much more limited (just over 0.6 Gt).

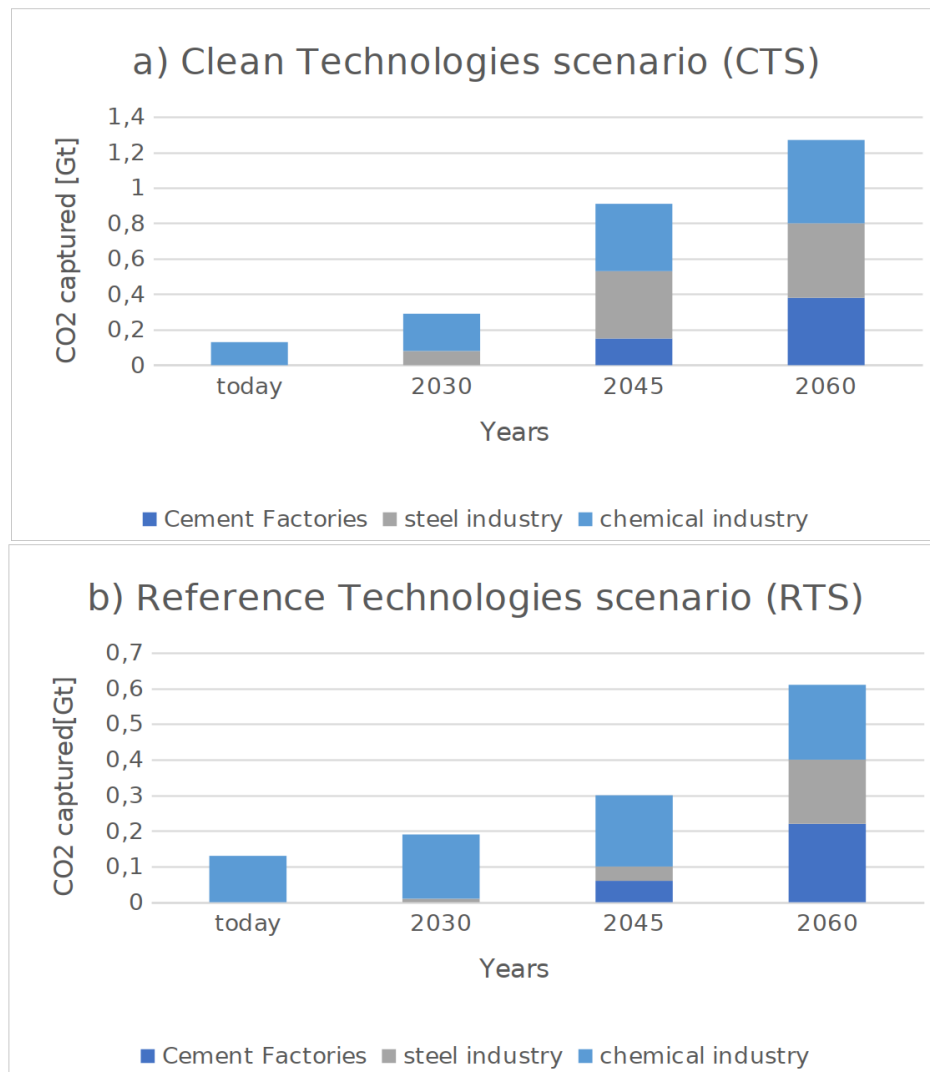


Figure 1.4: Forecasts of the development of carbon capture and storage technologies in the future according to two different scenarios. Case a) development of the clean technology scenario; case b) development of the reference technology scenario. Data elaborated from

1.2 Material for Chemical Looping CO_2 reuse

It is clear from the conclusion of this first section that CO_2 capture is a key issue for future technology developments. One of the most impactful problems for the advancement of capture technologies lies in finding suitable materials to perform

this task. Recently, several materials have been tested to check their performance against oxygen exchange. The firsts to be considered were metal oxides characterized by volatilization during reduction, with negligible difficulties encountered during the hardening and sublimation process. For this reason, research has been focused towards non-volatile metal oxides [16]. Many ferrite-based materials were tested [17]. Then the research focused on non-stoichiometric vectors such as, doped ceria or ceria, in parallel with perovskites with a high degree of oxygen storage [18]. Indeed, according to this review, perovskite studies of the type Lanthanum–Strontium–Manganates (LSM) confirm the higher yield of O_2 compared to the ceria and lower temperatures necessary for the reaction. Even though, they present an incomplete re-oxidation in the presence of CO_2 . Other studies reported in this review are instead focused on the differences received in the use of media such as ZrO_2 , Al_2O_3 or SiO_2 . As already mentioned in the initial summary, for this work the reduction in the presence of hydrogen has been explored to facilitate timing and temperatures, as well as giving greater weight to oxidative behavior in the presence of CO_2 . However, in the literature, information can also be found regarding purely thermal reduction methods also adopted with perovskites such as Albrecht et al. [19] who have carried out studies on thermochemical storage systems (TCES) using thermally reduced perovskites with temperatures between 700 and 1100 °C and with low partial pressures of O_2 , combined in the thermochemical cycle with re-oxidation in the air. Once the starting material has been chosen, there is a further branch in the study of materials that consists in selecting the right doping mixes to allow the improvement of performance. Furthermore, it also allows to avoid some side effects that may result from oxidation and / or reductions with gases of different nature. The research is also extended to the characterization of the mechanical mix of two different oxygen carriers. In particular Zhao et al. [20] studied the performance and synthesis of a metal oxide composed of Cerium and Zirconium in equal measure that has both ion conductivity characteristics of O_2 and electronics. It decompose into an atmosphere of N_2 at a temperature of 800 °C, but manages to remain stable in air up to 900 °C. More recent studies [21], are always based on the initial structure of Cerium oxide, doped with elements mainly belonging to the rare earth group and that of transition metals. From the studies already mentioned, it is recognized as necessary to investigate the temperature ranges with which redox

cycles can occur to achieve appreciable levels of non-stoichiometry. It is clear from these reported studies that it is undoubtedly interesting for research to reduce the heat of these materials. However, it remains a fact that reducing the material by using a fuel in a redox cycle, brings more benefits. Furthermore it makes possible a research area intended for the recycling/conversion of CO_2 , even in contexts that provide large plants both for energy production and in the power to liquid sector. Therefore, this introduction has been designed with the aim of describing the greatest challenges that still have to be overcome. It highlights some of the most common limitations of these systems and evaluates some aspects of feasibility with regard to the use of CO_2 . This gas has the potential to be transformed from waste to new raw material with undeniable benefits on the environment.

Chapter 2

Literature review

2.1 Carbon capture, storage and sequestration

CO_2 capture technology has made an appearance in the 1970s, after the first energy crisis, establishing itself as a new method of tackling climate change. The 2020 report of the Global CCS Institute [22] shows that to date existing plants can manage 40 Mt of CO_2 every year. There are also 34 experimental plants in operation or in the process of being completed and 8 centers for the experimentation of new CCS technologies. Depending on the type of capture, CO_2 can be separated from other compounds at different stages of combustion. In particular, there are three main categories of CO_2 separation processes from other gases: they are differentiated into pre-combustion, post-combustion and oxi-fuel plants. In the type of post-combustion carbon capture, CO_2 is separated downstream of exhaust gases after burning fossil fuels [23]. One of the main advantages of this technology is that it can be adopted to modernize existing fossil fuel plants such as coal or natural gas plants. Since the partial pressure of CO_2 present in the exhaust gases remains low, its removal process results in a penalty in terms of plant efficiency. The most common CO_2 separation processes are chemical and physical absorption in which CO_2 is removed via a liquid solvent. In physical absorption, CO_2 is physically captured on the surface of the solvent with a high absorption capacity at high pressures; in the chemical process instead, there is separation with alkaline solvents such as monoethanolamine (MEA), then there is a process of

regeneration of the CO_2 -rich solvent by heating [24, 25]. An oxyfuel-based CCS process consists of burning the fuel in an atmosphere of pure oxygen in such a way that the combustible gas is not diluted with Nitrogen, but instead is composed of CO_2 and water which can therefore be easily separable in a capacitor. Thus, oxyfuel combustion allows to reach up to 99.9% CO_2 captured by fumes. Besides, since N_2 is present in very low concentrations, the production of nitrogen oxides (NOx) also remains limited. In the literature, we find evidence of the use of this technology also combined with new plants, but it still lends itself very well to the improvement of existing power plants with the device of some modifications [26]. The main disadvantage of oxyfuel plants is in oxygen supply; there are two methodologies best known to date for using oxy-combustion technologies: the first consists of an air separation unit (ASU) from which the oxygen then used for combustion processes downstream of this unit is extrapolated. The second method is the use of ion transport membranes (ITMs), which separate oxygen from the containing flow (again typically air). These processes are quite energy-intensive and therefore result in a reduction in overall plant performance that cannot be overlooked. It is estimated for ASU a consumption between 0.16 and 0.25 kWh for each kg of O_2 produced at 95% purity [27]. This could be one of the reasons why there are currently no large-scale oxyfuel combustion plants, only pilot or demonstration plants derived from coal combustion technologies [28]. This aspect is well described in figure 2.1 where the oxyfuel plants with CCS technology are displayed by year of first operation. All the plants with CCS included are represented the red square in the figure mentioned. They are just demonstrative and not yet supposed to be on industrial scale. There are also a bunch of plants that are not yet proceeded into the demonstrative section. This to notice how this implementation of the capture it is behind the normal oxy-fuel plants without capture which were already present on an industrial scale before the 2000s. Even less are the plants always based on oxyfuel combustion that use natural gas as their main fuel. In fact, they are an even lower state of development than plants based on coal combustion. The last route for CO_2 capture is in pre-combustion processes where carbon dioxide is captured during fuel pre-treatment, which can again be coal or natural gas. After the seizure, the CO_2 is dehydrated, conditioned, and pressurized up to 110 bar and then sent to the storage site via pipeline, railways, or roads. It can be pointed out

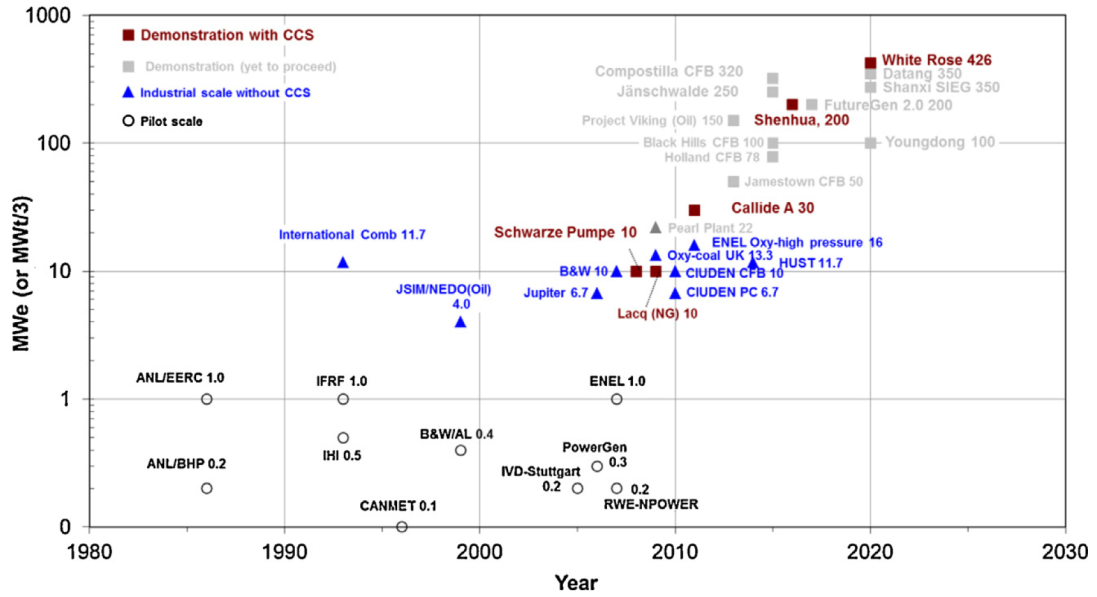


Figure 2.1: Representation by power and year through historical progression of oxyfuel combustion plants from small scale pilot up to large scale [28]. The plants with the presence of capture systems are highlighted in red, while the blue ones are exclusive to carbon capture systems.

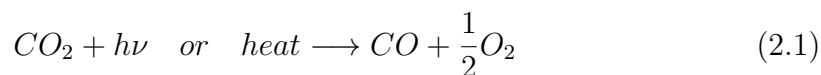
that at the moment the most promising method of transport, especially for larger production plants, is through ducts. This can also come from the fact that it has been the technology used for decades, especially in the USA, for the recovery of oil (EOR) from production plants almost at the end of the reservoir. In addition to oil recovery, there are also other options for storing CO_2 [29], at the moment the most corroborated include storage in geological sites and unmined coal beds. The loss of plant efficiency is a consequence that cannot yet be overcome, and is estimated at between 7 and 15% depending also on the type of storage that is considered [23]. It's not just what worries about CO_2 storage; potential loss, earthquakes global storage capacity, engineering feasibility and economic expenses are all factors that limit and put a strong brake on the CCS chain [30]. So CO_2 could have a more promising future as a carbon raw material than being considered a waste gas to be stored. Being considered a primary source of carbon thus makes it suitable for the use of new chemical compounds and fuels. Yuan et al. [31] reported a large number of technologies of CO_2 capture from stationary and air sources based on solid and

liquid solvents and membranes. Highlighting the advantages and disadvantages of different technologies. Given the low efficiencies and productivity of these technologies nowadays, the conversion of CO_2 through single-step electrochemical or photochemical processes is unfortunately still in development for the near and medium future. When compared to photochemical/electrochemical/biochemical processes, catalytic and thermochemical processes for CO_2 conversion promise more promising prospects shortly, especially concerning larger-scale applications. However, it remains an important fact that the alternative to CO_2 storage has received great attention from the scientific and industrial fields in recent years. As already mentioned, this type of process is referred to as carbon capture and utilization (CCU). This concept not only allows for new ways of exploring cleaner combustible gases but also allows a more sustainable energy economy [32]. The process of recycling carbon dioxide, therefore, takes place through its direct use or converting it into something new. Some uses of this gas by companies in different sectors can be mentioned. Taking the food and beverage industry as an example, it uses CO_2 as a gaseous agent. In other sectors such as pharmaceuticals, on the other hand, it is an intermediate useful for the synthesis of drugs. Taking into account all sectors that use carbon dioxide, no reuse levels are achieved that can guarantee a reduction in emissions, conversely, the conversion of this greenhouse gas into fuels and other chemicals allows to reduce a greater portion of catch costs by also encouraging a closed carbon cycle as also described by Huang et al. [33] in a review work on CO_2 uses. Concerning the use of CO_2 to convert it into chemical fuels or compounds, there was in the past greater skepticism for more than one reason: carbon dioxide incorporated in fuel does not have particularly long storage times (as the fuel is created specifically for later use), so that then CO_2 is re-released from the burned fuel again as an exhaust gas ending up in the atmosphere and not being caught repeatedly. There are also reasons for the conditions of dissociation that are not very convenient to be achieved by contributing to the reasons that have delayed the evolution of these recycling procedures. Only more recently have scientific studies been able to remedy this by retrofitting carbon dioxide from existing production facilities, thus mitigating emissions to produce appreciable results. In a study published in 2010, it was estimated that CO_2 recycling can account for 7% of the reduction of global emissions [34]. CO_2 is very stable thermodynamically,

which is why its conversion requires large amounts of energy, catalyst materials, and optimal reaction conditions. That is why more and more solutions are being sought to enable us to draw on these great demands for energy from renewable sources. On this subject, Mr. Von der Assen et al. [35] propose a systematic framework for Life-Cycle Assessment (LCA) study that can place environmental assessments on the concept of CO_2 use. Despite the conversion difficulties, it remains a fundamental co-reagent in some standard conversion processes in organic chemistry such as carboxylation of precursor compounds of other chemical agents or drugs. Then there is the alternative, which sees part of its application involved in this study, consisting of the reduction of CO_2 , breaking one or both C=O bonds giving the possibility of synthesis of new species such as syngas. The reduction of CO_2 in the specific case of this work appears to be the desired driving effect, as the exit from the reactor is found the presence of carbon monoxide, a molecule present in large percentages in syngas derived from fossil fuels. The roads for the reuse of this CO are also different, just think of a possible replenishment of fuel in the same plant, allowing recovery of efficiency as a result of the necessary reduction due to the capture of CO_2 . Knowing that syngas, as a mixture of H_2 and CO , is to date one of the most valuable resources that the industry possesses being so versatile and has a wide choice of uses, this can only encourage the study towards solutions that include this product and that value, even more, it is potential. Among the many processes used for the dissociation of CO_2 , what is part of the focus of this work is chemical looping, a process that has gained great attention in research especially for its large-scale application potential. Bayam et al. [36] provide an overview of different types of processes involving chemical looping, specifying potential configurations for application to power plants and chemical products in general. It follows a description regarding the known knowledge about the possible applications of chemical looping processes, with a particular emphasis on the materials tested, including a more detailed description of perovskites: from the main characteristics that distinguish them to details on the uses so far tested in the field of scientific research.

2.2 The use of carbon dioxide in chemical looping

Direct dissociation is one of the two main methods for thermochemical conversion of CO_2 . This predicts very high temperatures up to reach 2400 °C. Traynor and Reed [37] investigated a plant composed of solar focal mirrors combined with a secondary concentrator to provide great solar intensity around a ceramic tube. Heating a CO_2 flow to such an extent that it can be dissociated into CO and O_2 . In this study, they were able to achieve maximum conversion of 6% from CO_2 to CO and a solar-to-chemical energy-conversion of 5%. In short, this technology has been designed to intercept a flow from coal-fired plants or cement production centers, thus converting exhaust gases into new useful fuel. This type of conversion is also called direct photolysis, which is represented by the following equation:



This solar absorption by CO_2 is made possible thanks to a strong preheating that allows the CO_2 absorption spectrum to expand, even going so far as to involve wavelengths of waves of the visible spectrum and not only of the ultraviolet part. For these reasons, temperatures of 1900°C were reached in the initial heating process even before the CO_2 flow reached the core of the solar reactor. The apparatus as a whole has been created in three main sections: a circular solar concentrator, a converter that can be considered as the core of the system where the conversion reaction from reagents to products takes place, all crowned by adequate instrumentation to manage flows, solar pursuit and not of minor importance the post-conversion quench phase to avoid the recombination of products and not obtain the desired CO at the exit of the gas line. In the figure 2.2 is shown schematically the setup of the system used by the researchers where the CO_2 passages are highlighted, the conversion point where the ceramic tube is located, and strong post-conversion cooling that brings the temperature downstream of the concentrator between 500 and 600 °C where the connections to the analyzer for data collection are located. From this brief description, it can be understood how the need for very high temperatures is one of the main limiting factors for the

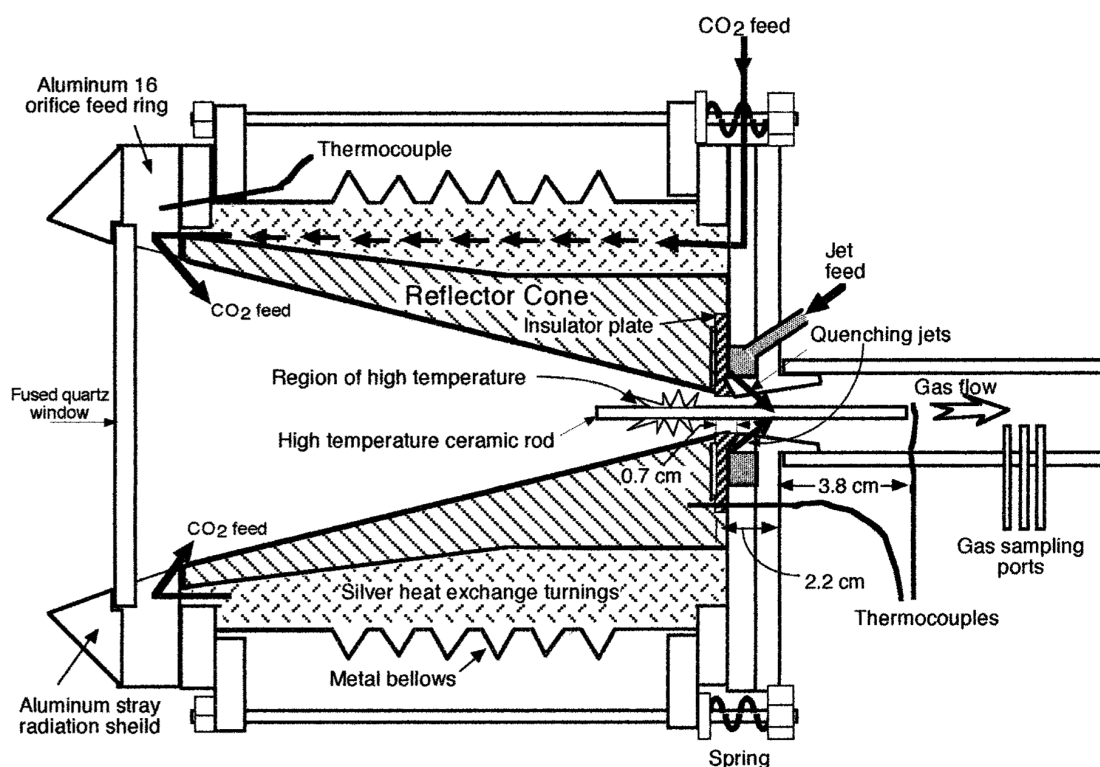


Figure 2.2: Converter unit for direct solar reduction of CO_2 [36]. The gas path is indicated by the arrow as well as the jet feed injection is shown.

application of these systems without counting the energy efforts necessary to carry out a strong quench that makes this type of application inconvenient. Otherwise, chemical looping processes are based on the use of a set of chemical reactions that can be repeated, ideally, in a perpetual way by re-circularizing one of the reagents and alternating it in different oxidative states. In this way, a closed cycle is formed in which the reagent in circulation (metal oxide generally) is never lost and consequently no waste is generated in large quantities. Figure 2.3 shows a generic diagram of a chemical looping process based on the recirculation of the oxygen carrier using three reactors. In the Reactor 1 the metal oxide/oxygen carrier is reduced generating the useful stream at the output, then partially oxidized in reactor number 2 and then carrying out a complete reoxidation only in reactor 3. Considering the whole system, it is also indicated in the figure an incoming flow of make-up of the reagent that oxidizes and reduces alternately: there are always

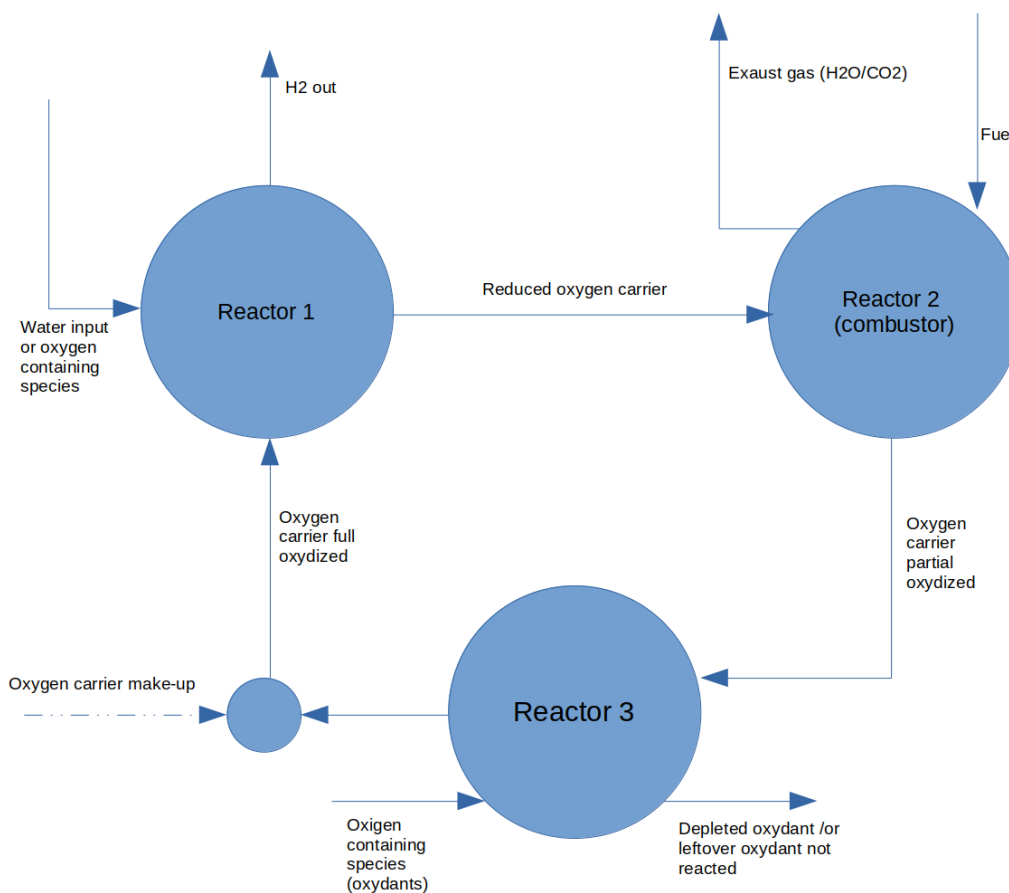


Figure 2.3: Example of chemical looping made by three reactors with recirculation of the oxygen carrier.

leaks and it must be considered the fact that all materials have a limited life for which they can efficiently perform the function of oxygen carriers. A reduction of the performances is always present after some cycles even for the most performing and promising materials. In not all cases, however, it is necessary to separate the reoxidation into more than one reactor and is therefore faced with systems with two stages only. In the case of research studies, then, as carried out for this study, the conditions present in the two reactors for the reduction and oxidation of the reagent material can be simulated in the same environment. Thus keeping the material fixed in a packed-bed type reactor, it is possible to simplify the setup, reduce costs, still managing to obtain valid data for a post-process study. At the same time,

however, simplifying the system results in new problems as example, certainly the lengthening of reaction times between a reduction and oxidation that will require waiting to reach the two setpoint temperatures decided with adequate growth ramps for both materials and tools. This is because in many cases individual reactions can be both endothermic and exothermic, thus requiring different temperature conditions in one case than the other. Normally the reduction of metal oxide requires higher temperatures to provide acceptable results, while oxidation requires lower temperatures in relation also to the oxidant that is sent into the flow. For this reason, given large-scale operation, integrations are necessary to the system that provide regenerative heat exchangers with possibly pinch-analysis studies to improve the exchange performance between hot and cold fluids. There are also cases in which it is possible to maintain isothermicity throughout the process that can be more convenient from the plant point of view, taking into account the consequent losses of efficiency of the entire process due to the maintenance of a temperature higher than that necessary to carry out the desired reactions in some sectors of the setup. Among the most developed processes of chemical looping can be related to the type of cracking processes by catalytic fluid (FCC), in which hydrocarbon chains are broken. The catalyst during the process is consumed and therefore needs a regeneration system to be reused cyclically. Figure 2.4 shows schematically and in a simplified way a possible cycle for the regeneration of the catalyst used in the reactor in the figure on the left side. Leaving the consumed reactor, it is directed to a regenerating system where a fluid, passing through the catalyst, allows it to be reactivated. To improve the reactivation state, a re-circulation of the catalyst is also provided for within the regenerator. Once regenerated, the catalyst capable of reactivating is re-fluxed into the reactor to separate the hydrocarbon chains. Among the best known CCS processes, monoethanolamines (MEAs) also involve a chemical looping system, where spent gas is treated with MEA in a reactor. In this reactor, MEAs capture CO_2 present in the exhausted gas, along with other oxides present as SO_2 . The cold mixture is then heated by releasing the absorbed molecules in the previous step. The amines are then returned to a lower temperature and then reused again. This method is used as a post-combustion method for CO_2 separation, and can therefore be applied in retrofitting existing plants. The most recent approaches to the use of chemical looping that always

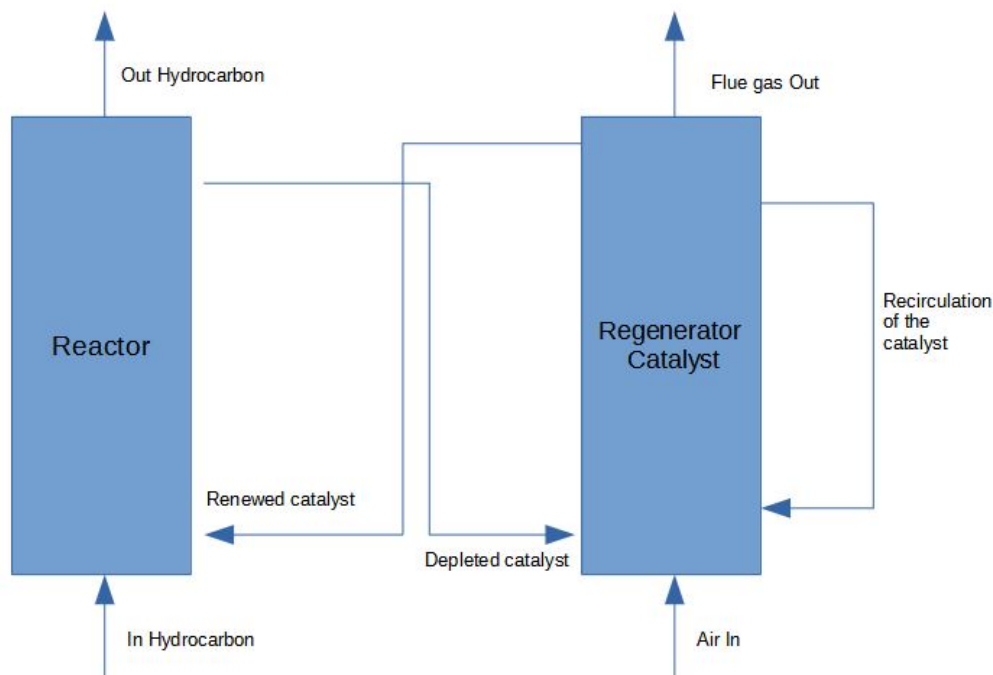


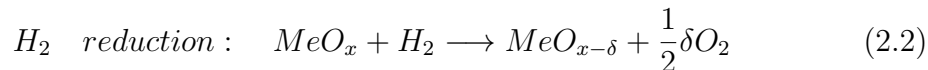
Figure 2.4: Example diagram of the possible catalyst regeneration procedure in an FCC process

refer to carbon capture are chemical looping combustion (CLC) processes. These processes come much closer as a concept to the approach used in the study of this thesis, however, I differ for some fundamental precautions. Metal oxides are indeed used for the transport of oxygen, but the primary objective of these systems is mainly in the form of the need to decarbonize a fuel or to produce hydrogen for other uses. The figure 2.3 can be representative of a three-stage CLC system, where, unlike the purpose of the setup of this thesis, which as mentioned in the first section attempts new ways to remove CO_2 from the atmosphere, in this case, it is instead the system that emits CO_2 by combustion with a carbonaceous fuel that after different stages of the process arrive at the final product in the form of chemical energy of the hydrogen produced. The entire process, being exothermic, also allows the production of high-temperature steam. Thus, in CLC there are similarities with this work, but other methods of splitting CO_2 and H_2O are based on the absorption of solar radiation or reduction with methane or hydrogen as in the experiment done in this work which use H_2 for the reduction of SFNM

perovskites.

2.3 Chemical looping processes for the dissociation of CO_2 and H_2O or carbonaceous fuels

Chemical looping processes are used for syngas production and may include CO_2 or H_2O dissociation phenomena to have a CO and H_2 -based product. The best-known setup for this type of chemical looping consists of two interconnected reactors, in a reactor, the reduction reaction of the material present leads to the creation of new oxygen vacancies in the matrix, in the second reactor then this same material is oxidized through CO_2 and/or H_2O with the consequent release of CO and H_2 at the exit. These two reduction and oxidation phenomena are repeated cyclically in a loop in which the material is reused from time to time. The material can be reduced by the thermal process (with temperatures above 1300°C), or by using a reducing agent (e.g. H_2). The fundamental phenomenon that governs the feasibility of these processes and consequently their convenience or not, is precisely this creation of vacancies within the material matrix. Subsequent re-oxidation usually takes place at lower temperatures (below 1000°C). To make a thermal reduction the partial pressure of oxygen in the mixture must be very low, that is, the process is favored in vacuum conditions. Presenting the opposite case for oxidation, this leads to swings of temperatures and pressures between the two steps. A reduction in a reducing environment, on the other hand, allows to lower the reduction temperature, even arriving at conditions for which the temperatures of the two steps can coincide. Considering that with a reducing fuel the pressures can remain even almost environment, this leads to a considerable simplification of the conditions necessary for the operation of the setup. Although the thermal reduction is one of the most studied processes with high prospects of innovation, the reduction with fuel presenting currently those characteristics of greater simplicity exposed above has been chosen as a solution to be implemented to verify the material studied in this work. The equations 2.2 and 2.3 show the macroscopic reaction chain that occurs for the reduction and subsequent oxidation of the oxygen carrier.



Another method of lowering temperatures and consequently having a minimum temperature swing between reduction and oxidation is methane reforming processes. Krencke et al. [38] have studied a system that would bring the benefits of partial methane oxidation with a thermal reduction on cerium oxides. Maintaining an isothermic system they were able to lower the operating temperature to 950 °C. In addition to these advantages of a kinetic and thermodynamic nature, there are also economic aspects: in fact, methane can be obtained from different resources, starting from the most commonly natural gas. Other sources of methane are found through the power to gas (P2G) technologies that are facilitated to progress thanks to a mature natural gas distribution network. In addition to the temperature reduction, these methods allow, thanks to the use of a non-oscillating source in availability as renewables can be, to operate continuously without unproductive intervals. The reaction, in this case, translates into 2.4, where already in the reduction there is the production of syngas as well as in oxidation that if performed with CO_2 you return to the equation 2.3.



Ebrahimi et al. [39] has tested the performance of an oxygen carrier composed of $La_{0,7}Sr_{0,3}FeO_3$ perovskite (LSF731) testing various kinetic models evaluating both the gas-solid transition part and the catalytic activation part. In this work, a chemical looping reforming (CLR) setup natural gas (methane) promotes the production mainly of hydrogen, carbon monoxide, carbon dioxide, and water through the use of metal oxide. From the literature among the best known oxygen carrier perovskites based on Ni, Cu, Fe are chosen for the versatility that characterizes these materials, moreover, the production of fuel is emphasized by the ability of the transition metals (such as Co, Cr, Fe, Mn) to replace some elements of the crystal lattice of perovskite. The work done by Ebrahimi et al. was then the

elaboration of a mathematical model to describe the production of syngas through a fixed bed microreactor. A furnace envisaged of maintaining approximately the constant temperature and thanks to the small size of the reactor it has been possible to achieve a good homogeneity of temperature. Argon has been used as a thinner and as a purge gas between the reduction and oxidation steps in the cycles. In this way, the kinetic parameters were obtained for a temperature of 850 °C kept constant. This study was considered important for this work even if it involved chemical looping of different types than that foreseen in the current investigation process, in fact, it was possible to obtain basic information regarding gas-solid kinetics. The figure 2.5 outlines the process of interaction between methane and

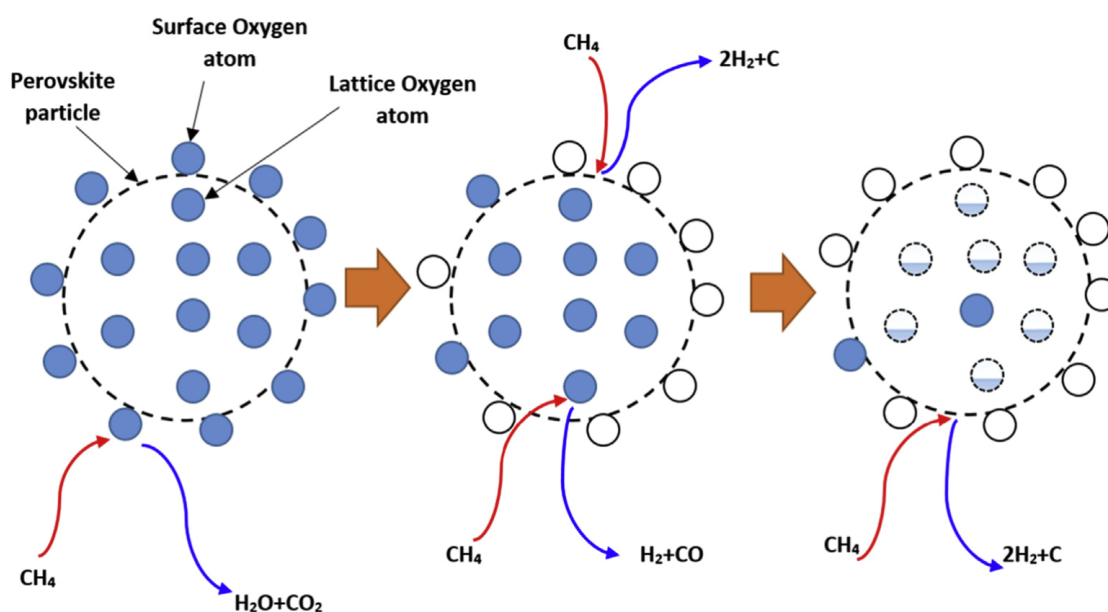
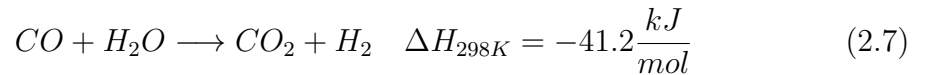
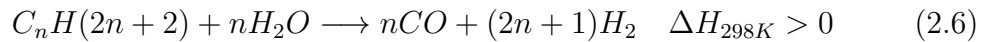


Figure 2.5: Schematic image representing the reduction mechanism of a perovskite with methane as reductant [39].

oxygen with the related products that arise as the oxygen vacancies generated progress. Initially, methane reacts with oxygen on the surface by classic combustion (left side of the figure 2.5), then thanks to the first vacancies created the reducing agent manages to spread inside the perovskite, reacting with the innermost oxygen and thus generating H₂ and CO having then exhausted the nearest holidays, the additional methane molecules interact with the surface of the material breaking and generating additional hydrogen and carbon at the same time. Under the

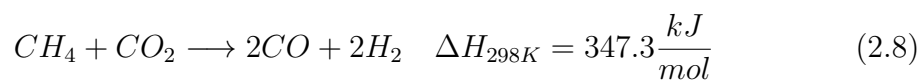
same conditions, Nickel oxides (NiO) were tested to check for differences between kinetics. The results show the complete reduction of LSF731 occurred after 2500 s while for Nickel 50 s was sufficient, and after 500 s carbon production begins not to become negligible. However, these results show that Nickel is an excellent catalyst when combined with carbon-containing molecules, which is why doping SFNM perovskites with Ni is interesting for CO_2 dissociation during material oxidation. Iliuta et al. [40] deepen carbon formation due to interaction with Nickel oxides, demonstrating that nickel is heavily dependent on oxygen availability. When there is a sufficient amount of oxygen in the metal oxide, the formation of carbon derived from methane is limited independently of the addition of steam if in the temperature range between 750 and 950 °C. On the other hand, if more than 80% of the oxygen available in the metal oxide has already been consumed, then the onset of surface carbon formation is denoted. Ultimately, therefore, it is the amount of oxygen added to nickel oxide that determines whether carbon formation can occur more or less quickly. This is if other parameters are consider as constant, such as temperatures and pressures.

Another alternative to CLR is steam methane reforming (SMR): this mature technology consists of reacting steam with the raw material in a set of reactions for the production mainly of hydrogen. The main reactions to this procedure are given below.



In particular, the equation 2.7 is intended to represent any hydrocarbon higher than methane contained in natural gas. Operating conditions are generally high temperatures (800-900 °C) and pressures between 15 and 30 bar, with steam-carbon S/C rate values between 2.5 and 3 [41]. The last proposed equation is commonly called water gas shift (WGS) reaction which can be applied in two distinct steps:

a high-temperature step in which the gas at 350°C with a high CO content is converted to H_2 with iron oxide catalysts. The reaction is exothermic, so the gas comes out at temperatures higher than the input (400-450 °C) and with an incomplete conversion. It is then cooled to about 220 °C for entry into a low-temperature step where the CO content present in the mixture is further reduced with a final conversion between 95 and 99%. These processes are very sensitive to sulfur poisoning, in fact, the concentration of H_2S must not exceed 0.5 ppm [41]. Another reaction that may intervene is represented by the equation 2.8 under the name of CO_2 reforming or dry reforming.

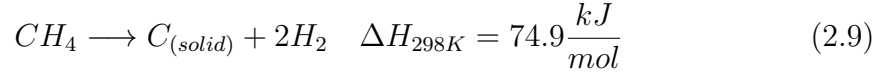


In dry reforming, CO_2 reacts with hydrocarbon resulting in a more endothermic reaction than SMR. However, it has captured a lot of attention for the possible application to remove CO_2 from the atmosphere. The nickel-based catalyst brings a second drawback in addition to endothermic, namely carbon deposition problems. This has not stopped the studies on the material because it is true that is more disadvantaged than elements such as Pt or other noble catalysts, but on other hand it has a much lower cost and therefore more possibilities to be applied in large-scale contexts. The variables that most influence the steam reforming process are temperature, pressure, and steam-carbon (S/C) molar rate. These variables must be chosen considering kinetics, the amount of gas used, process thermodynamics as well as economic factors. A catalyst is also essential for this reaction as overall the process is endothermic and therefore more favored at high temperatures. Nickel makes easier the reaction 2.5 and 2.6 thus decreasing the temperatures necessary for reform.

2.3.1 Carbon formation in chemical looping processes

The main conditions under which carbon formation can occur in a chemical looping can be divided into two distinct events: methane decomposition, described by equation 2.9 or at least a containing-carbon fuel, or by Boudouard equilibrium,

which consists of the expression 2.10.



The reaction affecting the specific field of application is also defined as reverse Boudouard reaction according to the formula 2.11:



This has greater implication in catalytic reaction cases, where it is important to

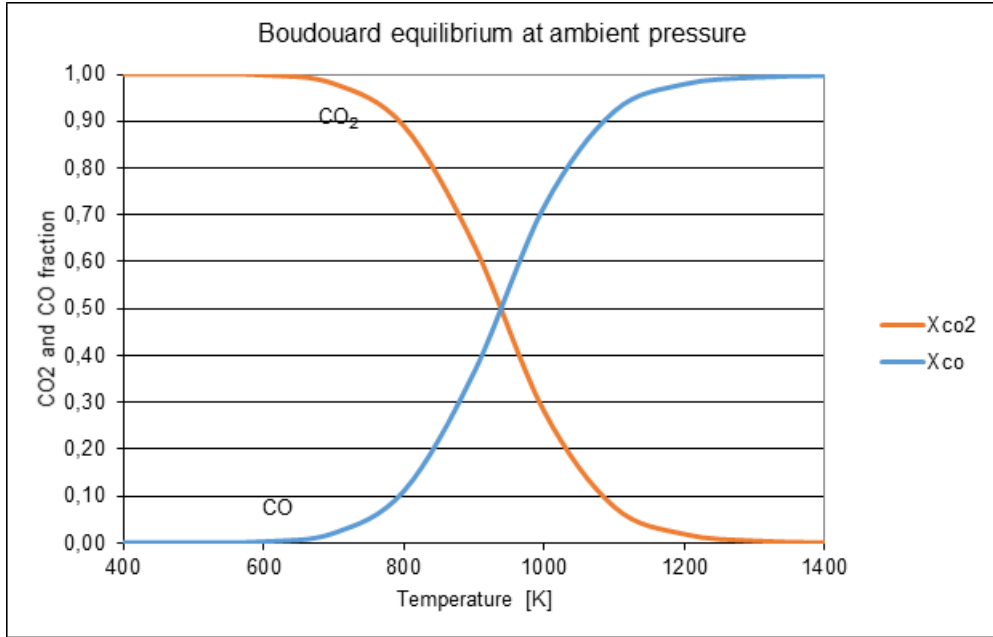


Figure 2.6: Representation of the mole fraction of CO_2 and CO in the Boudouard equilibrium as function of temperature.

define the carbon deposition on the outer surface of the material resulting in the deactivation of the catalyst [42]. With a ΔH negative the reaction is exothermic for the entire temperature range in which it can occur. In particular, it is inhibited at high temperatures while it is more favorable if in the presence of lower temperatures.

The figure 2.6 shows how the equilibrium present a reversal of the trend after 600 K where increasing the temperature also increase the fraction of CO. This trend goes up to saturation of the carbon monoxide and the almost disappearing of CO_2 after 1300 K. Kinetically both pyrolysis and Boudouard equilibrium are of limited importance if there is no catalyst, however, both of these reactions are catalyzed significantly by the presence of Nickel [40]. Boudouard's balance being as already anticipated always exothermic, therefore, more favored at low temperatures. In the same study, it is also mentioned that it has already been discovered in previous research that at high temperatures (600°C) the carbon obtained through the Boudouard reaction is less when compared to a methane decomposition. Finally, it can be defined that Nickel actively catalyzes the carbon deposition of the carrier in the reactor bed, imposing certain constraints on the type of oxygen carrier and the need to optimize the conditions of operation of the latter. The factor that unites both thermal reduction and fuel reduction is the non-stoichiometry of the oxygen carrier, which releases an amount of O_2 equal to 0.5δ moles, for which removal is necessary (by vacuum pump). Similar to the reduction during oxidation it will instead be some moles of O_2 that from the oxidizing agent (CO_2 or H_2O) will again switch to metallic oxide, producing CO if CO_2 and H_2 if H_2O is used. Mixed splitting systems of H_2O/CO_2 at the same time have also been studied [43] to obtain an additional generation of power from exhausted gases derived from the oxy-fired natural gas-fired power plant, with the possibility of externalizing the setup to other combustion technologies as well.

2.4 Different types of oxygen carriers

An oxygen carrier is essentially a metal oxide with at least two different oxidation states: a metal state and an oxidized state. An example is Fe_3O_4/FeO iron oxides that manage to release oxygen when subjected to high reduction temperatures [18]. In the literature, several studies researched the best materials to be used in chemical looping for splitting [18, 44, 45, 46]. This wide variety of materials for the transport of oxygen can be categorized according to different characteristics that distinguish them from each other, a possible way is to divide these materials according to their physical state that arises once reduced. This gives you volatile

oxygen carriers and non-volatile oxygen carriers.

2.4.1 Phase-changing metal oxide (volatile)

These materials exhibit a phase change when they move from oxidized to reduced state, especially at high temperatures in the presence of thermal reduction. The metal oxide thus reduced then passes from a solid-state to a state of steam in general, thanks to the lower boiling temperature of the metal compared to its oxide state. The processes that see the use of these particular materials consequently require a very strong quench that normally provides for a rapid lowering of the temperature, to prevent the newly released oxygen from returning to recombine with the metal allowing the reformation of the oxide [44]. The most common materials with volatile characteristics include Zinc oxides, germanium oxides, cadmium oxides, and tin oxides. The figure 2.7¹ shows a two-step chemical looping scheme of zinc oxides in which the temperature swing increases from 2000°C for reduction to 600°C for oxidation. The presence of refrigerant is essential to remove oxygen from zinc vapors to avoid recombination of the two. In these systems, however, some of the oxygen tends to recombine, thus reducing the total effect and efficiency of the cycle [18]. Vishnevetsky et al. [47] presented a work in which these materials were compared in a thermodynamic analysis conducted on two-stage thermochemical cycles. The results show that molar weight ratio – valence combined with $Me - O$ or stronger bonds requires more solar energy during the endothermic step, however, as a result of a higher exothermic stage with the release of greater amounts of heat suitable for self-healing. Conversely, oxides with higher molar weight ratio – valence and weaker $Me - O$ bond are more easily reduced with lower input solar energies. In general, however, for these metals there are strongly endothermic conditions in reduction with ΔG falling below zero only with temperatures above 1720 °C. Given the disadvantages described above, the study of these systems has recently been left out, giving more space to studies on materials that do not require strong post-reduction removal and that can also work at lower temperatures.

¹Image from Santarelli Massimo, Slide of the course of Polygeneration and advances energy systems - Fundamentals of hydrogen production from renewable energy sources, 2019, Politecnico di Torino

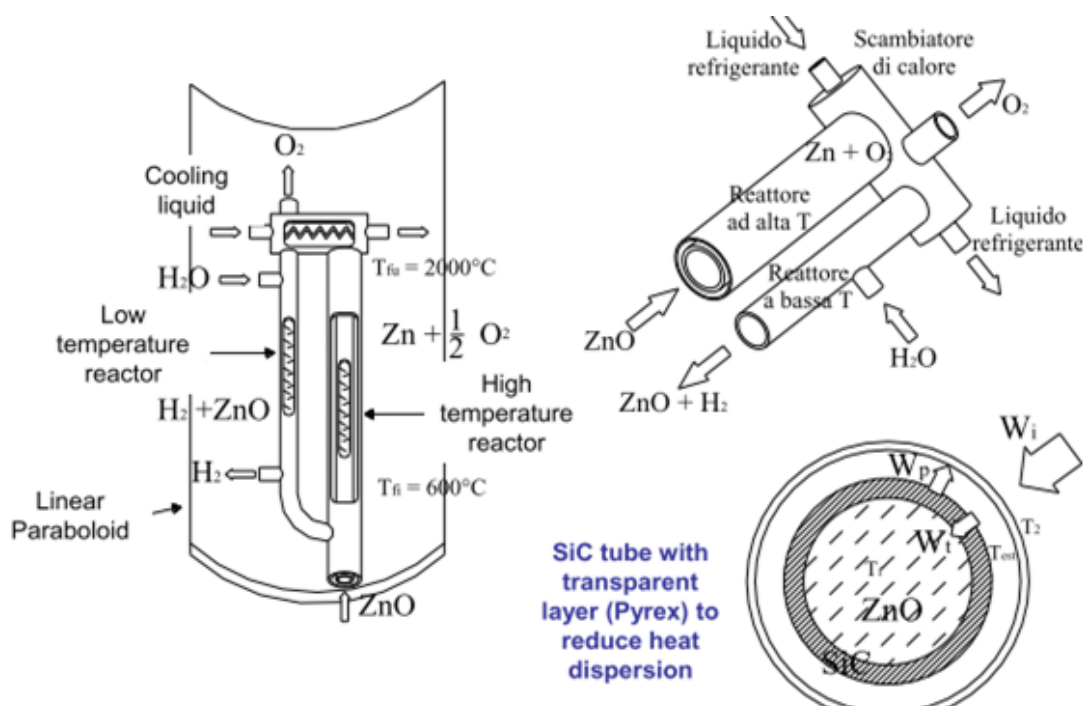


Figure 2.7: Zinc oxide reactor for water splitting and hydrogen production.

2.4.2 Non-volatile oxygen carrier

This particular type of oxygen conveyor does not develop any phase changes during the reduction transformation they remain solid throughout the entire cycle. Hence the first benefit, namely the need for a rapid quenching step, which is very energy-intensive and consequently lowers the overall performance of the process. However, this should be considered together with the fact that usually metal oxides that do not foresee a phase change, turn out to have a lower storage capacity than volatile oxygen conveyors [18]. Since the molecular weight of the oxygen exchanger is low, they consequently show a large sharing of oxygen atoms per unit of weight. So the storage capacity of non-volatile oxygen carriers is less than 2-5 times that of cerium oxides, for example. A particular category of non-volatile oxygen carriers is composed of materials that release oxygen in non-stoichiometric measurements. The most studied is certainly cerium oxide as it is structurally stable thanks to the optical and electrochemical properties and allows still competitive productivity of 8.5 – 11.8 ml of H_2 per gram of ceria and a fuel production rate of 4.6 – 6.2

ml of H_2 per minute per gram of ceria [48]. This material is characterized by increased efficiency, reduction extent, and methane conversion with the increase in temperature. And it results in a suppression of carbon formation with temperatures above 1300 °C [49]. However, there are many types of non-volatile metal oxides. Bush and Loutzenhiser [50] report on the use of iron oxides in thermochemical cycles with redox reactions combined with an electrical generation system. In the study, Fe_2O_3 is thermally reduced by operating at low partial pressures of O_2 to shift the balance to more favorable temperatures. The cycle is then based on two solid phases of iron oxide: Fe_2O_3 and Fe_3O_4 . To reduce hematite thermally, high temperatures resulting in a low overall cycle yield are also required here. The authors then specify how the oxidation process is not fully reflected by the proposed model, possibly due to rapid and complex reactions occurring during TGA tests at low time conversion regimes along with uncertainties due to the gas switch during testing. This has not made it possible to understand precisely which of the conversion steps is the decisive step for the global phenomenon. The oxidation process is however described in its main passages by the authors who also report a visual description shown in the figure 2.8. The process begins with

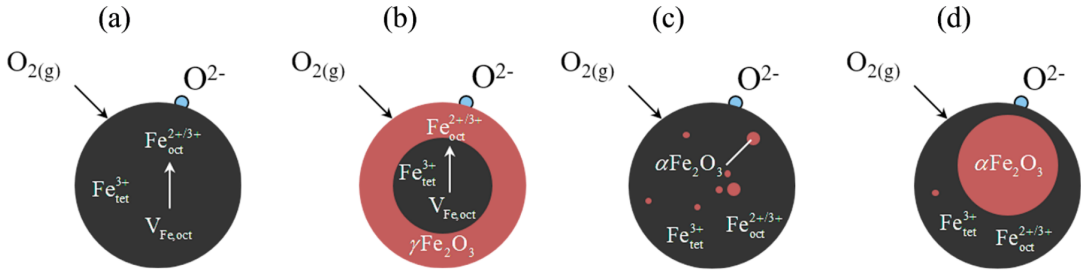


Figure 2.8: Fe_2O_3 oxidation pathways. Starting from the diffusion-limited regime (a), upon the magnetite start to segregate or $\gamma - Fe_2O_3$. Then in (c) is shown the transition to the nucleation-limited regime, ending with (d) where the oxidation result in hematite $\alpha - Fe_2O_3$ [50].

the diffusion of particles towards the contour to join O^{2-} , with the oxidation of cations from Fe^{2+} to Fe^{3+} and the consequent formation of vacancies. The reaction then proceeds under favorable thermodynamic conditions 2.8(b). This is followed by the nucleation of a new $\alpha - Fe$ phase induced by the temperatures and subsequent stresses on the oxide matrix (figure 2.8(c)). Subsequent oxidations of

the remaining Fe_3O_4 are shown in the figure 2.8(d) where the prevailing phase is already completely reduced.

Perovskites oxygen carrier

As mentioned earlier with some examples from the literature, perovskites are a good alternative to the most common oxygen transporters and have therefore captured great research interest. In particular, results are reported on the use of perovskites for CO_2 or H_2O splitting [51]. Most of the literature deals with improvements to materials according to two main approaches: optimizing composition or optimizing particle structure. For a possible future application of these technologies, materials must meet many requirements, including:

- Excellent oxygen exchange capacity;
- Thermodynamics favored depending on the selected fuel;
- Low risk of carbon formation;
- Structural established under cyclic conditions of reduction and oxidation;
- Reagent during the oxidation step;
- If it is intended to be used in fluid bed reactors, good material fluidization and friction resistance are important;
- The material must be possible to reproduce on a large scale and at competitive costs for the future;
- It must have environmentally favorable characteristics.

It is known that pressures and temperatures can induce phase transformations in oxides with structure ABO_3 (with A = transition metals or alkaline lands). The significance of material also derives from its structure and the properties that each different structure possesses. Perovskites have very different patterns of cations, holiday compensation and transitions caused by lattice distortions offer a wide range of materials. The fundamental question, therefore, remains what structure is formed under what conditions and how it behaves to the changes in pressures,

temperatures, and agents it encounters. How similar the cations of the ABO_3 structure are in size, the classical corundum structure takes shape. This basic structure involves layers of oxygen packaged in the hexagonal form with cations that define octagonal layers. Each layer is identical in the corundum structure. When different ions from the ABO_3 backbone, perovskite structures may form. In particular, this structure occurs when A-cations require longer bonds and greater coordination numbers than B cations. The ideal perovskite consists of a BO_6 framework in an octahedral form bound through every corner. In this regard, the

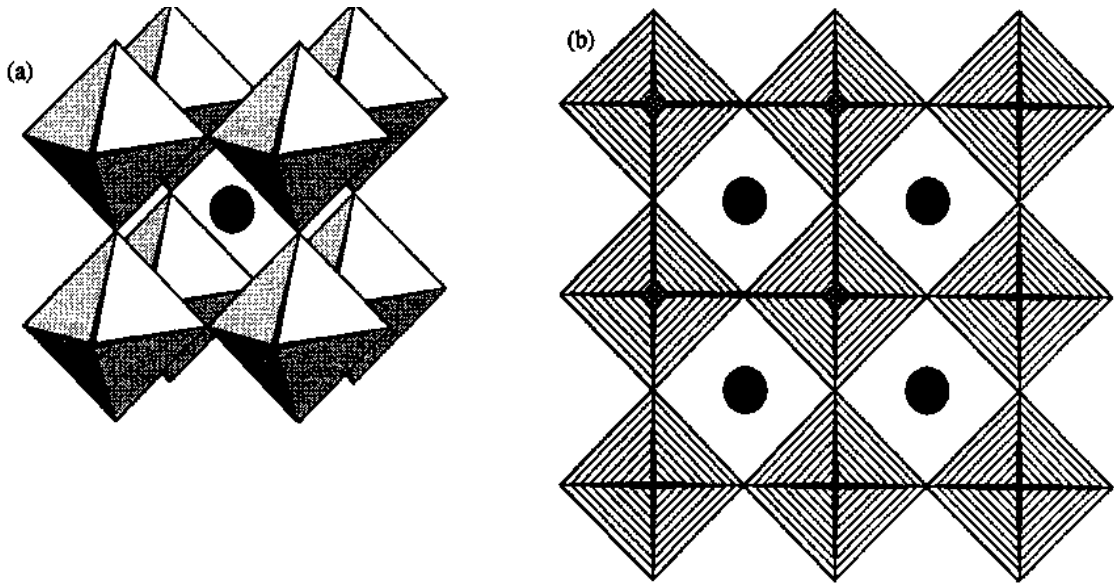


Figure 2.9: Representation of the ideal cubic perovskite structure. Left (a) shows a 3D representation; right (b) shows representation on a plane. Spheres represent A-site cations. B-site cations are placed inside the octahedral shapes [52].

figure 2.9 represents the structure described above. If the lattice forms an ideal cubic array, the interstitial zones define the sites. Because this interconnected network is created, a change in the length of a bond at a central site can disrupt the structure by changing inclination or creating lattice shrivels. These distortions allow different types of cations to sit on the sites of the structure. It is possible to define a tolerance factor for a classic ABO_3 perovskite such as:

$$t = \frac{r(AO)}{2^{0.5}r(BO)} = \frac{r(a) - r(O)}{2^{0.5}(r(B) + r(O))} \quad (2.12)$$

Where the terms r represent the bond lengths calculated as the sum of ion rays. If $t = 1$ then both cations have the same lengths and are distributed according to the ideal cubic form. If this number deviates (generally between 0.8 and 1.1) perovskite can still form with a certain degree of distortion concerning the cubic structure by modifying its thermodynamic and stability properties. The type and measurement of distortion depending on the pressure, temperature, and composition of the material. Navrotsky [52] has reported numerous transition phases for many systems including cations of different elements. In the study, it emerges that replacing tetrahedral Si and Gr with the octahedral counterparts lengthens and weakens the Si-O and Gr-O bond. Thus many other elements induce weakening in oxygen bonds allowing easier dissociation of ions and consequent creation of vacancies. The author also highlights the relationship between the size of A cations and energy costs for the formation of perovskite, as well as affirming a greater entropy of vibration even in the presence of a properly ordered matrix. This is related to the phenomenon of oxygen release as it is also a function of the reaction ΔG , i.e. the formation energy or free energy of Gibbs, expressed in a general way as:

$$\Delta G = \Delta H - T\Delta S \quad (2.13)$$

This determines the conditions necessary for the different evolution of the material depending on the external conditions and the composition that arises. It is generally accepted that perovskites are structures that remain more stable at high temperatures and pressures. The metals used as active components in perovskites are manifold: Fe, W, Sn, Ni, Cu, Mn, and Ce. At a time when metals alone do not complete the necessary requirements, there is the possibility to opt for supporting components such as ZrO_2 , TiO_2 , SiO_2 , Al_2O_3 to increase mechanical and chemical properties. These active components can be integrated into a unique structure together with metals, forming perovskites structures. Voitic et al. already mentioned earlier [51] reported *nano - LaFeO₃* perovskite oxides, which have a three-dimensional structure of the fresh sample and gradually collapses into repeated cycles caused by chemical and physical stress. The size of the grains and the crystallinity is therefore modified and in particular decreased, however, the porous structure with a small part of agglomeration is preserved and is stable during

the test cycles. The perovskite oxides of this family with cobalt doping are also to maintain the crystalline structure that characterizes them. The increase in Co then allows a higher concentration of oxygen vacancies resulting in stronger resistance to reduction. However, the composition is completely reducible. Experimental post-process analyses show degradation caused by sintering but are still compensated by the increase in oxygen vacancies. The addition of ceria shows that the volume of the pores and their diameter has been reduced by a small amount, partially filling the empty areas. In any case, better oxygen transport capabilities are seen at lower temperatures than classic metal oxides both pure and with the presence of specific doping. Perovskites presenting the generic formula $ABO_{3-\delta}$ promise a large non-stoichiometry especially if at high temperatures combined with excellent reversibility in oxidation, which is a key criterion for a material used in chemical looping for syngas production. To increase the performance of perovskites, solutions supported by metal oxides have been designed. The replacement of transition metals such as Cr, Co, Ni, Cu in $A_{1-x}Sr_xFeO_3$ has allowed an increase in performance. Jiang et al. [53] have tested several media on $LaFeO_3$ perovskite and several doping to replace atoms at A sites and in atoms at B sites. The replacement of these sites is made possible by the structural network that remains unchanged with a wide variety of elements, the stability of the perovskites is better than that of the corresponding metal oxides. In the work mentioned above in particular, a two-step chemical looping experimented with a fixed bed configuration. The reduction of perovskite came thermally to 1300°C in a high purity Argon environment, while for the re-oxidative part a CO_2 flow was expected at 1100°C. The choice of doping with Mn and Co as a substitute for iron lies in the easier reduction of the respective Mn and Co oxides compared to Fe_3O_4 oxide, the thermal reduction in this way is more favorable when compared to pure $LaFeO_3$. Cobalt particularly demonstrated higher oxygen productivity: $LaFe_{0.7}Co_{0.3}O_3$ generated 6.4 ml/g_{perovskite} of O_2 compared to 1.3 ml/g of $LaFeO_3$. On the other hand, different results were found for the oxidation process with the low CO generation, possibly due to the aggregation of particles after heat treatment, sintering of the material, therefore, avoided the reaction with CO_2 . The effects of perovskite support created to have 25% perovskite weight were then analyzed also combined with other doping, replacing in the A Sr^{2+} and Ce^{4+} sites that increased the reductive process but not the oxidative

process leaving always poor CO yields even worse than the non-doped perovskite supported by SiO_2 in the Form $LaFeO_3/SiO_2$. A decisive improvement was made possible by doping the material by replacing sites B with Co and Mn by analyzing different concentrations of doping. In this case, the maximum CO generation was achieved for $LaFe_xCo_{1-x}O_3$ with $x=0.7$ to 25% by weight on SiO_2 support. The generation was 4 times faster than $LaFeO_3$ and production in 20 minutes of oxidation reached $4.3\text{ ml}/g_{material}$ for $LaFe_{0.7}Co_{0.3}O_3$ compared to $1.2\text{ ml}/g_{material}$ of $LaFeO_3$. Picture 2.10 represents the oxidation curves with the CO production of

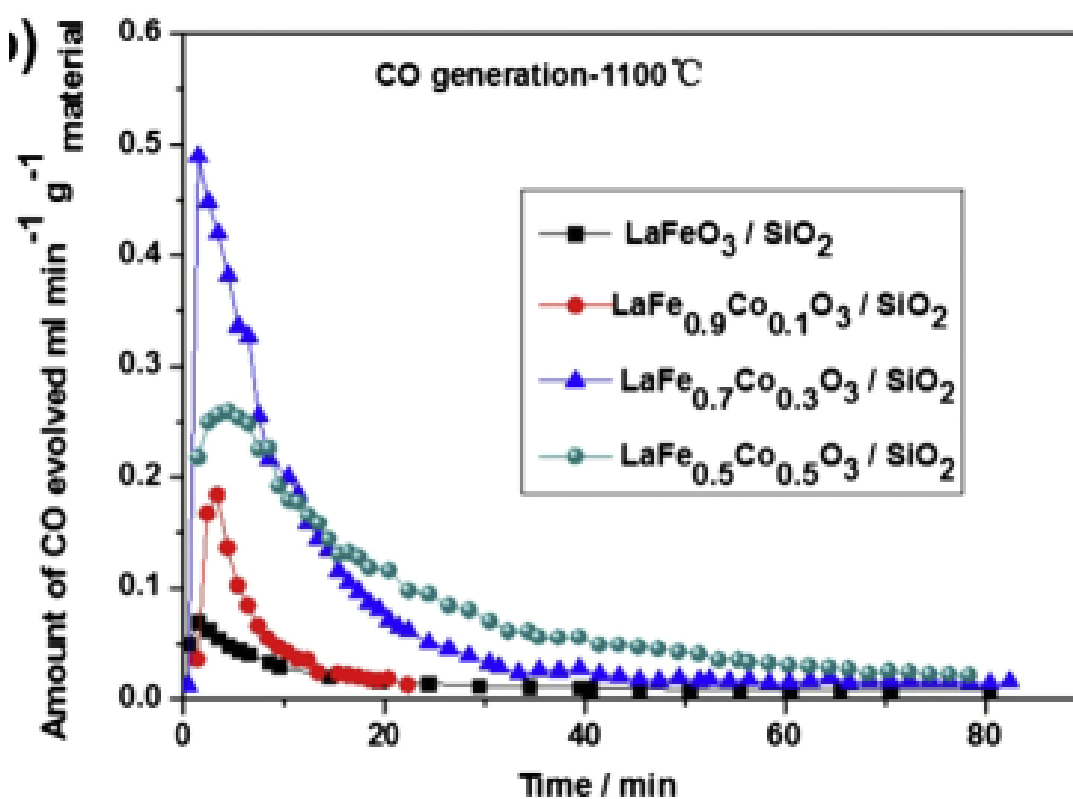


Figure 2.10: Generation rate-time of CO at 1100°C for the perovskite $LaFe_xCo_{1-x}O_3$ at 25%wt on SiO_2 with $x=0.5,0.7,0.9,1$ [53].

the different cobalt doping tests, as well as the production of supported perovskite without doping.

A-site substitution by alkaline earth ions

By the replacement of A-sites with alkaline earth ions, Yang et al. [54] have reached higher oxygen non-stoichiometries than the ceria at equal partial oxygen pressures, subject to reduction temperatures of 1500 °C, in particular, it refers to $La_{0.65}Sr_{0.35}MnO_3$, this phenomenon is certainly influenced by the greater negativity of Gibbs free energy at certain temperature conditions. The figures 2.11 show in 4 cycles respectively the oxygen released in thermal reduction and the hydrogen produced, in this case, the splitting consisted of the production of H_2 from water. The study by Yang et al. concluded that the increase in Sr leads to an increase in the degree of reduction by decreasing oxidation capacity and consequently the production of H_2 . Another class of perovskites studied by Dey et al. [55] with composition $La_{1-x}Ca_xMnO_3$ with variable x of value 0.35, 0.5, and 0.65 have always been studied to split CO_2 and water. In this case, the increase in calcium allowed a decrease of temperatures and an increase in the degree of reduction. The reduction was set at 1400°C with consequent production of 109 $\mu mol/g$ of oxygen for LCM x=0.35, 315 $\mu mol/g$ for LCM x=0.50, and 653 $\mu mol/g$ for LCM with x=0.65. That is an oxygen production of 1.6 times that of the corresponding LSM and 5 times greater than the most well-known that under such conditions has reached an oxygen production of 112 $\mu mol/g$. Dey et al. then compared these perovskites to another factor that has proven influential in transport capacity: the arrangement of atoms in the lattice. LCMs perovskites are orthorhombic, unlike LSMs that have a rhombohedral structure. The figure 2.12 shows just how calcium doping increases kinetics more pronounced than Sr which instead has a production less than O_2 in reduction and at lower intensity peaks with a noticeable delay even in the time of transformation of the material. The study made it possible to determine the CO yields produced after the reduction of LCM perovskites with x = 35, 50, and 65. The results are yields of 175, 525, and 810 $\mu mol/g$ respectively. Again, yields are much better than in the LSM. A peak of re-oxidation for LCM65 has still been noted divided into two different timelines, firstly a part corresponding to a rapid mass growth given by a reaction-controlled regime, following a slower and more constant growth corresponding to a phenomenon in a diffusion-controlled regime. In any case, it has been shown that reversibility in the production is of both O_2 and CO is established, although re-oxidation kinetics

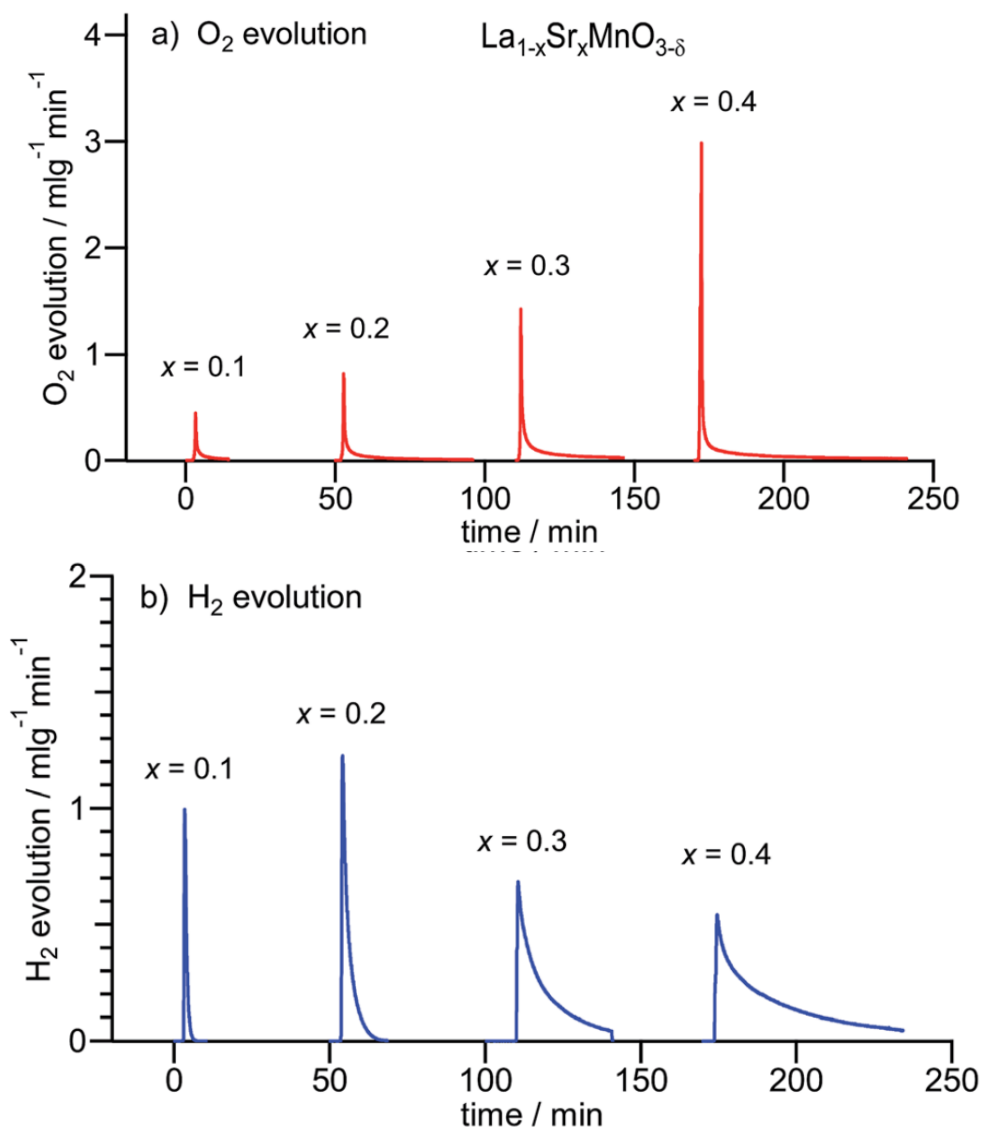


Figure 2.11: Evolution of production of oxygen (a) and hydrogen (b) of the perovskite $La_{1-x}Sr_xMnO_{3-\delta}$ with different concentration of Sr [54]. Different peaks were positioned in series on a x-axis to have better comparison of the time needed for each reaction to occur.

seems to decrease in repeated cycles. However, morphology does not appear to have changed after TGA studies, and perovskites with orthorhombic configuration have superior characteristics to rhombohedral ones. Dey et al. conclude their study with

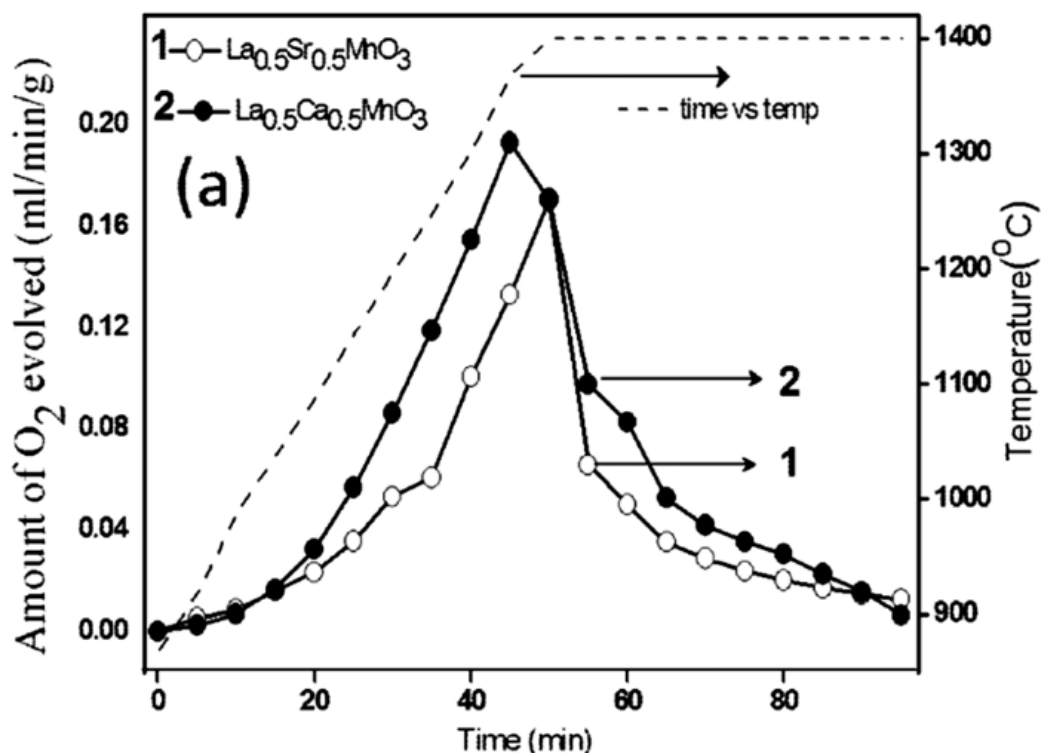


Figure 2.12: Evolution of oxygen in perovskite $La_{0.5}Sr_{0.5}MnO_3$ and $La_{0.5}Ca_{0.5}MnO_3$ [55].

tests on $La_{1-x}MnO_3$ ($x=0.1$) which has high concentrations of Mn^{4+} ions instead of Mn^{3+} ions as the most common in the presence of doping. Unfortunately, with this composition of the material at high temperatures, there is a transition from the orthorhombic to tetragonal that as mentioned above modifies the performance reducing yields and reactivity of the material in general. Similarly, perovskites of the type $La_{1-x}Ba_xMnO_3$ have been studied, classified according to the acronym LMBx with $x=0.35$ and 0.5 . Rao et al. [56] report the main results obtained, which do not excel compared to other materials already described: for example, LBM50 produces less O_2 than the LSM50 and LCM50 counterparts. It can be noted that instead, LBM35 produces an amount of O_2 comparable with LCM35. CO_2 splitting performance, on the other hand, is not significantly increased. Other more recent studies have focused on the chemical looping capabilities of perovskites intending to be used for reforming processes. Jiang et al. [57] studied the feasibility of an

applied SMR process by providing heat through a solar system, thus managing to find the necessary heat from a renewable source. The process to produce hydrogen was carried out through redox cycles completed by a perovskite oxygen carrier, thus defining the demonstration setup as solar-driven chemical looping steam methane reforming (S-CL-SMR). This study is significant for the current work as it provides important information regarding the oxidation and reduction characteristics of perovskites based on lanthanum, calcium, nickel, and copper. Both reactivity and cycle regenerability in the material has been evaluated, which are typically dependent on oxygen exchange capacity and the starting temperature of oxygen release. For this evaluation, the researchers addressed a temperature-programmed reduction TPR in the presence of H_2 developed through a thermogravimetry analysis (TGA), releasing 20 ml/min at 5% H_2/N_2 as a reducing gas for a 10 mg of mass sample. From room temperature, a growth ramp of 5 °C/min was chosen from room temperature to reach 600°C. Taking into account doping at different concentrations of Calcium in the A-site has shown how as the concentration of calcium increases the specific surface area, from the Brunauer–Emmett–Teller (BET) model, it is also increasing from 4,604 m^2/g for $LaNiO_3$ without calcium to 5,295 m^2/g for $La_{0.1}Ca_{0.9}Ni_{0.9}Cu_{0.1}O_3$. A similar trend was found in the average pore diameter, which increased from 3,794 nm to 5,016 nm. Calcium then brings a distortion of the lattice, being less radius than lanthanum, making it easier to generate oxygen vacancies. By providing to a higher gas contact area, calcium doping allows for the overall reactivity of the material. An XRD analysis then saw how the Ca and Cu ions are very homogeneously absorbed into the structural lattice. There are two stages of reduction of this material: the first stage occurs with the absorption of surface oxygen, the second instead involves sub-stoichiometric absorption in the lattice. In the figure 2.13 is possible to see the two different reduction stages performed with H_2 for the different materials tested. Increasing the amount of calcium, the peak is most pronounced for both the surface absorption part and the absorption in the lattice, also the presence of calcium manages to reduce the starting temperatures of the reactions. The TGA curves provided for the same material set confirm the best oxygen release performance of the $La_{0.1}Ca_{0.9}Ni_{0.9}Cu_{0.1}O_3$ which results in a 5% decrease in mass in the first step and 11% in the second reduction step, determining the best conditions among the different materials tested. TGA

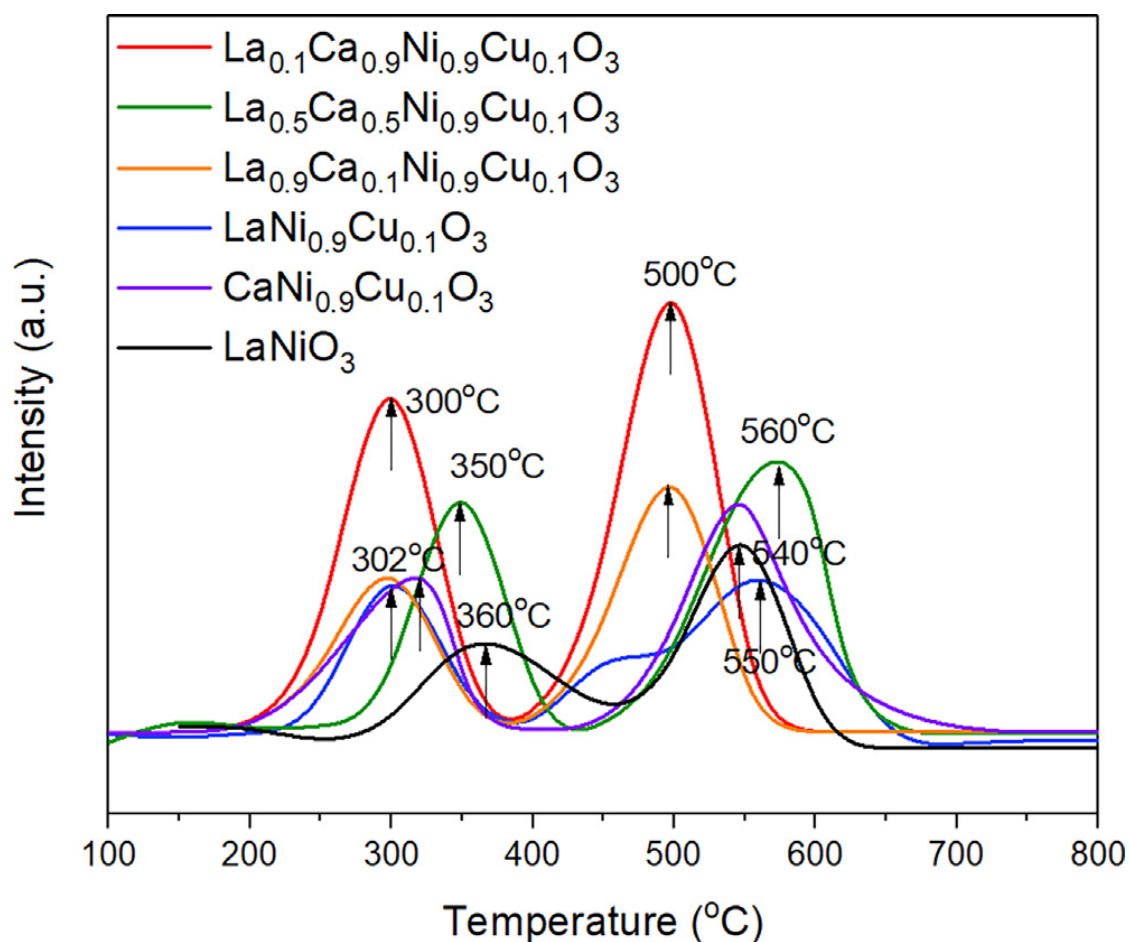


Figure 2.13: H₂-TPR results of different perovskites studied by [57].

curves are shown in the figure 2.14. The same authors compared this data to those of other studies on perovskites [58] of type $La_{1.6}Sr_{0.4}FeCoO_6$, where a maximum mass variation of 8.5% shown in the figure was seen 2.15. Other studies on perovskites have focused instead on supporting materials such as Hare et al. [59] that proposed a $La_{0.75}Sr_{0.25}FeO_3$ (LSF) perovskite oxide combined with various media that also includes classic materials for redox reactions such as CeO_2 and ZrO_2 in parallel with other alternatives including Al_2O_3 , SiO_2 , and TiO_2 . The differences between these materials are highlighted in Hare et al.'s study. They were highlighted in compliance with possible advantages given by the creation of a network of diffusion of the gas through the mass of the lattice, which takes place for example during the cleavage of the C-O bond, in the process of reducing CO_2 ,

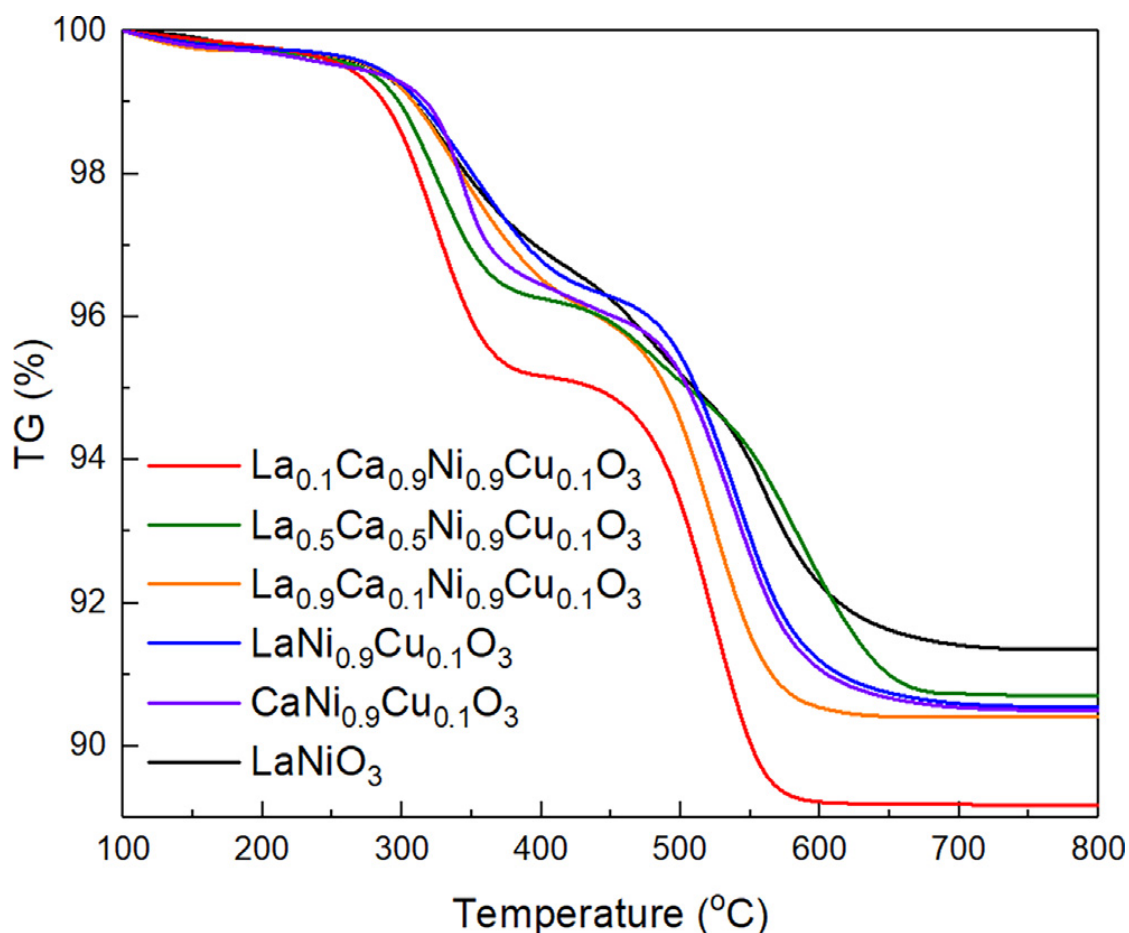


Figure 2.14: Results of different TGA test of $La_{1-y}Ca_yNi_{0.9}Cu_{0.1}O_3$ performed in H₂-TPR [57].

on the surface of the catalyst resulting in the oxygen atom spreading within the mass of the lattice reopening the active catalytic site for a further decomposition of another CO_2 molecule. To provide an improvement to this process, the introduction of support material is suggested by the possible best performance of perovskite which sees the surface area increases and accelerates the phenomenon of oxygen diffusion. Several temperature-programmed experiments were carried out in a quartz microreactor in which about 75 mg of material was introduced for each test crossed by a flow of 50 scm. The reduction part (TPR) was conducted by identifying the reduction temperature for each test material following a temperature ramp of up to 950°C with an increased rate of 10 K/min in a 10% H_2/He (v/v)

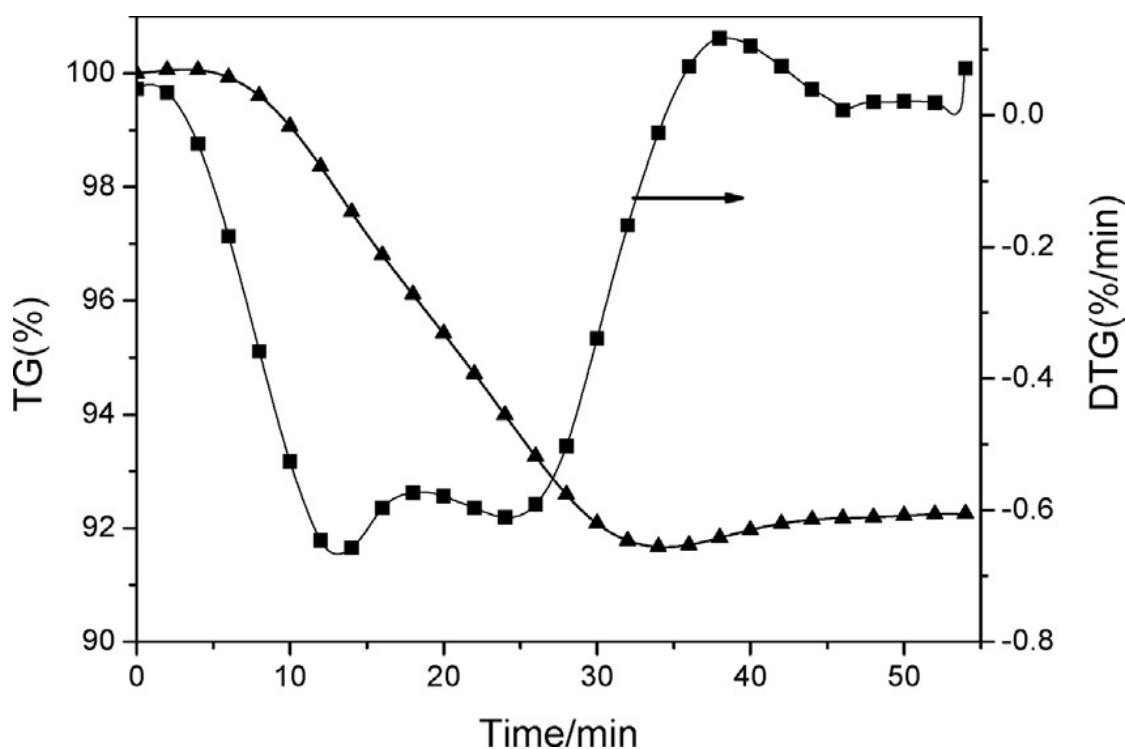


Figure 2.15: Mass change and DTG plot of perovskite $La_{1.6}Sr_{0.4}FeCoO_6$ from [58].

environment. Temperature-programmed oxidation (TPO) then followed up starting with an isothermal temperature of 600°C by 30 min with the previous H_2 flow and then changing the stream to $10\% CO_2/He$ returning to the ramp from 600 to 950°C with the same rate of 10 K/min faced for the reduction. The figure 2.16(a) shows the results obtained from each supported perovskite (colored lines) and perovskite without support (black line). It can be seen that for each of the materials the formation of oxygen vacancies can occur, in particular, the peaks below 700°C of temperature are attributed to the partial reduction of the perovskite phase (from ABO_3 to $ABO_{3-\delta}$) while the subsequent more intense peaks are attributed instead to the decomposition of perovskite into binary oxides such as FeO . The result is therefore that a good temperature for the reduction settles around 600°C to create active sites for the decomposition of CO_2 without altering the material. The figure 2.16(b) shows the oxidative behavior of materials with CO production in an isothermal environment at 600°C . From here you can see how the use of

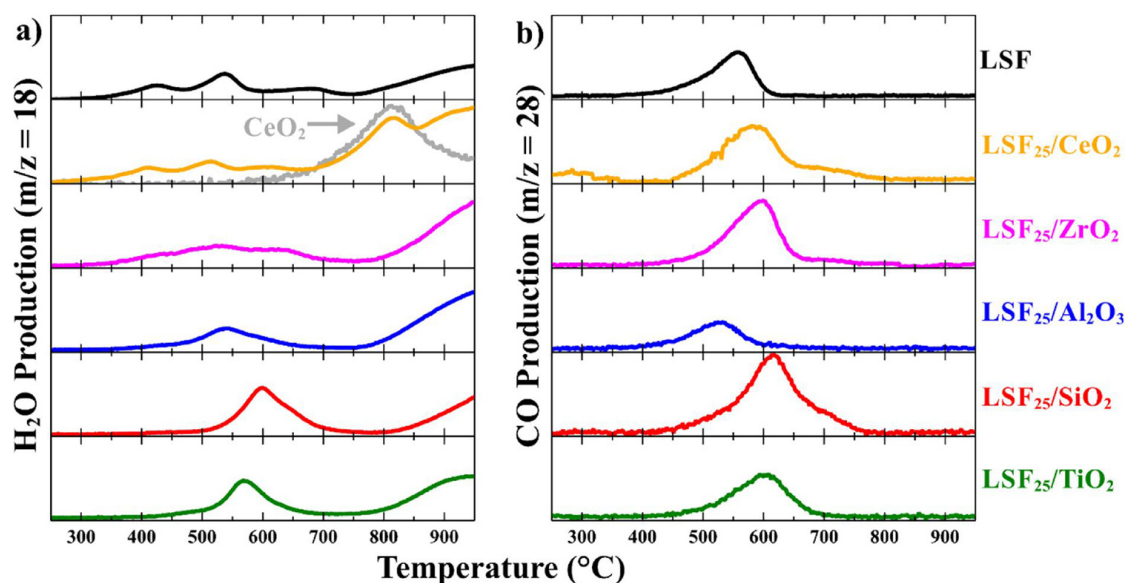


Figure 2.16: Temperature programmed reduction in H_2 (a), followed by temperature programmed oxidation in CO_2 (b) [59].

Al_2O_3 as support is harmful to the redox properties of the LSF which together with the TiO_2 support makes vacancies training less likely by creating transport restrictions making the catalytic task more difficult. Conversely, the greatest success in supporting SiO_2 is highlighted, which emphasizes CO production by arriving at a yield calculated in the study of $1700 \mu mol/g$: an excellent result when compared with the yields of CeO_2 or ZrO_2 .

A-site substitution by rare-earth ions

Alkaline earth ions are not the only possibility of replacing perovskites's A interstitial sites, other ions such as those belonging to elements of the rare earth group have been used as perovskites doping. Hartley et al. [60] compared a type of supported perovskite on a stainless steel chip with Zr and Cr doped ceria on the same stand and Al_2O_3 support. The pre-treated surface by annealing has shown that the species deposits on stainless steel. The ceria and perovskite crystals have been confirmed with XRD analysis. In the perovskite supported by Alumina, alumina was revealed to have a 10% presence in the crystal phase. The doping of Zr or Cr can lower the reduction temperatures. Among the most famous families

of perovskites containing alkaline earths ions we find two that have been most successful in the research: the first with a Sr concentration of 0.5 combined with rare earth and the second instead with an equal concentration of Ca instead of Sr. Generic nomination can be for perovskites with Sr and Ca respectively such as $Ln_{0.5}Sr_{0.5}MnO_3$ and $Ln_{0.5}Ca_{0.5}MnO_3$ where Ln represents ions such as A, Nd, Sm, Gd, Dy, Y [56]. It has been found that with the decrease in the size of rare-earth ions, the production of reduced oxygen increases and reaches its peak in tests with the replacement of A-sites with yttrium; $Y_{0.5}Sr_{0.5}MnO_3$ showed a higher oxygen yield than LSMx x=0.5 mentioned in other works, with an oxygen production of $483 \mu mol/g$. Among the materials tested in [61, 62, 63, 64, 65, 66, 60] YCM50 produced the most oxygen with a value of $575 \mu mol/g$. A phenomenon influenced by the size of the ions at the sites is also the oxygen release temperature that decreases as the ion size decreases. In this regard, it was found that YSM50 begins the release at about $860^\circ C$ while YCM50 at $970^\circ C$. Similarly, it follows the behavior for CO productivity which increases as it descends towards smaller rare-earth ions. Again, yttrium-based perovskites allowed greater CO production at $1100^\circ C$ with $671 \mu mol/g$. A further caution can be noted regarding the production of CO for the latter material that does not seem to be particularly influenced by the number of cycles and manages to remain practically unchanged even after several loop tests.

B-sites substitution

A further subchapter wants to be dedicated to the B-site substitution of perovskites. McDaniel et al. [67] bring aluminum replacement back to LSMx, thus defining a new type of material capable of achieving lower oxygen deficiencies than CeO_2 . In particular, they synthesized perovskite $Sr_xLa_{1-x}Mn_yAl_{1-y}O_3$ at two different levels of aluminum concentration: 0.4 and 0.6. The choice of this type derives from the structure of $LaAlO_3$ that is active for redox cycles and stable both under reducing environments and under oxidizing environments. The material created performed better in reduction with lower temperatures than the ceria ($1550^\circ C$) and ferrites ($1400^\circ C$) without losing the opportunity to reoxidation at reasonable temperatures after reduction ($800^\circ C$). The figure 2.17 shows that CO production is much higher for SLMA than for the ceria, in particular, it has been calculated 6 times higher production with the concentration % of CO_2 sent and temperatures

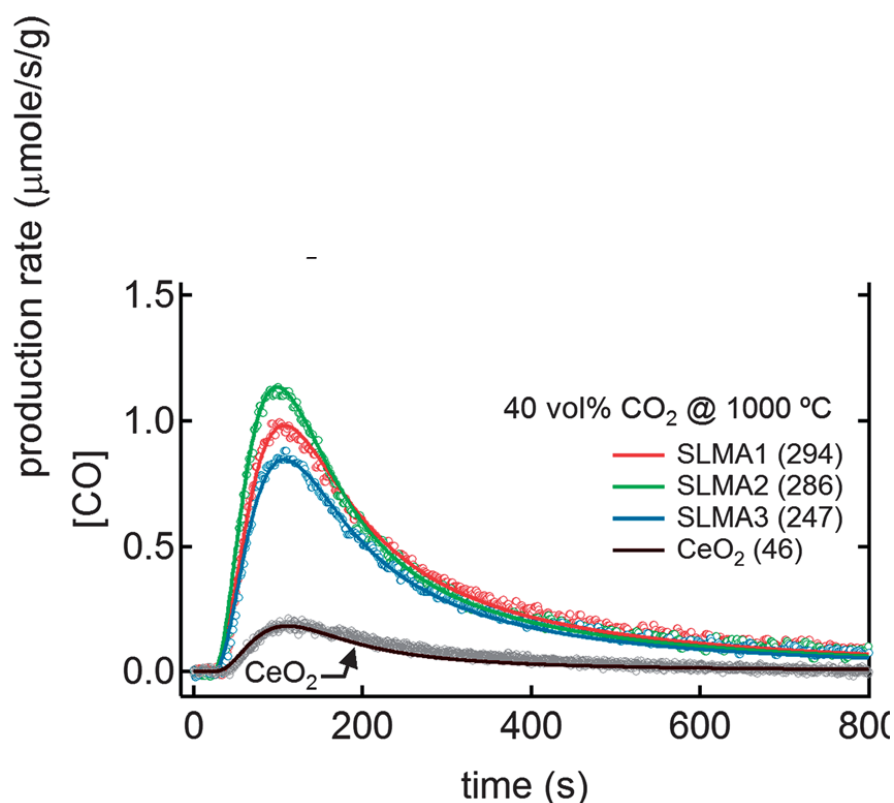


Figure 2.17: Production rates of CO measured in oxidation at 40% CO_2 in volume at 1000°C. All the sample where thermally reduce in He atmosphere at 1350°C. The numbers in the parenthesis represent the total amount of the production [67].

described in the figure. The constant flow of CO_2 for oxidation allows to wipe out the syngas produced and thus achieve better performance, also the same CO_2 flow allows to maintain an ever greater CO_2/CO ratio of 100 that contributes to increasing the kinetics of the phenomenon. The same figure then shows that there are two mechanisms of CO production, the first order based on the exponent $(1 - \alpha)^n$ of the expected kinetic model. This first factor contributes about 75% to total CO production. The second factor is related to a diffusive phenomenon and in the figure is represented by the trail of CO that gradually decreases with time instead of stopping radically. To assess the evancy of the material, a test including 80 redox cycles was evaluated as shown in the figure 2.18 at temperatures of 1350°C for reduction and 1000°C for CO_2 splitting. The constant level of CO produced in this experiment shows an ability of the material not to degrade and

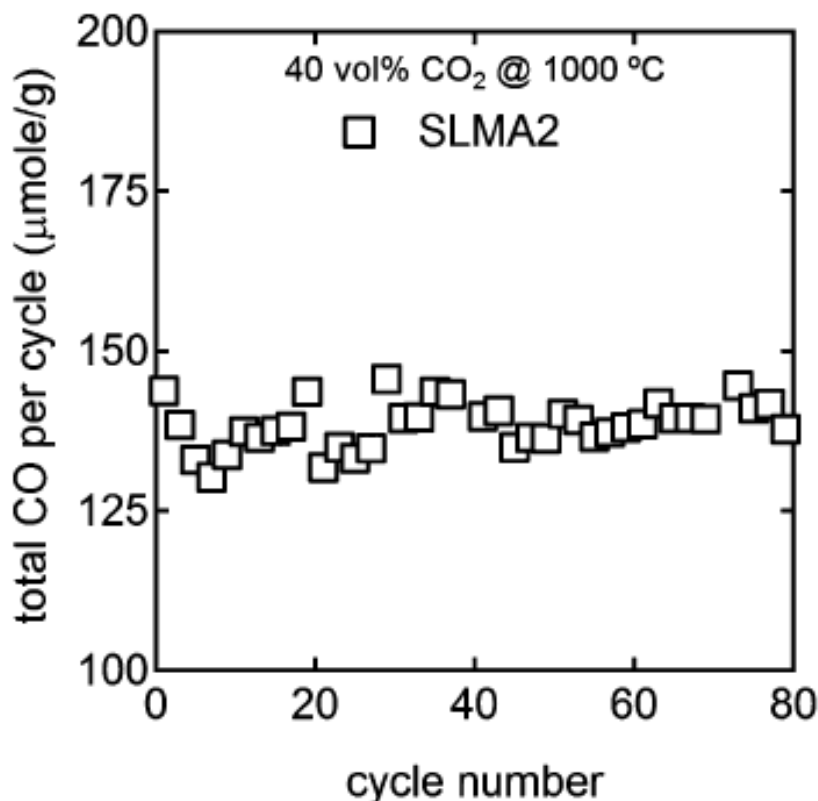


Figure 2.18: Total amount of CO produced in each cycle for SLMA2 with a reduction at 1350°C in He and oxydation in 40% CO₂ in volume at 1000 °C. Each reduction and subsequent oxydation lasts for a total time of 30 minutes divided in 15 min for reduction and 15 min for oxidaiton.

lasts more consecutive tests, thus assuming considerable interest in further studies. These results are also confirmed by Jiang et al. 2.10 where the performance in particular of $LaFe_{0.7}Co_{0.3}O_3$ and $LaFe_{0.7}Mn_{0.3}O_3$, part of the family of lanthanum-ferrite based perovskites, revealed a high oxygen-carrying capacity, with the lack of poor performance regarding CO₂ splitting, then increased with the use of metal oxide-based supports.

Gálvez et al. [68] conducted different studies concerning the doping of B-site with aluminum in perovskites of the type LSM and LCM, synthesizing the new formula $La_{0.6}Ca_{0.4}Mn_{0.6}Al_{0.4}O_3$ which was then subjected to 3 consecutive redox cycles

with thermal reductions and the following re-oxidations with CO_2 . The reduction steps expected temperatures of 1350 and 1450 °C while the oxidation of the material remained at 900 and 1000°C. Among the characterizations of the material carried out, SEM shows the presence of enriched phases in Ca that are presumed to be CaO and CaCO₃. The authors report that the formation of carbonates is increased by excess cations in A-sites, i.e. where the rate of A/B cations is higher. The TGA curves obtained during the reduction to 1350°C followed by oxidation in TPO from 400 to 1200 °C saw the achievement of the balance of the material reduced after 1h, and again the mass increases in re-oxidative phase with the overcoming of the theoretical mass corresponding to the equilibrium at the end of the test. This as evidence of the formation of new phases. The trend of production of nw phases has been more limited in LCMA and LSMA by replacing AL cations into B-sites instead of Mn. The authors also reported that the formation of carbonate species from Ca and Sr is reduced by operating at higher temperatures.

Dey et al. [69] starting from a perovskite similar to the study described above, looking for alternatives to B-site doping with aluminum. In particular, they investigated the effect of Ga and Sr cations in $A_{0.5}Sr_{0.5}Mn_{1-x}A_xO_3$ (as an alternative to Aluminium. Further, performance increases were seen with Ga and Sr, especially the derived material including Sr gave significant fuel yields. The study consisted mainly of TGA with oxide reductions and following CO_2 splitting. The reduction and oxidation temperatures were chosen at 1440°C and 1100°C respectively, leading to the yield of 370 $\mu mol/g$ of CO on average over 3 cycles of LSMA, without noticeable deterioration in performance. Ga^{3+} replaced has a higher yield than the previous one with 447 $\mu mol/g$ of CO produced. Subsequently, again a replacement of Sr^{3+} up to a maximum possible concentration seems to be $x=0.1$ which saw 545 $\mu mol/g$ of CO produced. However, all derivates materials have performed better than LSM. The CO yield of the Ga derivative was 1.5 times that of the consideration derived with Al at similar doping proportions ($x=0.25$). The decrease in yield was shown to be marginally affected with a 15/20% loss in the third cycle. This decrease in yield has been seen in many perovskites and is caused by a lazier kinetics or sintering phenomena. After TGA testing, further analysis showed that the structure of perovskites remained stable at the end of the cycles completed. It was also ensured that there was no weight gain due to the formation of carbonates.

This is true for oxidation at 850 °C compared to the classic at 1100°C, further confirmation that the weight gain is given by CO_2 splitting. Demont et al. [70] focused on perovskites containing Mn by first testing LSM and YSM with site replacement A, and then acting on replacing B sites with doping initially of Al and later in Mg. Production of O_2 was seen to improve for YSM50 which reached 551 $\mu mol/g$ after 45 min at 1400 °C, with a maximum production rate of 1315°C which suggests the possibility of lower reduction temperatures without particularly altering the yield found for the temperatures used in their work. CO production, on the other hand, reached 112 $\mu mol/g$ after 1h at 1050°C for YSM50, at 269 $\mu mol/g$ of LSM50 under the same conditions. Thermodynamics is therefore different as the material changes from A to Y, with worse reduction yields during reoxidation. The reoxidation yield was calculated to be about 10% during the first cycle and 9% during the second cycle, counting only for a small part compared to the oxygen released during the reduction, that is, only part of the matrix can reorganize according to the initial conditions if subjected to CO_2 . The replacement of Al and Mg at Sites B, on the other hand, yielded more optimistic prospects. By decreasing the Sr content, the researchers were able to allow better incorporation of Mg into the matrix, creating perovskites with different concentrations: $La_{0.6}Sr_{0.4}Mn_{0.83}Mg_{0.17}O_{3-\delta}$ (LSM-Mg17) and $LaMn_{0.67}Mg_{0.33}O_{3-\delta}$ (LM-Mg) with minimum or zero Sr content compared to LSM50. Similarly, $La_{0.6}Sr_{0.4}Mn_{0.6}Al_{0.4}O_{3-\delta}$ (LSM-Al40) and $La_{0.6}Sr_{0.4}Mn_{0.4}Al_{0.6}O_{3-\delta}$ (LSM-Al60) have also been synthesized. CO_2 splitting performances were then evaluated in TGA, where a limited amount of oxygen release was seen for pure LM-Mg, resulting in poor CO yields. Overall the reduction appears similar to LSM50 for these new material variants, with reoxidations bringing 196 $\mu mol/g$ and 279 $\mu mol/g$ of Co for LSM-Al40 and LSM-Al60 respectively. However, performance fell dramatically after 2 cycles. Finally, LSM-Mg17 managed to gain the highest CO yield, appearing with smaller particles of an order of magnitude compared to LSM35 and LSM50. This makes LSM-Mg17 a promising material capable of making it similar to LSM50 but with higher resistance to sintering and making itself less sensitive to deactivation after long-term cycles. The largest CO production was seen at 1200°C to 239 $\mu mol/g$, while a huge drop was reported at 900°C. Since re-oxidation is usually favored thermodynamically by temperature drops, the increased CO production observed at higher temperatures may be the

result of dissociation of catalytic CO_2 with oxides spreading in the mass of inner material. Another approach to the redox reactions used by Galinsky et al.[71] is to incorporate perovskite-based support such as lanthanum strontium ferrite (LSF). In this way, the reactivity of the oxygen carrier (Fe_2O_3) is emphasized by at least an order of magnitude compared to classic supports such as TiO_2 , Al_2O_3 , or yttria-stabilized-zirconia (YSZ). The support eases the transport of O^{2-} from the metal oxide to the surface to participate in redox reactions on the surface.

With this part of review of different oxygen carriers for thermochemical applications, it is clear that there is a great interest in the subject especially in the development of new materials that better reflect the needs and restrictions due to the operating conditions of the systems. The search for better performance such as responsiveness, stability at high temperatures, the possibility of shifting reactions to lower temperatures is constant. The physical aspects are also of some importance, among which there is a tendency to create agglomeration and sintering. By increasing the oxygen transport capacity, the reactive properties of the material are increased. As seen in the chapter this is becoming more and more possible with new doping or looking for suitable supports that increase performance. One factor that cannot be left apart to implement these technologies shortly also in the market is certainly the cost of materials. In fact, in addition to the creative processes to obtain the desired concentrations, there is also the question of what materials can be used on a large scale, which must therefore comply with environmental parameters. A well-known example is cobalt, which, while presenting characteristics and potential for improvement in the doped materials of this element, remains, in fact, its use for the synthesis of huge quantities of materials. To avoid economic and possibly also environmental problems related to the placement of these elements in nature, the aim is also to look for functional mixes that include elements more easily available, present in large quantities that can significantly reduce costs. The collection of literature presented so far was also intended to outline in some way a map of the possible alternatives present to date. As seen the attention to materials that possibly avoid a transformation from a solid phase to gas phase is increased by the fact that you can count on some important discoveries that demonstrate the possibility of obtaining yields of syngas produced and released oxygen even considerable, this if is introduced into the material a non-stoichiometry

to increase the reaction kinetics and certainly the transport capabilities. Focusing on perovskites, research is constantly moving. New materials are synthesized to be compared with existing ones. The study of this thesis proposes a perovskite with a non-stoichiometric state and with composition: $Sr_2FeNi_{0.4}Mo_{0.6}O_{6-\delta}$. In the next chapters are reported the method used for the experimental section and the result obtained in each test.

Chapter 3

Experimental Methods

3.1 Thermogravimetry Analysis (TGA) method

One fundamental method for the correct characterization of a Redox reaction is the Thermogravimetry Analysis (TGA) and is a method belonging to the thermal analysis methods focusing on the weight change of a sample in a certain temperature range. When a TGA test is performed, the change of mass is recorded as function of time, along with the change of temperature, or isothermal situation, performed in the same time step. The opposite situation also called “scanning mode” represent instead the weight change of the sample mass as function of temperature. The sample in fact with the fluxing gas, increases or decreases its weight thanks to the interaction of the atoms or molecules contained in the gas with the atoms or molecules that make up the mass of the sample itself. A different gas composition, set at will, can cause a different mass variation in the sample. To give a practical example: a reduction tends to remove atoms or molecules from the mass of the sample. These are transferred to the gas, resulting in a decrease in sample mass. Conversely, an oxidation will see the opposite phenomenon. Some atoms or molecules contained in the gas are transferred to the sample increasing its weight. The main utilization of TGA is under programmed condition, creating a sequence of different steps. Each step is characterized by one or more parameters that have to be chosen depending on the behavior that has to be performed: as example, a dynamic step is composed of a ramp rate in K/min that the temperature has to

follow in order to achieve a predefined value. Also, a target temperature that will represent the end of the step is needed. Another type of step is the isothermal one, characterized by a temperature that has to be maintained for a predefined range of time. The final step is always a protection step: it interferes and stop the step that is performing in that moment if the temperature rises up and exceed the highest temperature set point in the whole sequence.

3.1.1 Components for the measure of mass

Essentially the device consists in an electronic micro balance able to record the changes associated with the sample mass with respect to a reference mass (typically an empty crucible). There are several types of balances that can be adopted in a device to record the mass changes and are divided in two main categories: deflection type balances and null-point type balances. The deflection type can be differentiated in four sub-categories: beam type, helical type, cantilevered beam type and torsion wire type; each of these sub-categories differs from the others in the method of deflection or elongation that is produced [72]. Regarding the null-point type instead, the sensor measures the deviation from the null point and a balance restoration thank to a restoration force is obtained. A schematic of the balance mechanism of the STA2500 machine is shown in figure 3.1.

The sample holder (crucible) has the task of maintaining the mass of the sample inside it during the test; it is removed to be filled with the sample and re-positioned on the plates that support it. They can be made up of different materials: aluminum, platinum and quartz are the most common one, but also stainless steel, glass and graphite are used depending on the type of sample that has to be contained inside and depending also on the different type of test that is intended to be carried out. The shape of the crucible is fundamental to contain correctly the sample and transfer the heat from the furnace to the sample efficiently and uniformly. Thus, there are crucible more suitable for testing liquid materials, and others more suitable for testing solid materials. Is important to notice also that the crucible should not interact with the tested material in order to have reliable result on the TGA test. In figure 3.2 shows the two crucibles. One with the sample mass inside, while the second empty to give the reference to the instrument. The white plates hold the crucibles and under the plates are positioned the thermocouple for the

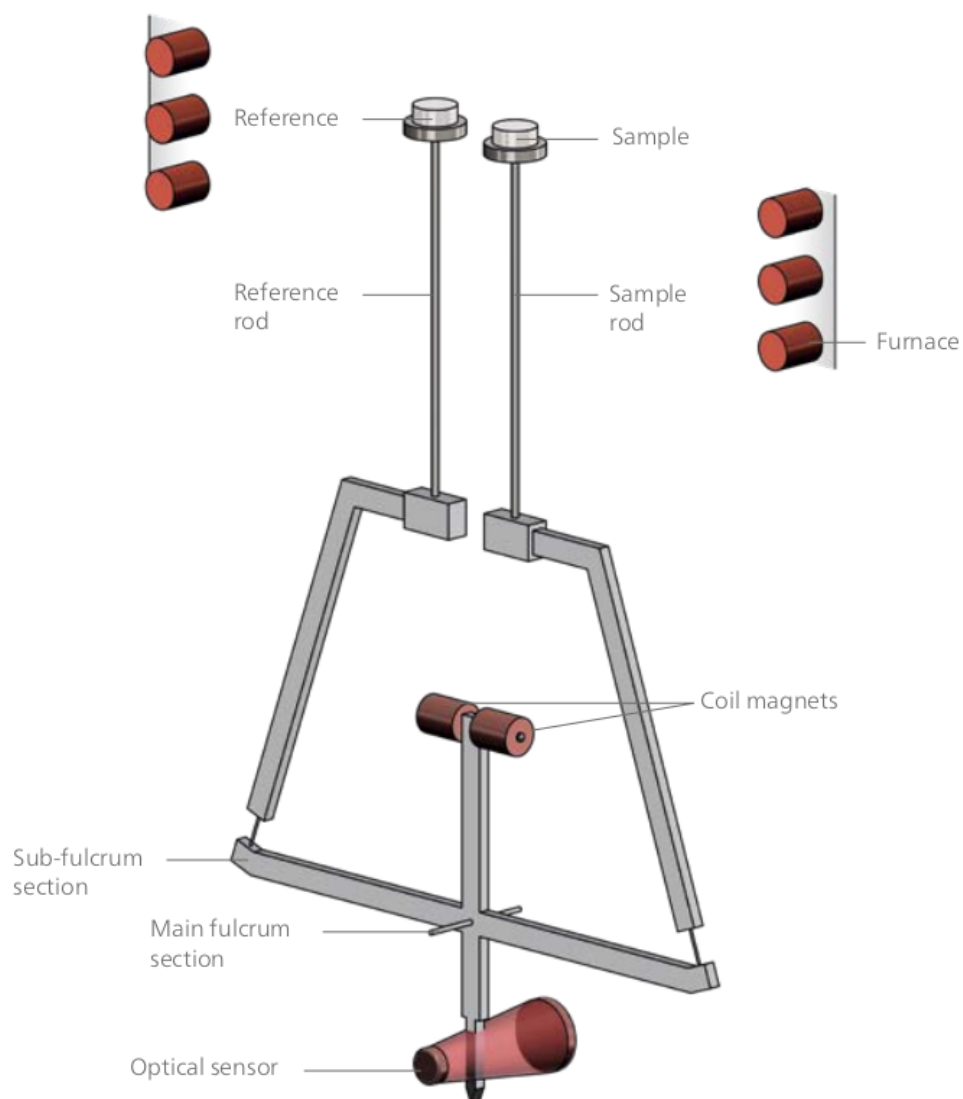


Figure 3.1: Mechanism of the balance inside the TG instrument STA 2500 Regulus [73].

temperature measurement which are in contact with the plate for a more precise measurement.

After these considerations is possible to assert that Platinum crucible able to withstand temperatures of up to 1600 °C and with cylindrical shape can be a good choice for testing the SFNM Perovskites materials. Another component that

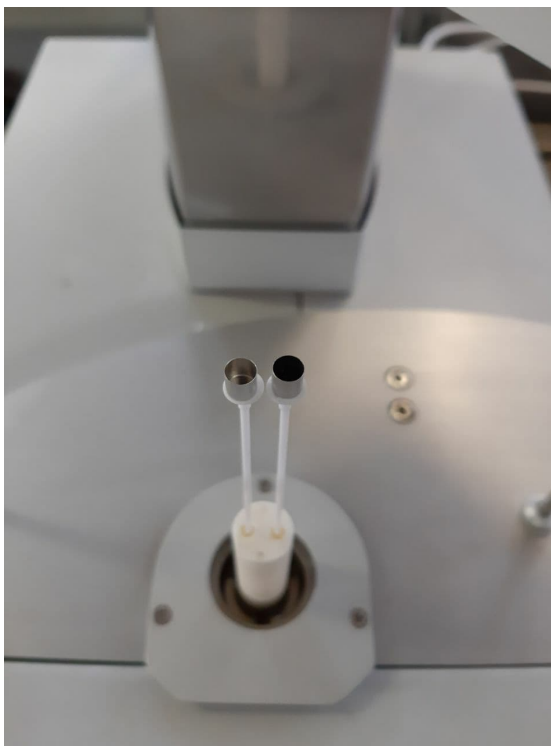


Figure 3.2: Crucibles positioned upon the plates. Thermocouples are under the sample holder in contact with it.

determines the correct functioning of a TGA is the slip-on plate on which it is placed the crucible. As for the crucible, also for this component is possible to locate the best choice of slip-on plate depending on the typology of test and material performed: is possible to choose between standard slip-on plate, large volume slip-on plate types or corrosion-protected slip-on plate. It must be well inserted on the balance rod, and if not dimensioned correctly it can cause micro-oscillations of the crucible that determine a mutation of the registered mass difference with respect to the reference mass. Its other fundamental function is to be, in the STA2500 Regulus machine, the point of direct contact with the thermocouple present inside the sample support rod; with this special configuration, the slip-on plate has to transfer the heat flawlessly from the crucible, otherwise the recorded temperature in the control unit of the machine would be too far from the real value. The temperature measuring is better discussed in the following paragraph. The following paragraphs illustrate more in detail the various components of a TGA

test machine.

3.1.2 Components for the temperature measurement

The furnace is the part of the system that provides heat to the sample and crucible. It consists in a hot zone where the heat should be provided linearly so that the temperature inside the furnace can be considered the same as the crucible and sample temperature. Also, the size of the furnace is responsible for the temperature gradient: low weight furnace can provide quick heating but with more difficulty in controlling temperature gradient. Different heating coils depending on temperature range can be used, with the foresight that no magnetic interaction should arise between the sample and the heating coils.

Thermocouple are used for the measure of the temperature and as mentioned in the above paragraph in the STA 2500 Regulus machine are positioned under the slip-on plate directly in contact with it, which in turn is in contact with the crucible positioned above the plate, this is a typical arrangement useful to capture also the smaller temperature changes. Generally, various materials can be used to build the thermocouples: tungsten and platinum alloys are two types of construction material for these components but typical standard thermocouples are of Nickel and Nickel alloys (types E, J, K, M, T) [74]. In the setup utilized in this work, S-Type thermocouples made of Platinum and Rhodium are present inside the STA 2500 Regulus. Besides the hardware component, the machine is equipped with temperature programmer which deals with the control of the heating rate when a temperature ramp is made and is able to detect when an isothermal step is needed to be maintained adjusting the power and consequently the heat supplied.

3.1.3 Reliability of the data collected in during the TGA

Loganathan et al. [72] describe six main factors that influence the mass change:

- Weight and volume of the sample.
- Physical form of the sample.
- Shape and nature of the sample holder (crucible).

- Atmosphere of the performed analysis.
- Pressure maintained during the analysis.
- Ramp rate of heating or cooling.

However not only a mass change can be seen during a TGA test, in fact the device is also able to perform in the same moment more than one measure: thanks to thermocouple the temperature inside the furnace is also measured as the thermal properties in a differential thermal analysis (DTA). With TGA method are mainly studied phenomena of adsorption, desorption, vaporization, sublimation, decomposition, reduction and oxidation; in particular, the latter two has been studied for the purpose of this thesis and in particular, to rely the setup, in this case has been used the machine NETZSCH STA 2500 Regulus shown in figure 3.3. The result obtained

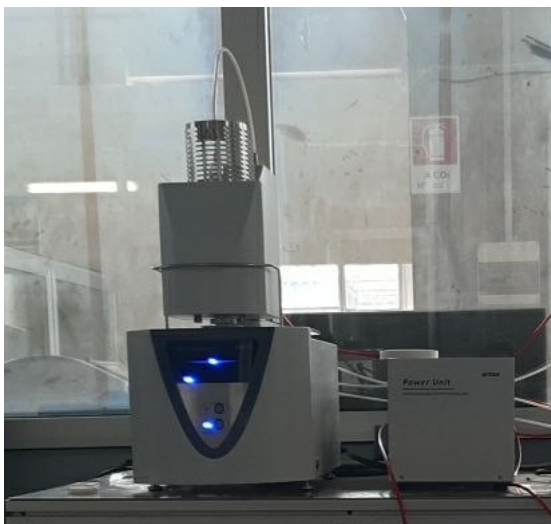


Figure 3.3: STA Regulus 2500 machine.

in a TGA must be interpreted correctly, as many factors may cause a deviation from what we expect, or even provide results that may not seem to describe the phenomenon that is occurring inside the machine. This paragraph is created with the intention of hinting what can be the errors of a TGA, and which methods or tricks are useful to reduce its impacts. STA 2500 Regulus TG present a vertical configuration that allow for a better precision in the measure of mass even if can present more contamination problem due to decomposition of the sample during

the temperature changes. Also, this TG can be categorized in “furnace above the balance” type that include some beneficial effect related to the disturbance of the gases but compromising the maximum sample mass achievable. Buoyancy forces and drag forces from local gas circulation are two important phenomenon that in most of the cases can occur during a TGA and has to be properly taken into account as the gas density is inversely proportional to temperature and that influence in the same way buoyancy. J. Czarnecki [75] describe in its work three forms of buoyancy forces that can be distinguished:

1. weight disturbances;
2. weight oscillations;
3. erratic buoyancy disturbances.

The first type is attributed entirely to the sample, in particular when the tube of the furnace, during the first moments of heating, is hotter than the sample; creating a difference of temperature inside the furnace, a particular circumstance that results in a toroidal circulation of the gases making the instrument to measure more mass with respect to the initial state. The second type of buoyancy can be attributed to the instrument: when the heating power oscillates, temperature gradients will occur locally producing as consequence weight oscillations. This is particular effect that can be controlled by a very smooth temperature control. Different situation occurs for the erratic buoyancy disturbances, which happens mostly with very large sample and high-pressure TG. Here, not a toroidal circulation but instead bubbles-like phenomenon appears presenting different temperatures and so different densities resulting again in buoyancy. This last case does not comply with the necessity to this work because of the little amount of mass used for each experiment. There are several measures that can be made to overcome these problems so that these controversial effects, arisen both in data generation and in data processing can be suppressed or at least minimized. One of them it is seen to be an adequate amount of gas flow in the reactor area and all around in the chamber that prevent temperature and pressure to build up and makes the basement more stable. Another trick is to send every moment a protective flow in the chamber, especially when changing in the gas composition are needed for the

purposes of the analysis with the foresight of maintaining the total amount of gas flow constant and stable during all the process. In a program of TG with samples that decompose creating a contaminating atmosphere, is good custom to not stop the analysis when the TG is run until the end, taking care to add at the end of the entire process one final step of purging gas for some time. Also, regarding the decomposition of the sample during the TGA, the data recorded of the thermal analysis regards only one decomposition (the slowest one) but many of others can occurs in the same time inside the instrument; this is a strong prerequisite for further studies on the material tested with the aim of making kinetic theories that may reflect at best the reality. Moving the focus on the temperature gradient to overcome again instability problem related to the TG, a slow heating rate that is mostly cause of the long time needed to the analysis is also able to give better equilibrium condition reducing all the heat transfer factors. Last, but not less important shrewdness is to perform some “blank runs” before the real test, to stabilize what are the main incongruousness of the TG with the specific experiment and making the reliability of the results more effective by subtracting the “blank” to the real curves thus succeeding in distinguish which are the differences in the result due to the sample and which are due only to the chosen setup.

3.1.4 Gas Spectrometer included in the bench setup

To the TG machine has been added a gas analysis system able to detect in continuous analysis a multiple set of gases and vapors (at the occurrence) at pressure near atmosphere. The range of detection of this component goes from 100 ppb to 100% and is also connected to an external backing pump able to create a vacuum atmosphere up to 2.3×10^{-6} mbar of relative pressure inside. A picture of HIDEN QGA Spectrometer used for the bench setup of this work is shown in figure 3.4. The gas spectrometer work thanks to the conversion of the molecules of gases into charged particles, hence breaking whole molecules into smaller fragments. This operation is possible thanks to a hot filament that can be made up of Thoria or Tungsten which induce a thermionic emission and results in an electron impact ionization; the impact of electron may create different types of ions: molecular ions with a positive charge by loss of an electron, fragment formed after the cleavage of one or more bonds, rearrangement caused by an atomic migration after cleavage,



Figure 3.4: Gas Analysis Spectrometer QGA from Hidden Analytical.

metastable ions that refers to further fragmented ions. Different types of cracking patterns are important information for the analysis. After cracking, the ions can be extracted into the mass filter in which are differentiated and species are selected for detection: in most cases mass filter consist of a Quadrupole, where two pairs of parallel and equidistant metal rods, biased at equal, but with opposite potential are crossed by DC current and RF components able to be varied so that the resulting field produced may vary itself. Ions that enter into the field are deflected accordingly to their charge ratio since the extent of deflection is function of the ion's mass; every interval the RF see through only one ratio allowing to pass only ions that present that particular condition, the others are neutralized impacting on the rods of the quadrupole. As the expected concentration of the CO molecules contained in the gas mixture at the exit of the TGA would have been low, a Faraday detector has been adopted able to have better performance in terms of ions detection with lower concentration. The Faraday Cup is an earthed passive conducting surface able to collect the electrons emitted by an ion during the strike of the ion itself on the cup.

3.1.5 TGA setup created for this study work

The whole bench setup used in this work include the following machines/components:

- STA 2500 Regulus TG machine;
- HIDEN QGA Gas Spectrometer;
- PC for system control and data collection;
- Cylinders and pipes for connections of the various gases used;
- Mass Flow Controller (for the calibration of the Gas Spectrometer).

Inside the TG machine are already included three mass flow controllers for the different input lines: Purge1, Purge2 and Protective. The latter is always present as a flow in order to protect the machine and avoid possible damages caused by the use of the other two lines where can be flushed various types of gases. From the cylinders the gas is sent to the STA 2500 Regulus slightly in pressure to ensure that the flow is able to travel through the entire circuit and is in a range of pressure also suitable for the input line into the spectrometer. Once the gas flow has been processed in the TGA, it exits the machine and the quantity necessary for the Spectrometer is collected to be processed and investigated on the final composition. From the computer has been established both the sequences that needs to be followed by the TGA and the molecules from the TGA exit stream that need to be analyzed by the QGA. In figure 3.5 is shown the schematic of the entire setup bench with the different streams of gases.

3.1.6 Characterization of the material through TPR and TPO analysis

The characterization of reduction and oxidation path has been assessed respectively operating with a temperature programmed reduction (TPR) and a temperature programmed oxidation (TPO). Different experiment has been carried out: both from the reduction and the oxidation section, different conditions has been assessed inside the TG instrument. As mentioned in the first chapter, these materials where

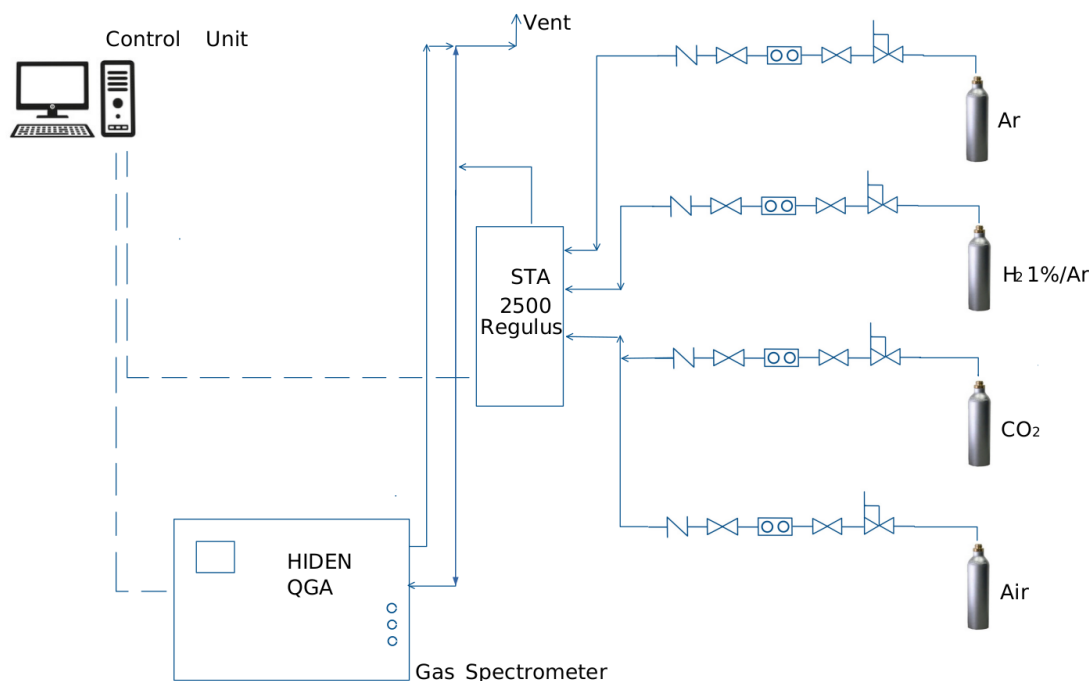


Figure 3.5: Scheme of the setup created for the TG analyses.

already tested from UNIUD as potential material for anode and cathode of SOFC, therefore a previous analysis revealed the conditions of the material subjected to hydrogen reduction in TPR analysis and then the stability in CO_2 environment was already assessed. Differently from the previous study of UNIUD, in this work reductions in 1% of H_2 flow have been performed following TPRs in order to determine in which range of temperature, from 500 to 900 °C, the material reacts with the gas sent in the TG unit. After that TPOs have been performed firstly in air environment then on CO_2 at different concentrations moving from 20 to 40% of molar flow and also one test with 50% of CO_2 has been carried out. Below is reported a generic list of the steps adopted for each test and repeated in loop according to the need to perform more or less cycles in the test itself:

- Pretreatment by dwelling in air at 500°C for 1 hour has been always performed for each single sample used, in order to assure a complete oxidation before the first reduction step.
- Reduction step in 1% H_2 /Ar flow in TPR with a ramp rate of 20 K/min:

this step has been evaluated for temperature ranges from 25 to 900 °C and also from 500 to 900 °C; the second ΔT of 400 °C it turned out to be a good compromise between optimal temperature range of reduction and time necessary to perform the ramp, even if from result showed in chapter 3, better improvement will see a drop of the maximum temperature reached, with the positive consequence of the falling down of time needed to conclude the step.

- Oxidation step performed in Air (21%O₂/N₂) flow for the first tests to assess the effective reactivity of the material with an oxidating agent without the presence of carbon. Then, the evolution of the tests brought to oxidation steps with diversified presences of CO₂ molar flow (20 - 50%) but unlike the reduction steps that were under ramp rate, this time the isothermicity has been maintained at 500 °C in order to improve the reaction of oxidation that is thermodynamically favored under lower temperature conditions as also assessed in the PRIN17 Project Report [76].
- Between each step a purging flow of Argon has been sent into the TG unit to clean from the remaining reducing or oxidating agents before passing to the next step, this to ensure that the two lines utilized respectively for reduction and oxidation will not come into contact creating possible deviations from the expected reactions rather than safety problems related to gas mixtures.

3.2 Microreactor setup with Gas Analysis method

After the TG Analysis, a second path of study has been taken to investigate on the reduction and oxidation characteristics of the SFNM perovskite material: a microreactor setup has been used to see if the result obtained during the TGA could have been shifted in a bigger overview, with more complicated environment and therefore a possible difference in the result. Pohar and Plazl [77] emphasized how the use of microreactors is considered essential for many types of processes, making it possible to miniaturize the latter. The processes developed in microreactors thus prepare the possibility of various types of studies with potential for improving the processes currently used on a larger scale as well as developing new applications. Focusing on this work, this bring to new prospective where the process is more and

more near to real scale system and where possible other phenomena can develop due to different interactions of the perovskites with the fluxed gases in quantities more than double compared to the tests carried out in TGA and also with sample that report a mass of an order of magnitude higher. The bench test setup, schematically

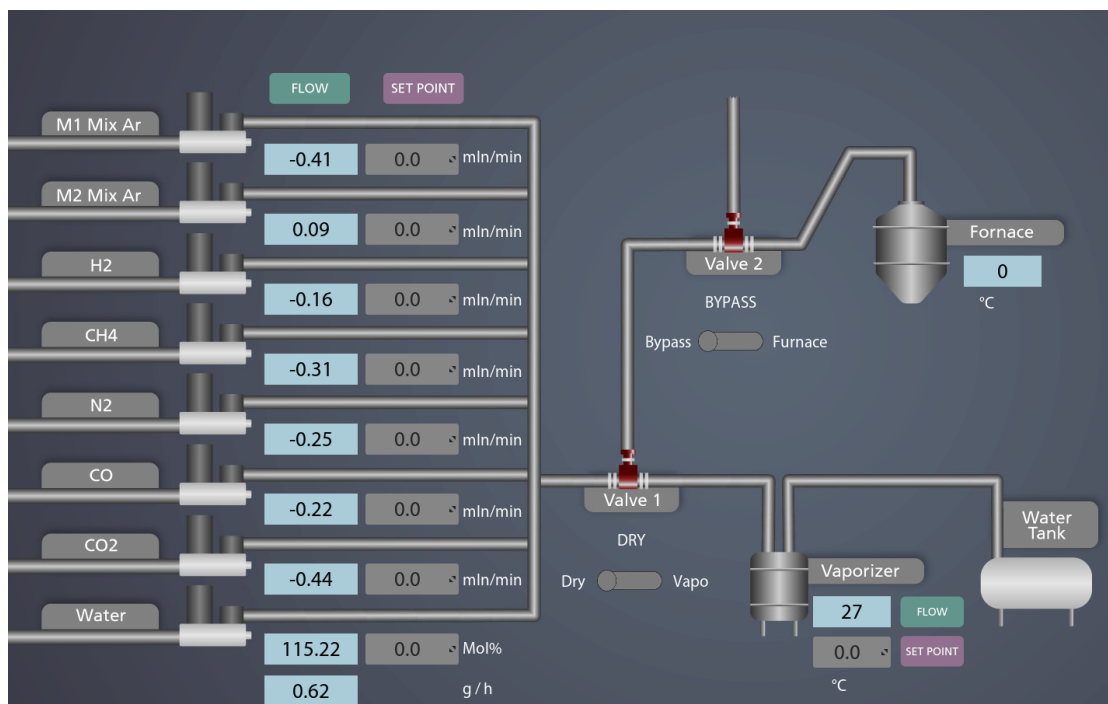


Figure 3.6: Microreactor setup scheme with the gas lines connected to the main stream. Note the two three-way valves: the first for choosing flow in the reactor rather than in the hood, the second determines the choice between dry flow or wet flow.

shown in 3.6 has been arranged with seven gas lines, five of which connected directly to the gas lines of the Laboratory, while the remaining two where connected to cylinders placed under the hood. The typology of gas connected to the setup was: N_2 , CH_4 , CO , CO_2 , H_2 but for our purpose only H_2 , N_2 , CO_2 and water where used. Each gas stream has a mass flow controller (MFC) able to measure and control the flow rate of the gas, so that the right amount of flow can be flushed in the microreactor for each gas in any time when needed. All the streams start with a pressure of 2.5 bar, except for the N_2 that start with a range of pressure from 3.5 up to 5 bar, allowing the latter to pressurize also a demineralized water tank used

(if needed) to create vapor with a vaporizer and flush the vapor in the main stream having as result a humidified stream. Downstream the mass flow controllers the pressure for the rest of the system results to be 1 bar (atmospheric pressure, so the bench test setup is not in pressure). Steel pipes makes the various connection present in the setup; starting from the inlet of the gases, the seven lines are joined into one single stream towards a first three-way valve equipped with pneumatic actuator able to select if the stream has to be dry or wet, then a second three-way valve has been added to choose between directing the stream into the furnace or directly to vent.

3.2.1 The furnace

The furnace is, in some way, the core of the system. Here the reaction of reduction and oxidation take place where the gases meet the material sample in difference concentration and temperature conditions. Figure 3.7 (left) show a picture of



Figure 3.7: On the left, bench setup with with the Carbolite Gero furnace as core component. On the right, power conditioning unit and temperature sequences controller

the Carbolite Gero High temperature horizontal tube electric oven of the system, while 3.7 (right) is the power conditioning unit PCU responsible for the supply of

electricity to the resistances placed in the core of the oven. This energy supplier solves also the function of controlling system for what concerns the temperature programs, allowing to create isothermal steps of temperature by maintaining the set point temperature selected or, instead, create ramp-up or ramp-down steps where the temperature can increase or decrease following the selected rate in degrees with respect to the reference time step. In the inner core part of the furnace, a cylindrical tube forms the reactor zone. As this machine was initially configured for bigger amount of mass samples, the original reactor has an internal diameter of 32 mm and in which has been inserted a secondary alumina (Al_2O_3) tube with a 8 mm of internal diameter; in the latter the sample finds its place in the center of the 1 meter long tube. To ensure the position of the material a quartz wool has been added before and after the sample mass and downstream the sample, also a tertiary alumina tube of 4 mm has been positioned: in this way the pressure created by the gas flow is no longer able to move the sample mass outside the center of the reactor, where the temperature is higher and where redox reactions are expected to develop. An alternative to the tube-in-tube setup has also been adopted, since the pressure created by the gas flow into the inner tube tends to move the sample away from the center of the furnace even with the presence of the quartz wool. So, a new type of sample holder has been chosen consisting in a crucible made of the same material as the tube (alumina). This new holder is essentially a bigger crucible with the shape like a half of cylinder and it is shown in figure 3.8. In this way the



Figure 3.8: SFNM sample under the Al_2O_3 crucible before being inserted in the center of the tubular furnace.

perovskite material is placed into the new crucible geometry and thrust into the center of the furnace. This choice simplify a lot the charge of the reactor and its discharge after the end of the test; also, it is much more similar to the TGA setup but instead of having a gas flux from the bottom to the top, in this case the flux will surround the sample mass in horizontal direction. All the new alumina crucible where pre-treated in temperature to remove the impurities and processing residues. Moving away from the center of the reactor towards the outermost layers a ceramic fiber inner insulation solve as the first temperature barrier, in this way the heat provided by the heating that are inserted from the extrados areas in maintained as much as possible in the inner core, surrounding the ceramic alumina tube. The heating molybdenum disilicide ($MoSi_2$) elements provide three heating zones, this permit a better preheating of the gases that should flow in input into the reactor [78]. After the first ceramic insulation, other two layers of ceramic fiber are present before reaching the outer case, where a last safety equipment composed of a metal grid define the outside shell of the instrument: see 3.9 for an inside-view scheme of the furnace. At the exit of the reactor, the line brings the gas mixture toward a

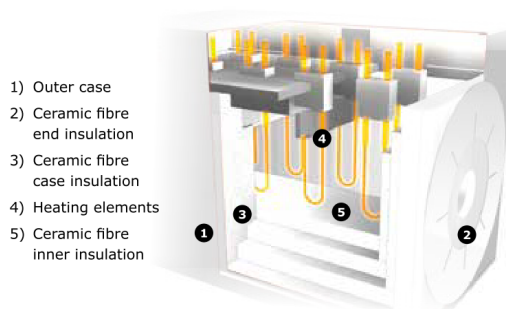


Figure 3.9: Inside overview scheme of the furnace Carbolite Gero [78].

manual selection valve, used to convey the flow to a condenser or directly to vent.

3.2.2 Data collection through Gas Analyzer

As the Gas Analyzer only works with dry mixture of gas, the condenser placed after the furnace can remove all the moisture content into the mixture allowing so the instrument to work correctly without getting damaged. The basic operation of this component is to compare the physical properties of the entering stream with

the properties of a reference gas, making so possible to evaluate the molar fraction of each molecule present in the analyzed stream. For this setup, the Emerson X-Stream XE instrument has been used: this continuous gas analyzer works with two different detectors that has been better discussed below. Using different detector and therefore different gas sensing technologies, allows to more possible gas mixture scenarios where can be adopted enhanced gas sensor calibration, each specific for the mixture to be detected. Liu et al. [79] have classified the most used gas sensing technologies with a review of the main performance indicators such as sensitivity, selectivity, response time, energy consumption, reversibility; also providing comparisons between different techniques adopted. In particular, their classification it had foresaw the division into two main groups, the first inclusive of all techniques based on variation of electrical properties, while the second for the other types of properties. In figure 3.10 is represented the scheme that they have been reported inside the work.

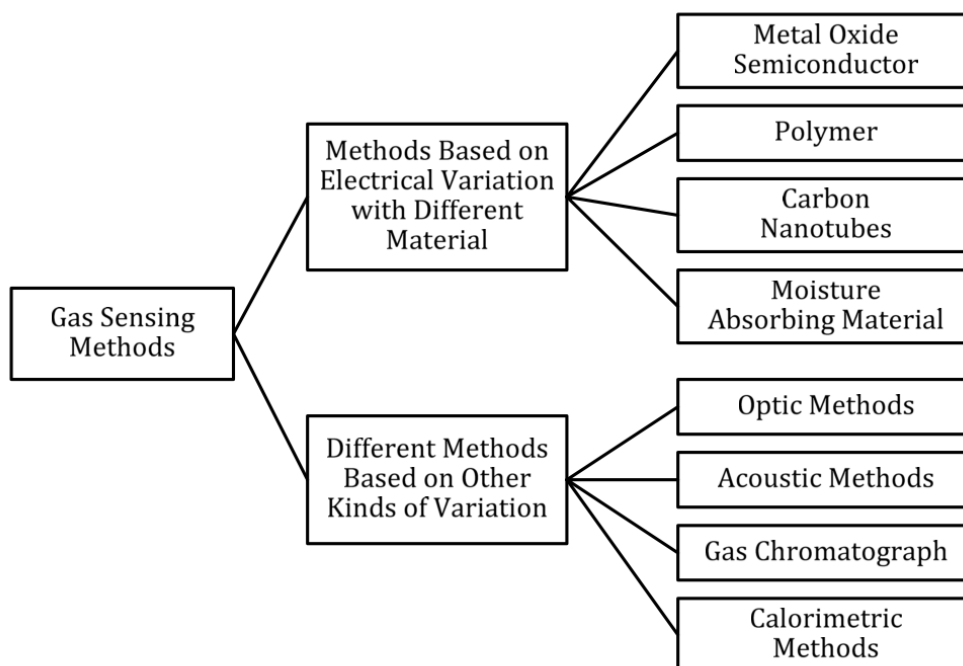


Figure 3.10: Classification of gas sensing methods by [79]

Thermal Conductivity Detectors (TCD)

A thermal conductivity detector, or TCD, is used in gas chromatography and can detect air, hydrogen, carbon monoxide, oxygen and other organic or inorganic compounds, as well as being a method able to provide selective, precise and accurate results [80]. It is non-specific and non-destructive, making it an ideal candidate for a universal detector. TCD instrumentation works best based on differences on thermal conductivity of the sample and carrier gases. Schematically a TCD

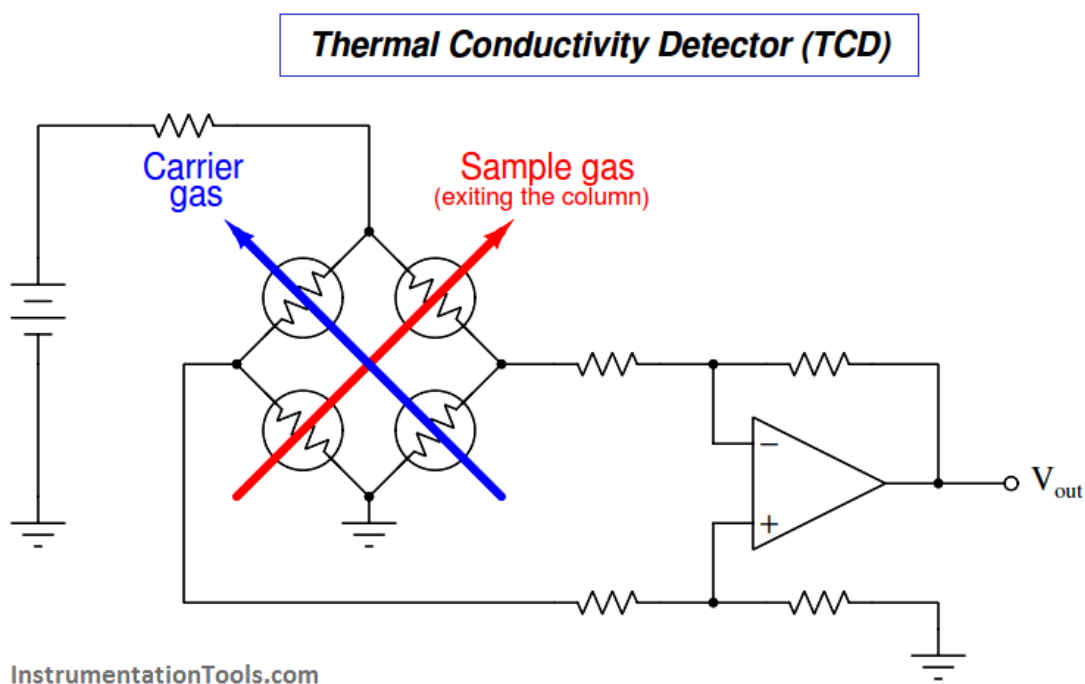


Figure 3.11: Electronic scheme of a TCD detector. Figure taken from the site at the bottom left of the image.

can be represented as the image in 3.11: the pass of the sample gas a carries gas are represented by the blue and red line respectively and the signal detectors are represented as resistances. Each gas enters the instrument into a separate channel, the sample goes to one column and the pure carrier gas goes to the other column. Electrically heated resistance wires are in chambers inside the TCD. A power supply provides current to the resistance's wires, which causes the wires to heat up. The scheme representing the characteristic shape of a TCD is known also as Wheatstone

bridge. As the gas flow to the TCD, the physical properties of the reference gas and the sample gas will allow the wires of the TCD to be cooled at different rates, this change in temperatures will result in change of the resistances from both the reference gas and the sample gas, which produce an electrical signal unique for each compound that is analyzed, this signal is proportional to the concentration of the sample component providing a direct means of measuring component concentrations on a particular sample. Some advantages of TCD can be that are non-specific, non-destructive, and highly responsive to many elements organic and inorganic; also, they can detect many compounds in a single run. Is necessary then to take care about some cons, in fact chemically active compound like acids, halogenated compound or oxidizing substances can corrode the wires of the TCD and lead to thermal damage; if not possible to avoid the flow of such compounds, then a good option is to replace the filament with more frequency [81]. TCDs works best when there are large differences in thermal conductivity between the carrier gas and the sample analyzed, thus analysis of sample possessing thermal conductivity close to the carrier gas will not result in accurate measurement, additionally TCDs have very low sensitivity to organic compound, compared to Flame ionization detectors (FID). As mentioned earlier, temperature is one fundamental parameter for this measurement and together with the gas flow rate is used to determine the correct calibration of the instrument. TCD sensitivity in fact increase with the delta of temperature of the filament with respect to the detector body [82]. Thus, with different temperature there are also differences in the sensitivity of the detector. Is required that the temperature difference remains as much as possible constant. Figure 3.12 shows a typical difference in temperature of the filament with respect to the detector block: where the temperature of the detector is lower, the delta is bigger, and this brings the best result in sensitivity. For this case study, the Emerson X-Stream XE instrument has a TCD only for the H_2 flow stream. The use of a TCD for the hydrogen concentration sampling introduce a typical problem that has to be considered, it has been studied in fact how the hydrogen could develop different results on the detector, not similar to the usual results observed for the other compounds. Some notes from an application reports how Helium, that is typically used as carrier gas, used together with Hydrogen give a low response from the TCD due to the too similar thermal conductivity of the different gases

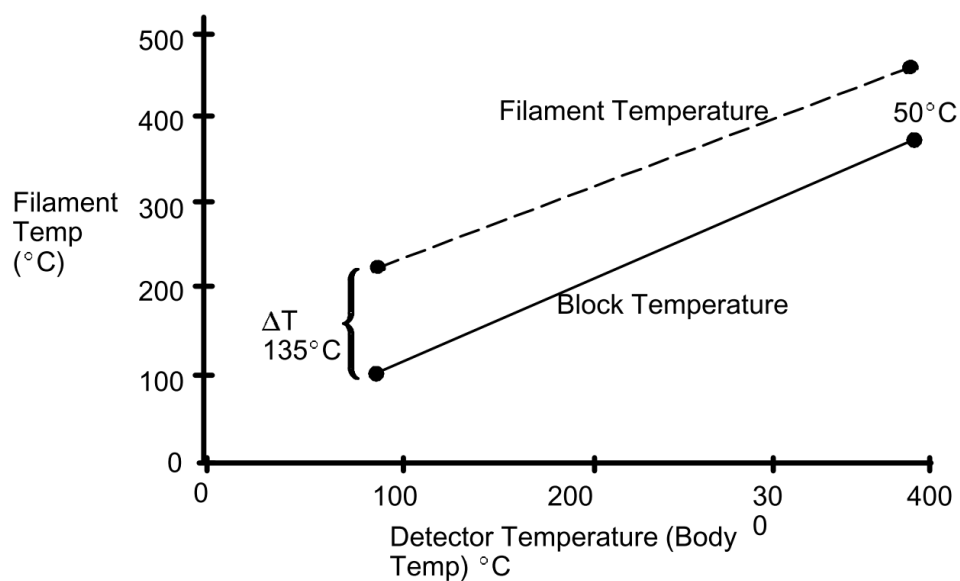


Figure 3.12: Typical differences between the filament temperature and the detector block temperature [82].

[83]. Also, it has been seen how the different concentration of the H_2 in the gas mixture is able to determine a different sign of the signal curve on the detector; in particular for lower concentration the sign of the curve remains positive as for the other compounds, while increasing in $H_2\%$ inside the mixture the thermal conductivity changes bringing to an inversion of the signal. For these reasons, calibration with these phenomena becomes very difficult if the hydrogen percentage present in the mixture exceeds a certain level. To solve this issue, a different carrier gas is needed; therefore Argon or Nitrogen are two possible options even if they both present the problem that switching from helium to these gases, the sensitivity of the detector to hydrogen also decreases noticeably and requires a more detailed calibration.

Infrared (IR) detectors

Quantitative IR analysis is based on Beer's law that may be written simply as:

$$A = \epsilon bc \quad (3.1)$$

where A is absorbance (no units), ϵ is the molar absorptivity with units of $Lmol^{-1}cm^{-1}$ (formerly called the extinction coefficient), b is the path length of the sample, usually expressed in cm, c is the concentration of the compound in solution, expressed in $molL^{-1}$. Calculating the absorbance of a sample using the equation depends on two assumptions:

- The absorbance is directly proportional to the path length of the sample;
- The absorbance is directly proportional to the concentration of the sample.

Chemical and instrumental effects may cause apparent deviations and high values of absorbances. Usually, base line method is employed for quantitative analysis. This typology of study can identify different atomic groups present in chemical compounds. These compounds have a selective absorption in the spectrum region of infrared. So, the atom can vibrate in definite characteristic frequencies. If a thin layer of gas is irradiated with infrared light of all wavelength, some of these wavelengths that corresponds to the vibrational frequencies of the compound are absorbed, while all the others can pass through. As do not exists 2 compounds with same structure, the transmitted spectrum is unique. With these characteristics, the infrared spectrum is largely used and offers a wide possibility for quantitative analysis. The concentration of a single component present in a mixture can be determined by measuring the absorption intensity of its characteristic bands.

In Dispersion-Type infrared instruments the infrared rays are reflected multiple times and the radiation is focused on a slit. The radiation is then converged by mirrors on a thermocouple detector and the amount of energy that the thermocouple receives depend on the degree of absorption that that compound presents. When the absorption is low, the energy will be high and vice versa.

In Non-Dispersion instrument instead, 2 sources of IR are involved. A sample cell allow the passage of the gas, and a second compensating cell is used to determine the background of radiation. The instrument must of course be calibrated with the nearest mixture with respect to the expected mixture. The sample container is filled with the gas at atmospheric pressure and the line from the source to the instrument has to be as short as possible and heated at about $65\text{ }^{\circ}\text{C}$ [84]. In the presence of light gases, such as carbon monoxide, carbon dioxide, nitrogen oxide or ethane is important that the total pressure in the infrared cell is constant

and preferably atmospheric. In fact, a pressure broadening in the CO spectrum has been shown also in a work of Twiss et al. [84]. It has been noticed that the absorbance by carbon monoxide is much less if the pressure is brought to ambient. Other gases such as N_2 has no absorption in the infrared region, so if presents, the effect of these compounds is to increase the response of carbon monoxide to infrared radiation simply by increasing the total pressure. This is the reason why a nitrogen blank spectrum is usually done. After the measurement the net performance of each compound is converted in ppm or mole percent. Also, the moisture infect the instrument by changing the reading values and can also damage the components, for these reasons it is avoided the use of a wet gas and are therefore needed chillers and filters before the input.

3.2.3 Data collected in the microreactor setup

Once all the setup has been connected, a seal test for each experiment has been carried out in order to ensure that the flow rate in input corresponds to the output flow with a reasonable loss less than 10%. After that, the gas sequences and the furnace program has been started at the same time following each other. The output stream is analyzed, depending on the amount of syngas expected, in the gas analyzer or in the gas spectrometer. In particular for SFNM-04 as the CO producibility expected was low, considering the mass involved in the reactions, the HIDEN spectrometer has been selected as the best choice to see the resulting output composition. In order to have data that correspond as much as possible to reality, different calibrations were carried out for each test in order to correlate the result read from the instrument output to the real concentration data. In the figure 3.13 is reported one of the many calibrations done for the different tests. The main variables that affect the reading of the instrument are the mixture of the species contained in the gas, the flow rate at with the mixture exit from the reactor and some sideway of temperature can be also considered. In this case 4 mixture of gas has been fluxed in the machine at the same temperature set-point that would later be used for the experiment. The four calibrations point were tested starting with a mixture without the presence of carbon monoxide and ending with 3% in volume of CO present in the mixture. As can be noticed the calibration data follow a straight line that will be used further after the end of the experiment

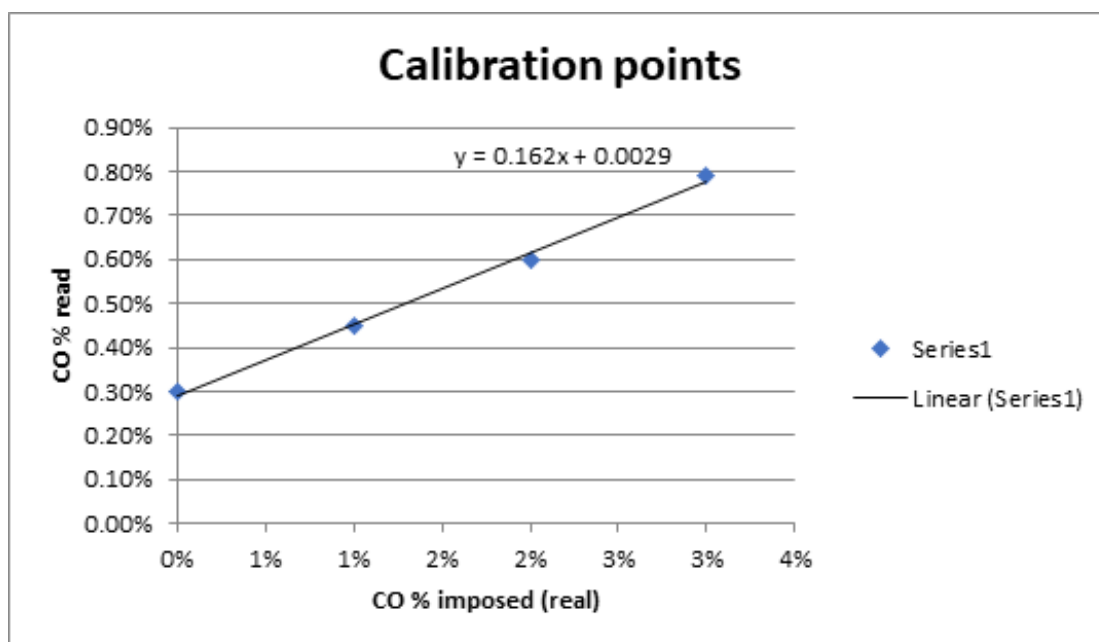


Figure 3.13: Calibration point correlated with a 1st order equation.

in order to shift the data collected and performing an analysis of the number with the real data. Since many test foresaw different temperatures set points involved, as consequence many calibration has been required, providing for each temperature and mixture, the linear curve to retrieve the real data. In fact, initially the first test has been done in order to recreate the nearest condition possible with respect to the TGA, thus allowing to have a confirmation of the results obtained in the first setup, even if the oxidation and reduction conditions of the material were not ideal. The subsequent tests, on the other hand, were designed with a view to improving the parameters of temperature and gas mixtures to allow the material to reduce and oxidize in a more optimal way and to have performance improvements. For this reason instead of swinging the temperature from high in reduction and low in oxidation, has been decided to maintain a constant value of temperature of 850 °C. The following chapter about the experimental result will explain in detail the achievement reached changing the condition and will show the further analysis implemented.

3.2.4 X-ray diffraction (XRD) analysis (post-mortem analysis)

X-ray diffraction analysis is now a key technology in studies aimed at verifying the composition of materials. It is one of the most used analyzes also regarding the transformation of a certain compound by verifying its state from fresh material compared to the post-mortem composition. This small paragraph is intended to give a brief description of this procedure. In an experiment using X-ray diffraction, the sample is placed inside an instrument and illuminated by X-rays. The source and the detector move in a synchronized manner. The detected signal is recorded and represented graphically. The peaks in the graph are characteristic for each individual atomic structure of the sample. The sample crystals are composed of atoms arranged in a particular way with each atom having its own cloud of electrons orbiting around it. Since the wavelength of X-rays is comparable to the distance between atoms in a crystal, diffraction can be used to measure the distance between these atoms. Indeed, when the diffracted X-rays interact, interference phenomena can occur: if the waves are aligned the signal is amplified (constructive interference), vice versa it is destroyed (destructive interference). In a crystalline structure, planes separate atom with well-defined distances and when atom planes are exposed to an X ray beam, the rays are scattered by the spaced atoms. At some angle a strong amplification of the signal could occur, where the scattered waves constructively interfere. The angle between the incident and scattered beam can be called 2Θ . When a constructive interference occurs the distance between the atom and the perpendicular line to the direction of the beam, that pass through the upper atom is $\lambda/2$, as shown in figure 3.14(left). The figure 3.14(right) instead shows the relation between the different dimensions. Applying the sign function is possible to create a link between all the three elements. The equation results the following:

$$\sin(\Theta) = \lambda/(2d) \quad (3.2)$$

And by rearranging this equation, is possible to retrieve the Bragg's Law:

$$n\lambda = 2d \sin(\Theta) \quad (3.3)$$

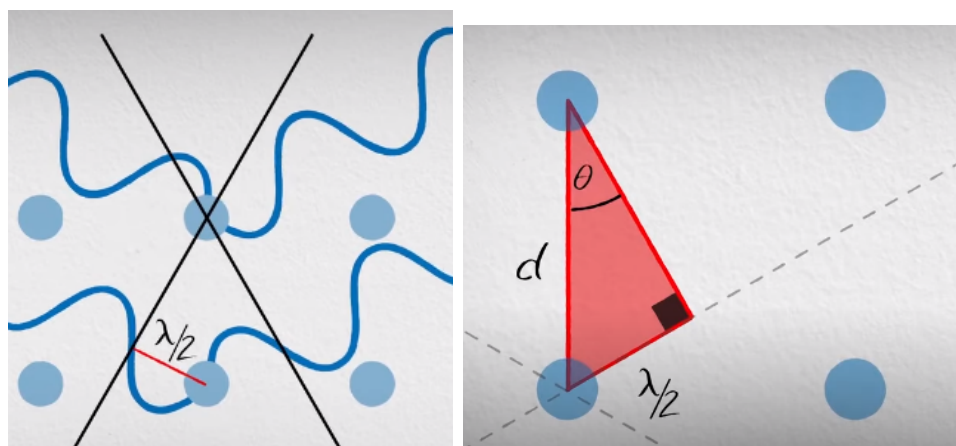


Figure 3.14: On the left: representation of the distances $\lambda/2$ between the atom in the lattice and the perpendicular line to the x-ray beam direction. On the right: representation of the main parameters that determine the Bragg's Law.

This technique of x-ray diffraction is used today for a wide variety of materials: from single crystal thin films, to polycrystalline mixtures and powders and even randomly oriented amorphous material [85, 86, 87]. In this thesis the X-ray analysis has been considered in order to assess the different composition and structure of the SFNM-04 perovskite with respect to its shape as fresh material.

Chapter 4

Presentation and discussion of the results

4.1 SFNM-04 as new material for chemical looping application

The choice of this material was born thanks to the synergy between different research bodies involved in the same project "PRIN17-Direct Biopower" [76]. The first part of the research involves the use of the perovskite structure $Sr_2FeNi_{0.4}Mo_{0.6}O_{6-\delta}$ called also SFNM-04 that is a double perovskite similar to other compositions already studied in literature, with the particularity that is able to self-assemble materials through exsolution process. The transformation done by exsolution creates nanoparticles on the surface that present reversible transformation. The structure of this perovskite transits from a classical cubic structure to a layered Ruddlesden-Popper (RP) structure. This structure presents a general formula $A_{n+1}B_nX_{3n+1}$ or $AX(ABX_3)_n$ that can be described as a perovskite layer followed by rock-salt layers in the outside. This phase has different common aspects with respect to simple (ABO_3) perovskite, as example the rich chemical composition and the oxygen stoichiometries that can change [88]. In figure 4.1 is presented a basic form of RP structure with different "n" layer of perovskite that share at the corners BX_6 octahedra, contained between two layers of rock-salt. The specific form of

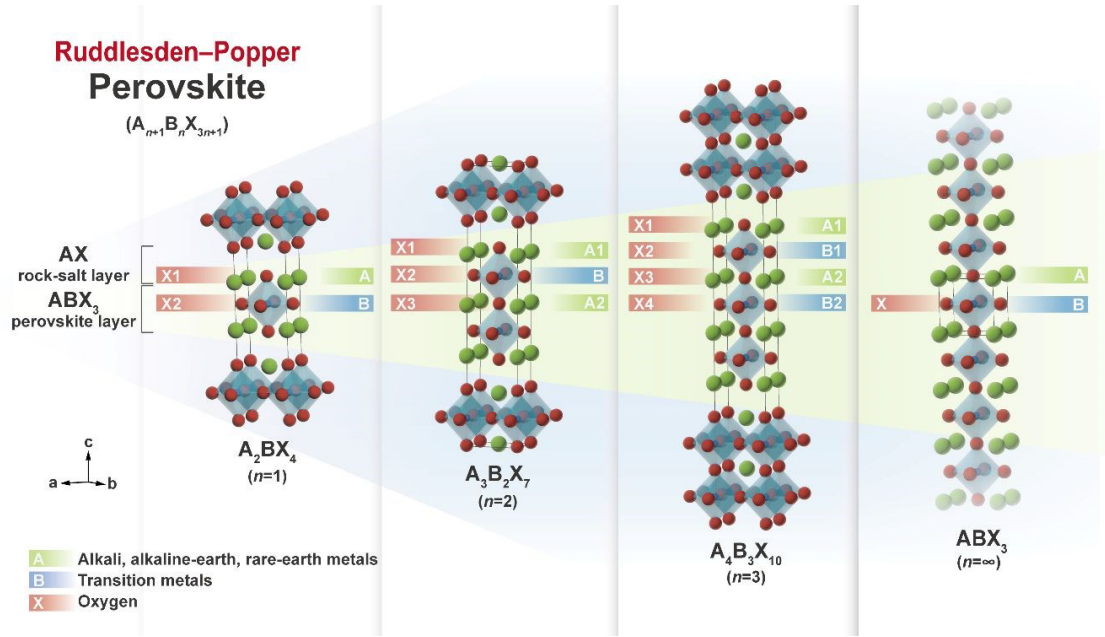


Figure 4.1: Scheme of the Ruddlesden-Popper perovskite structure with different numbers of ABO_3 cubic layer covered by a rock-salt structure [88].

SFNM-04 present a double perovskite structure with the Fe and Mo cation that can arrange in alternative way inside the oxygen octahedra. This material was already studied for SOFC electrode because of its good electronic conductivity due also to the Fe^{2+}/Fe^{3+} transition as well as Mo^{6+}/Mo^{5+} . The high ionic conduction is performed at best in its cubic phase thank to the redox couple non balanced in the structure. This allows the creation of a many oxygen vacancies. Also, the stability at high temperature was assessed without the formation of new compound. In a first assessment after synthetization the material has performed good stability also in oxidant and reductant ambient. Looking more in detail on the composition, the Ni enter in the structure as Ni^{2+} by substituting some of the Fe^{2+} cations. In this way the ratio of the Fe^{3+} cation with respect to Fe^{2+} increase and this help in the conductivity of the nickel. The already mentioned exsolution phenomena is done both from the Ni and Fe that from the lattice comes out up to the surface and assembling by creating new Fe-Ni alloy on the surface in form of nanoparticle. The formation of this alloy is one of the fundamental steps to increase the stability of the material, in fact Fe-Ni is more resistant to sulfide and coke poisoning than just

metallic Ni. XRD analysis of similar perovskite material un-doped has been carried out. On the material Sr_2FeMoO_6 (SFM) a segregation of $SrMoO_4$ has been seen, which are damaging for the electronic conductivity of the material because of the insulant characteristic of this new phase. In figure 4.2 is shown the graph of XRD

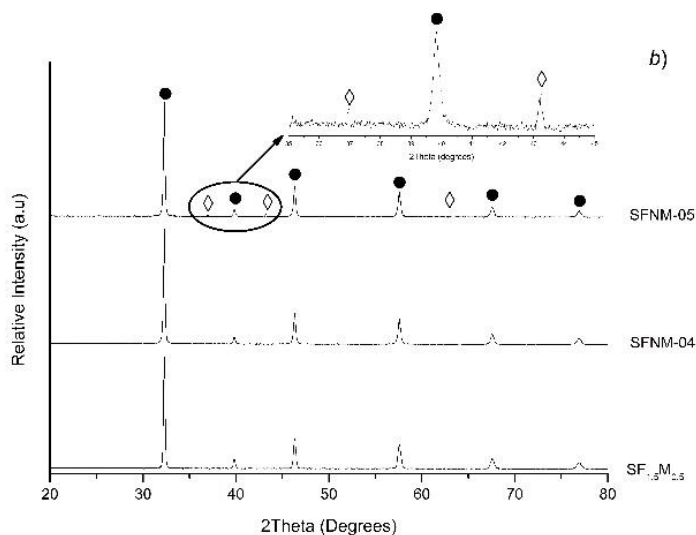


Figure 4.2: XRD spectra of the as synthesized SFNM-04 sample.

pattern for SFNM-04 and SFNM-05 (that has concentration of Ni $x = 0.5$ instead of 0.4). These patterns show the limit of Ni solubility inside the material, in fact in SFNM-05 the highest amount of Ni produce NiO segregation on the surface which it means that not all of the Ni has been positioned correctly into the lattice. For the SFNM-04 no segregation is shown and from this can be deduced that concentration of 0.5 is over the limit of solubility of Ni for the SFM perovskite lattice. After XRD, other analysis has been carried out in order to characterize more in detail the chemical composition of the sample. It has been detected a small quantity of Sr segregated on the surface of SFNM-04. Further, also a TPR analysis on SFNM-04 has been performed in order to investigate on the stability and repeatability of subsequent oxide-reductive cycles. The following list schematize the procedure carried out:

- A pre-treatment raising on 10 K/min until 500 °C in air to remove impurities and other species that could have occurred within the bulk. This same step

has been used to re-oxidize the sample after each reduction section;

- 1 hour of dwelling at 500 °C;
- Real TPR step from 500 to 900 °C at 10 K/min in a reductive ambient at 4.5% H₂/N₂ with a flow rate of 35 ml/min;
- Cool down in N₂ to ambient temperature;
- Re-oxidation described at the first point.

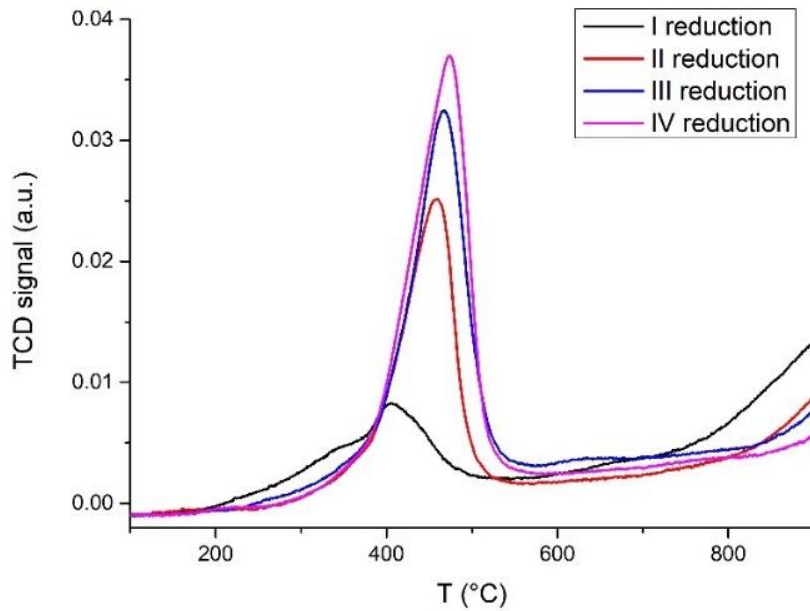


Figure 4.3: First analysis with 4 subsequent reduction and oxidation cycles. [76].

The figure 4.3 shows the result of the TPR tests with a raw signal of the H_2 consumed in each reduction step. The material shows a clear stabilization during the different redox. In the first reduction a transition of the phase ails the reducing capability, then the material improves its performance by enhancing also the H_2 consumption steps after steps. So, the new phase after the first treatment is more stable to reduction. After these tests other XRD have been also performed to assess the transformation of the material after all the treatment. Figure 4.4 show

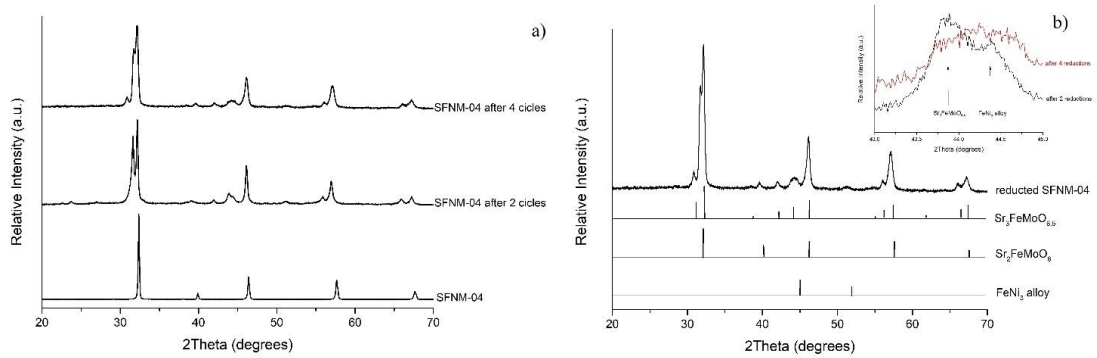


Figure 4.4: (a) XRD spectra of SFNM-04 sample after different cycles in order to assess the evolution of the phase in a reductive environment. (b) Identification in detail of the SFNM-04 after 4 cycles. It is possible to notice a magnification image in 43° and 45° .

XRD pattern of SFNM-04 as fresh sample, after 2 and after 4 loops. The transition of the material is clearly visible. Already at the second reduction the RP phase is present concurrently with the double perovskite phase. In addition, also new alloy takes place in form of $FeNi_3$ probably thanks to exsolution process during the reduction of the sample. So it is possible to predict that the H_2 causes the reduction of the Fe and Ni cation and their migration up to the surface where they can bond together forming the new alloy. In particular the signal that is attributed to the FeNi alloy is at 44.5° . In figure 4.4(b) a magnification of the graph shows better the signal described. The area near the 43.8° grows so, the signal of RP structure is also overestimated due to the FeNi alloy signal. The increment of H_2 consumption at $450^\circ C$ as shown in figure 4.3 so, can be attributed to the reduction of the new alloy whereupon Fe^{3+} and Mo^{6+} in the RP structure. After the reduction stability assessment, the CO_2 environment has been tested. The presence of nickel in the SFM should accelerate the formation of $SrCO_3$ thanks to the reaction of the CO_2 with SrO. This will cause a consequent stabilization of $SrMoO_4$ insulant composition. It is necessary to say that how the nickel acts exactly in order to perform the job just described has not been demonstrated yet. The CO_2 environment was not in the gas flow, that was instead biogas, but is a consequence of the transformation of the biogas in contact with the sample. As originally the perovskite has been designed for SOFC/SOEC application. It is interesting to notice

that $SrMoO_4$ compound has been found in SFNM-04 also after 1 year from its first synthesizing due to the CO_2 present in the air environment where it has been placed. Otherwise, a 30% of propane/ N_2 flow at $800^\circ C$ is sufficient to create the compound cited after 2 hours of dwell. This demonstrate the instability of the SFNM-04 in a hydrocarbon environment that crack with consequent formation of CO_2 . The positive perspective is that has been seen that carbonate $SrCO_3$ disappear with the thermal treatment in N_2 at $800^\circ C$. Also, $SrMoO_4$ after the treatment appear to decrease strongly. After this treatment a further calcination in air at $900^\circ C$ is able to reconstruct the original phase of the material, by reabsorbing the cubic phase $SrMoO_4$ inside the double perovskite lattice. Other catalytic tests has been performed to assess the behavior in oxy-dry reforming in a 80 ml/min flux of $CH_4 : CO_2 = 3:2$. After pre-reducing the sample in H_2 at $800^\circ C$ for 1 hour, the temperature set point has been set to $700^\circ C$ for about 12 hours keeping the sample in a reducing environment. The oxy-dry reforming reaction starts at $700^\circ C$. The CO_2 conversion has an inflection and after that an increase of the methane conversion, suggesting a direct combustion with the oxygen. After $650^\circ C$ both CO_2 and CH_4 conversion are decreased. In general, a low catalytic activity in oxy-dry reforming has been seen, this can be also caused by the low surface area of the sample.

4.2 Experimental analysis: TG characterization

This section describes the different tests performed. The table 4.1 summarizes them in chronological order as they were performed. The following subsections

Test ID	Test characteristics	subsection n°
WHITE1	white curve of the crucible	4.2.1
PRE1	Air pre-treatment of the sample	4.2.2
TPR1	TPR 1 cycle, no re-oxidation	4.2.3
TPR4-air	TPR 4 loop, re-oxidation in Air	4.2.4
TPR4-50%CO ₂	TPR 4 loop, re-oxidation 50%CO ₂ /N ₂	4.2.5
TPR10	TPR 10 loop, re-oxidation in 20%CO ₂ /N ₂	4.2.6
TPR6-oxy	TPR 6 loop, final longer oxidation step	4.2.7
TRP6-oxy/red	TPE 6 loop, last longer reduction	4.2.8

Table 4.1: Summary table of tests conducted in TGA.

presents in detail the test performed.

4.2.1 Test WHITE1: white curve of the crucible

The first set of tests has been conducted in TGA. The firsts experiments are useful to understand the response of the system to the environment composed of the different gas mixtures chosen. In order to verify that the platinum crucible won't affect the result it has been necessary to see what the TG instrument is measuring when no sample mass is present when performing a loop. For this test, the following flows has been used:

- Start with 5 min only Argon protective flow at ambient temperature;
- Dynamic step with a temperature ramp of 10 K/min until 500 °C in a total flow of 40 ml/min of Ar + 40 ml/min of Air;
- Isothermal step at 500 °C for 60 min with the same flow of the previous dynamic one;
- Dynamic step until 900 °C at 10 K/min again with only Ar 80 ml/min protective flow;

- Dynamic step until ambient temperature at 50 K/min with Ar protective flow.

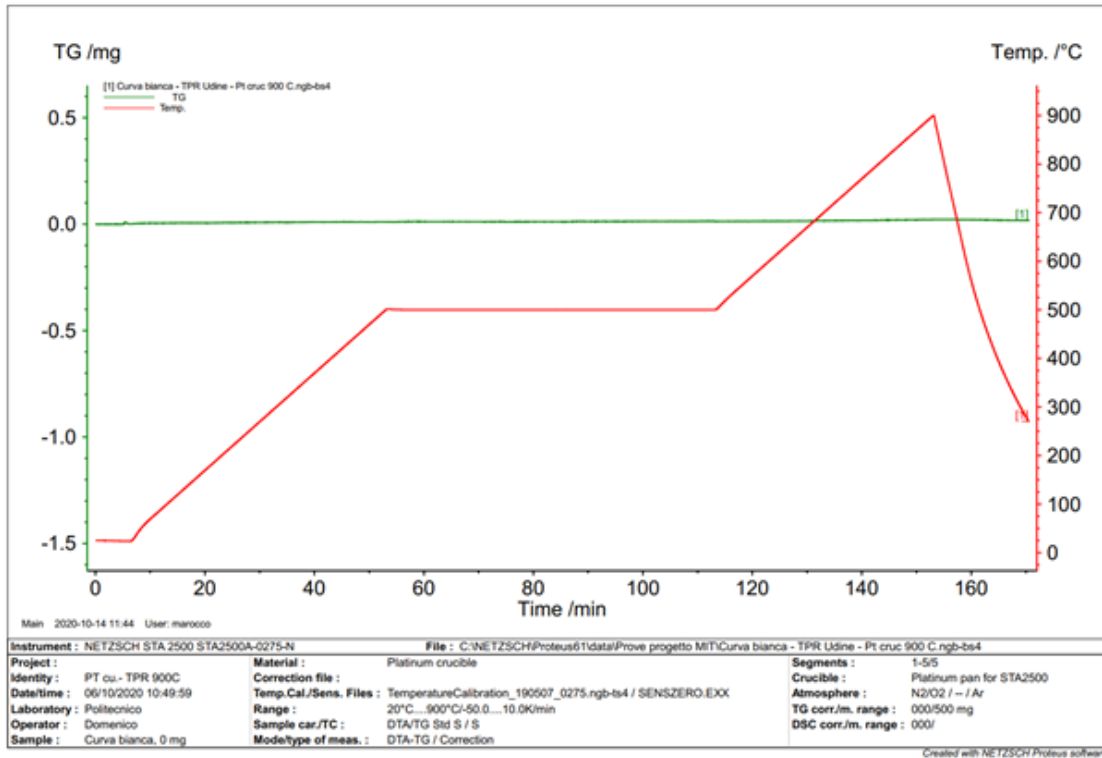


Figure 4.5: White curve of the platinum crucible in TGA until 900 °C.

In figure 4.5 is shown the white curve that has been measured to verify the stability of the Platinum crucible under the selected temperature range. In the picture, the green curve represents the crucible mass variation, which shows that the mass remains quite constant during the whole cycle even when the temperature peak reach 900°C. This is a good result that confirm how the setup can remain stable during the experiment, allowing to recognise each difference in the mass change without other phenomena having been triggered.

4.2.2 Test PRE1: Air pre-treatment of the first sample

For this experiment the following segments has been carried out:

- Start: 5 min at ambient temperature with 80 ml/min of protective Ar flow;

- Dynamic step until 500 °C at 10 K/min with 40 ml/min N₂/O₂ + 40 ml/min Ar;
- Isothermal step at 500 °C for 60 min with the same 40 ml/min N₂/O₂ + 40 ml/min Ar ;
- Dynamic step until 900 °C at 10 K/min with 80 ml/min Ar protective;
- Isothermal step at 900 °C for 10 min with 80 ml/min Ar flow;
- Dynamic step until ambient temperature with 80 ml/min Ar.

The second test has been made using the Platinum crucible adopted in the 1st test with a SFNM sample mass of 10,470 mg. In this experiment a simple air oxidation has been carried out in order to prepare the sample for the next experiment with 4 consequent loops. Figure 4.6 represents the pre-treatment of the SFNM with

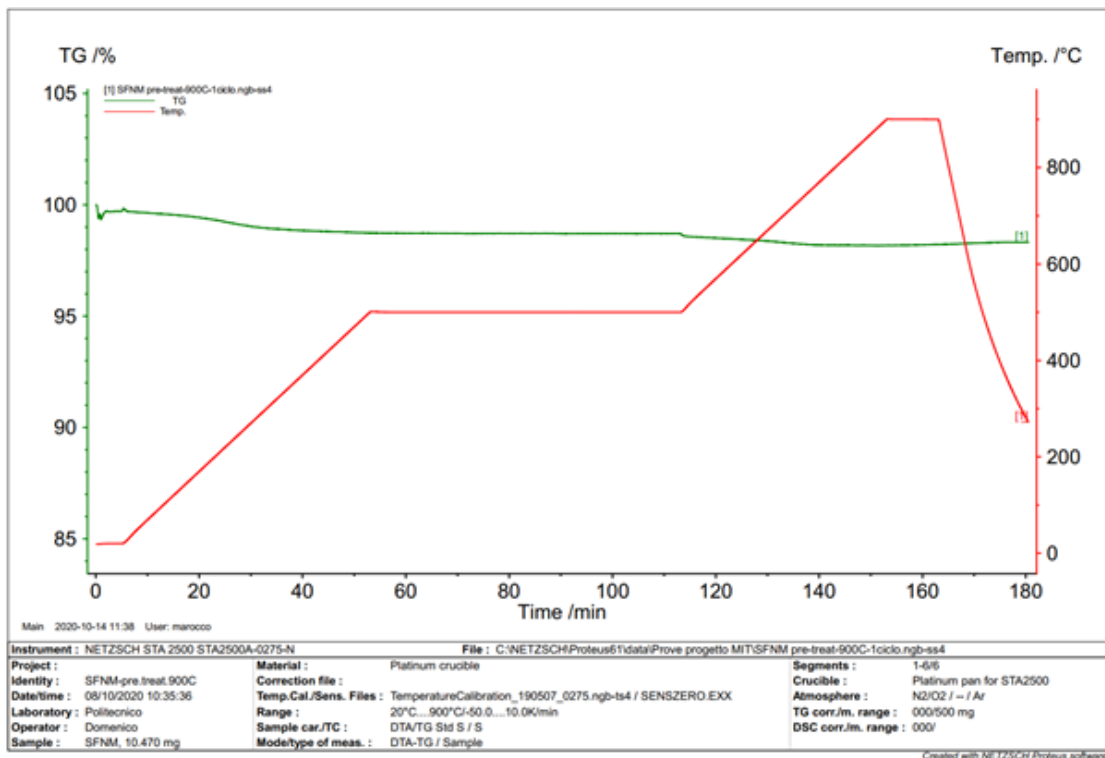


Figure 4.6: Air pretreatment of the first sample until 900 °C for the complete oxidation of the SFNM material.

air until 900 °C for the oxidation of the material. The mass is shown in the green curve in % with respect to the starting value of 10,470 mg. The material seems to be already oxidized before the test; the mass does not increase, instead decrease slightly at the first increase of the temperature due probably to water vapour and some volatile substances. A step of the mass is also shown after 110 min due to the changing of the flow from air flow: 40ml/min N_2/O_2 + Ar 40 ml/min to only Ar protective 80 ml/min. Another slight decrease of the mass arriving near 900 °C.

4.2.3 Test TPR1: single TPR of the pre-treated sample

After the white curve and the pre-treatment, a first TPR has been investigated by evaluating if the material presents some changes in the mass sending a reductive mixture of gas. A very low concentration of H_2 in Argon has been used as reductant gas. For this experiment the following segments has been carried out:

- Start: 5 min at ambient temperature with 80 ml/min of protective Ar flow;
- Dynamic step until 500 °C at 10 K/min with 40 ml/min N_2/O_2 + 40 ml/min Ar;
- Isothermal step at 500 °C for 60 min with the same 40 ml/min N_2/O_2 + 40 ml/min Ar ;
- Dynamic step until 900 °C at 10 K/min with 40 ml/min Ar protective + 40 ml/min $H_2(1\%)/N_2$;
- Dynamic step until ambient temperature with 80 ml/min Ar.

In Figure 4.7 is shown the first reduction performed with the SFNM sample. The material reacted as expected to the H_2/N_2 flow, is appreciable a reduction step during the temperature ramp from 500°C to 900°C. After reaching 900°C the H_2/N_2 reductive flow has been stopped and a cool down in Argon protective flow has been carried out. An isothermal step at 500°C for 60 min in air condition has been made before the reduction to make sure the sample would oxidize completely before the reduction step.

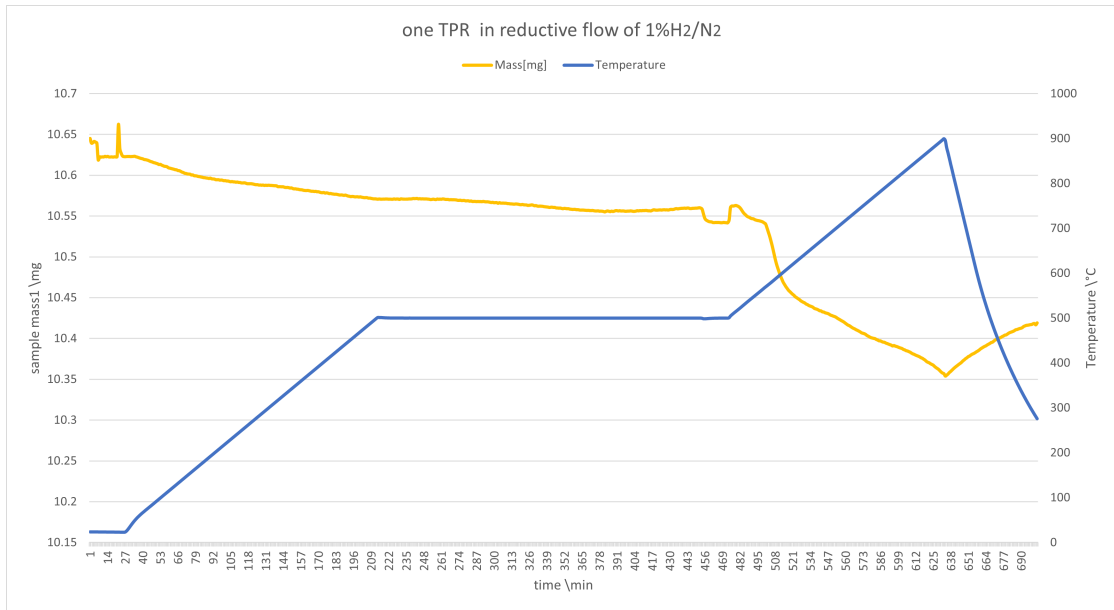


Figure 4.7: First TP-Reduction experiment in $H_2 1\%/N_2$ in temperature ramp from 500°C to 900°C.

4.2.4 Test TRP4-air: 4 consecutive cycles with re-oxidation in air

The next step has been done by subjecting the perovskite material to a first real chemical looping redox test. A recap list of the steps performed in this experiment:

- Dynamic temperature ramp until 500°C moving on 10 K/min with air 40 ml/min + 40 ml/min Ar;
- Isothermal at 500°C for 60 min with the same flow composition as before;
- Isothermal at 500°C with 80 ml/min only Ar protective flow to purge all the remaining air;
- Dynamic temperature increase until 900 °C at 10 K/min with $H_2(1\%)/N_2$ 40 ml/min + Ar 40 ml/min;
- Isothermal at 900°C 10 min to purge H_2/N_2 with 80 ml/min of Ar protective;
- Dynamic cool down until ambient temperature at 50 K/min;

- Restart from the 1st point and repeating all the steps for 4 time.

In order to assess the first reproducibility in redox environment a 4 loops experiment has been carried out by swinging the temperature from 500 to 900 °C respectively for the oxidation and reduction section. The oxidation part has been performed for the 4 times in air environment, while the same H_2/N_2 flow has been adopted for the reductive part. Looking at Figure 4.8 the material seems to present constant performance in all the cycles: starting in a condition where it was already completely oxidized, the first temperature ramp from 500°C to 900°C show a quality mass reduction compared to the starting mass of the sample. By removing the reduction flow and performing a dynamic temperature reduction with the protective flow is possible to notice that the mass start anew to increase creating a cusp, nevertheless the curve seems to stabilize before the air flow starts. When the air flowing in the TGA the material starts to re-oxidize as expected, also the transition time seem to stop even before the isothermal step at 500°C. The following 4.9 show the hydrogen reacted in any single cycle as function of the temperature of the TGA test. The various trends refer to calculations deriving from post-test elaborations taking as reference the derivative data of the mass variation measured by the instrument. In this dataset, between 550 and 600 °C there is a steep increment in the hydrogen reacted and after 600°C no other relevant peaks are present. For the whole experiment, every hydrogen peak is delimited between the temperature range from 550°C to 600°C; also from the 2nd to the last cycle the hydrogen utilization show a bit increase: this is much appreciable in the last figure of this set 4.10 where all the 4 cycles are plotted overlapping. With these results is possible to make a first hypothesis on the material which is activated by the hydrogen that is able to remove oxygen and consequently create vacancies in the bulk of the lattice. Secondly, the oxygen contained in in the air can easily reconstruct the initial structure by reincorporating the oxygen into the vacancies. Figure 4.11 shows four points that represent the maximum loss of oxygen in reductive phase expressed per unit mass of sample. These data were calculated always starting from the raw data of derivative of the mass calculated instant by instant. The maximum peak of oxygen loss (vacation creation) is generated starting from the second cycle. The value stabilizes around 1.7 mg/s of O_2 lost per gram of perovskite. At the fourth and last cycle performed in this experiment, the value is slightly lower. This

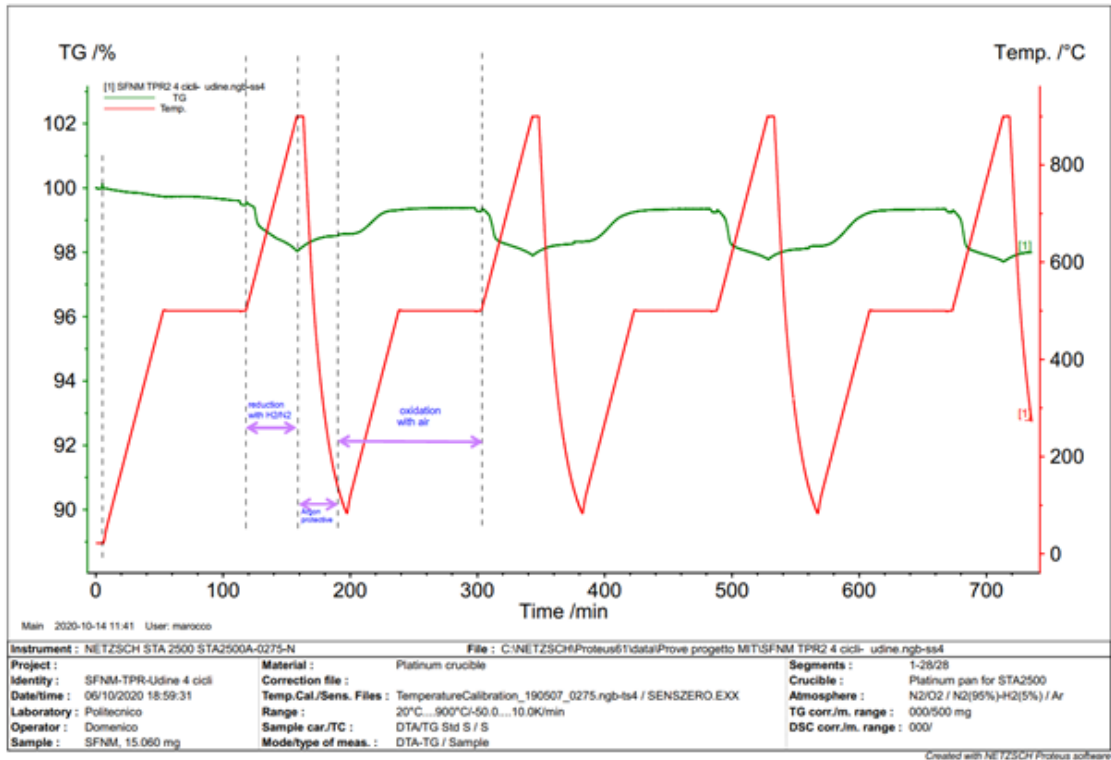


Figure 4.8: 4 consecutive cycles of TPR and subsequent re-oxidation in air environment. During the first loop are highlighted the reduction and oxidation steps separated by argon flow during the temperature swing.

indicates that a stabilization of the material has yet to occur.

4.2.5 Test TPR4-50%CO₂: 4 consecutive cycles with re-oxidation in CO₂ at 50%vol

In order to see if the CO₂ environment could create the same effect on the material, the next test has been carried out with 50% of CO₂ in argon flow. The steps performed are shown below:

- Dynamic temperature ramp until 900°C moving on 10 K/min with H₂(1%)/N₂ 40 ml/min + 40 ml/min of Ar,
- Isothermal at 900°C for 10 min with the same flow composition as before;
- Cool down step until ambient temp in argon protective;

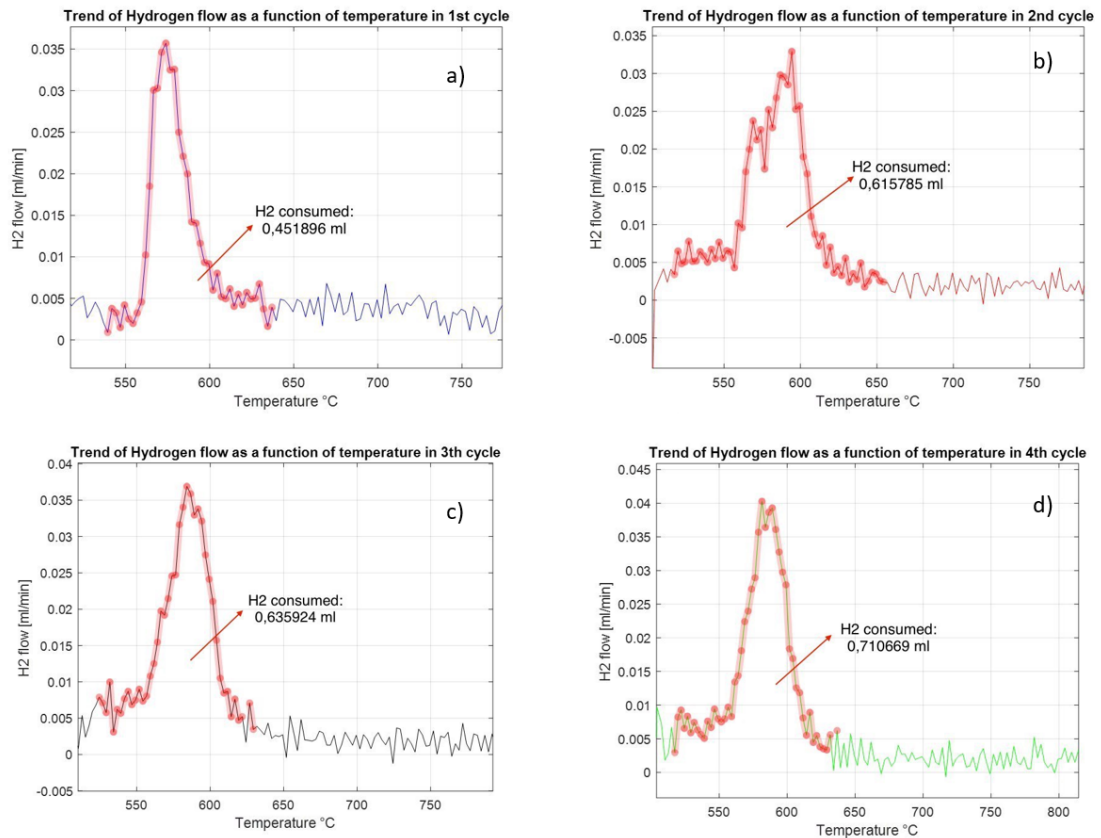


Figure 4.9: hydrogen reacted as function of temperature during the TPR in: a) 1st cycle; b) 2nd cycle; c) 3rd cycle; d) 4th cycle.

- Dynamic increase at 10 K/min with 40 ml/min CO_2 + 40 ml/min Ar (50% CO_2 flow) until 500°C;
- Isothermal at 500°C with 40 ml/min Ar + 40 ml/min CO_2 flow for 60 min;
- Isothermal 500°C only Argon 80 ml/min for 5 min;
- Dynamic temperature increases until 900°C at 10 K/min with $H_2(1\%)/N_2$ 40 ml/min + Ar 40 ml/min;
- Isothermal at 900°C 10 min to purge H_2/N_2 with 80 ml/min of Ar protective;
- Dynamic cool down until ambient temperature at 50 K/min in Argon protective;

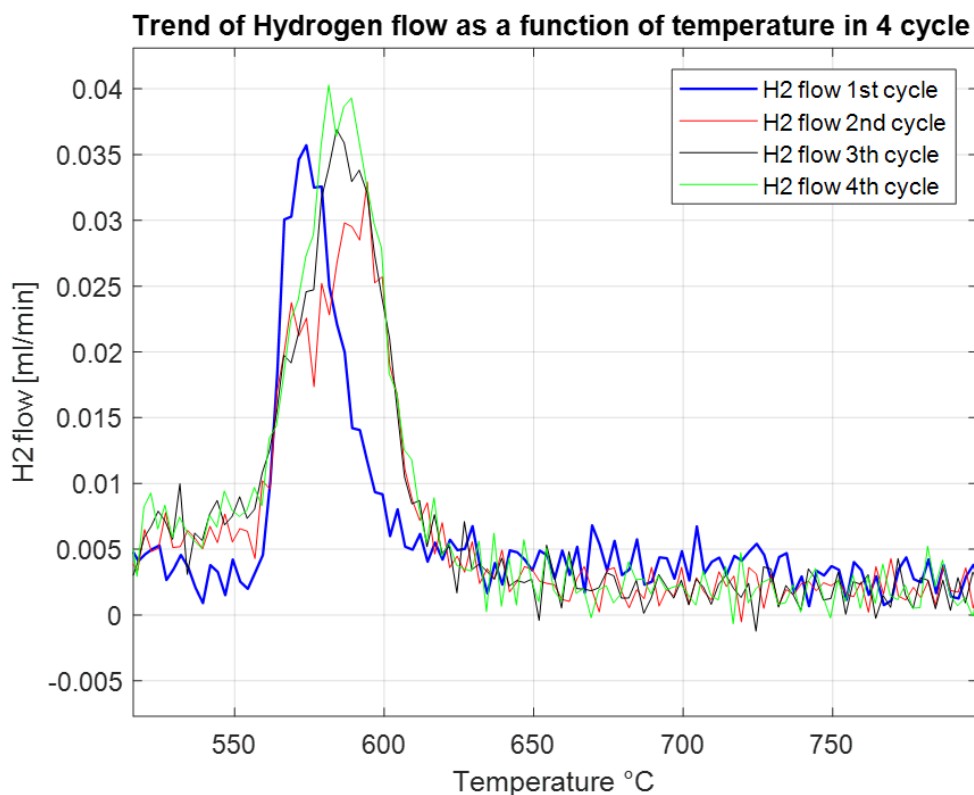


Figure 4.10: Overlapping of the hydrogen reacted in all the 4 cycles performed in TPR.

- Restart from the 4th point and repeating all the steps for 4 time.

The Figure 4.12 shows the mass variation of the SFNM sample. Are also reported the delta changes of mass during both reduction and oxidation phenomena; in the oxidation situations the delta increase slightly, on the other hand is possible to see a bit decrease of the delta mass from the beginning to the end of each single reduction step. In the table 4.2 have been grouped all the delta of mass calculated before and is also reported the starting sample mass. Furthermore, a similar trend in temperature and flows has been adopted for this experiment, only changing the oxidation gas from air to $CO_2@50\%$. Figure 4.13 and Figure 4.14 represent the hydrogen reacted in the 4 cycles of the test with CO_2 at 50% oxidation flow. In

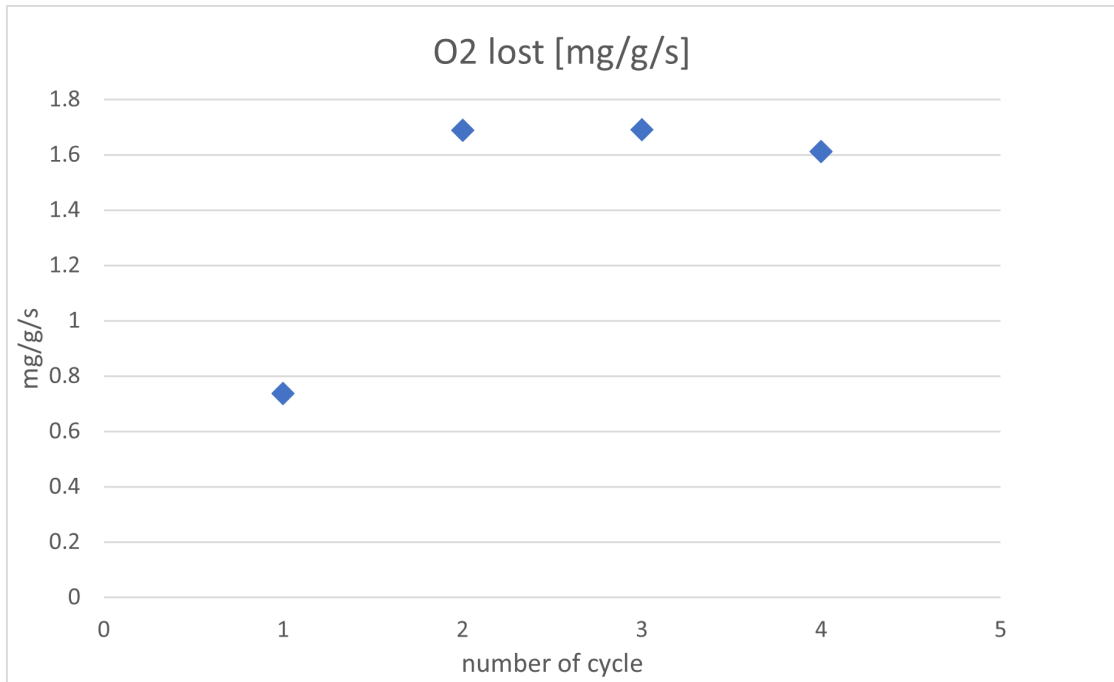


Figure 4.11: Maximum oxygen released for each cycle. Calculated considering the best rate of hydrogen consumed.

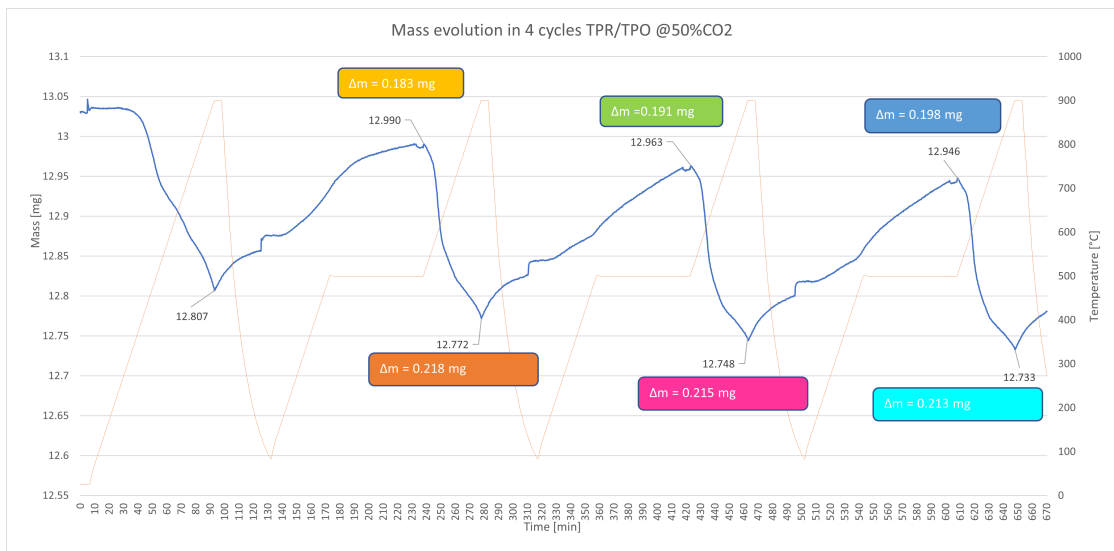


Figure 4.12: Mass variation of SFNM sample during the 4 cycles with reoxidation at 50%CO₂ vol.

Sample mass [mg]		13.031
$\Delta mass [mg]$		
Reduction	Oxidation	
/	0.229	
0.183	0.219	
0.191	0.215	
0.198	0.213	

Table 4.2: Mass variation of SFNM from figure 4.12 summarized.

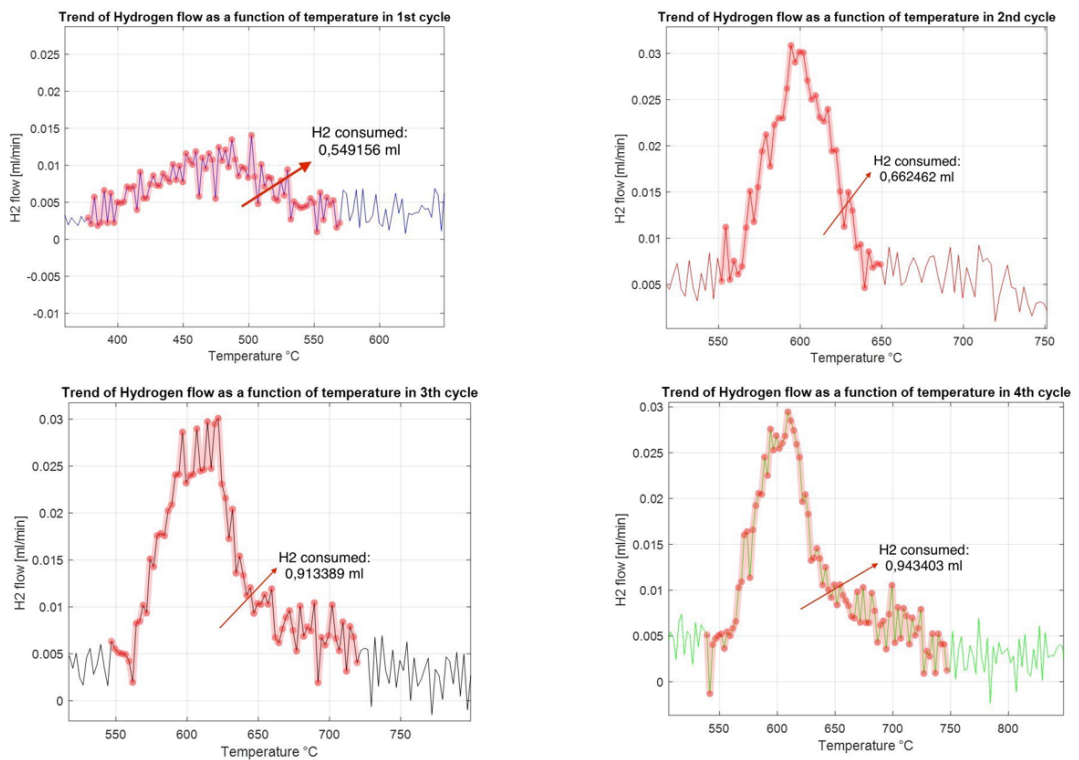


Figure 4.13: Hydrogen reacted for each cycle performed during the 4-loop test with CO_2 at 50%vol in oxidation step.

cycle number 2, 3 and 4 the hydrogen reacted increase slightly among the cycles. The Last cycle has the highest amount of hydrogen reacted; this suggest a farther increase if more cycles had been performed. Also, the total volume reacted is higher in this test with CO_2 oxidation than the volume reacted with oxidation in

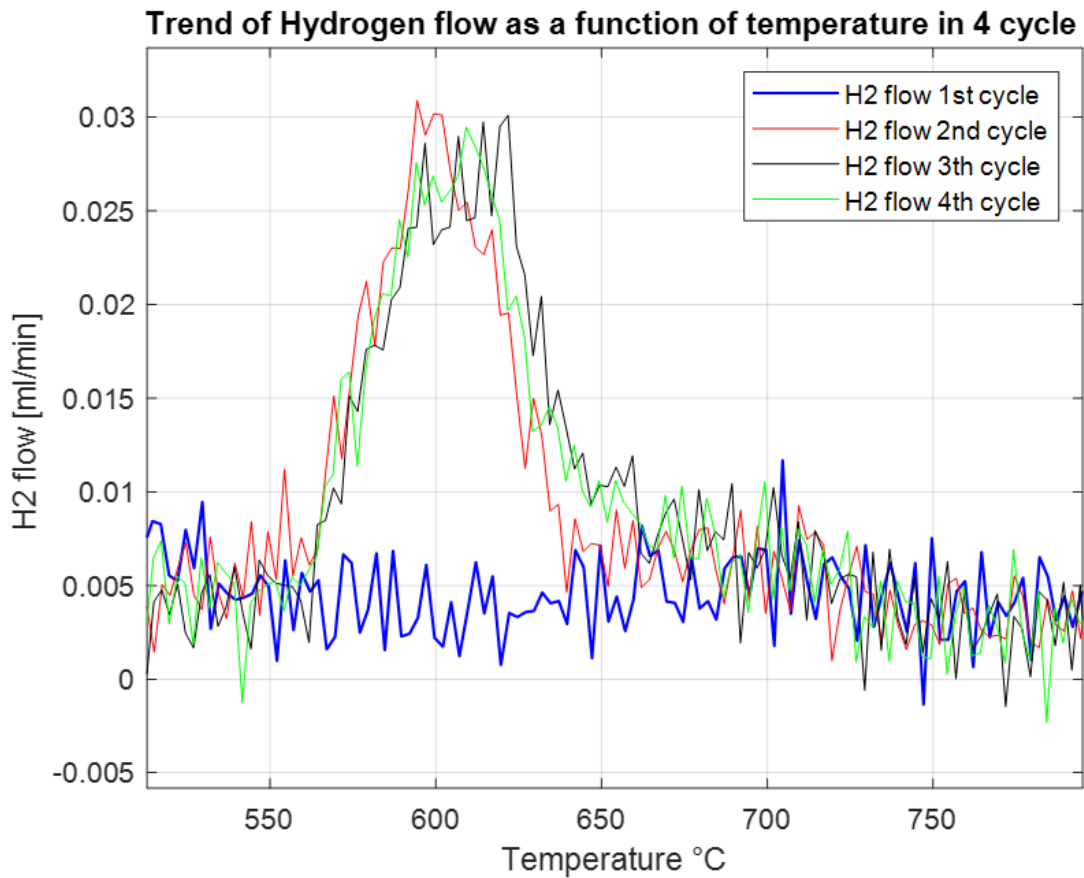


Figure 4.14: Trend of hydrogen reacted in the 4-loop cycles test with 50%vol CO_2 overlapped. No such increment in reaction is shown between the 2nd and 4th cycle.

air. Different situation can be described for the first cycle, where the reduction with H_2 happens between 400 and 550 °C. In this case the reaction starts before the other 3 because during first reduction the $H_2(1\%)$ has been sent right from 25°C up to 900°C in a single dynamic increase of 10 K/min. Also in this case the reduction and oxidation seem present a replicability. But a huge different with respect to air oxidation is shown in the 500°C isotherm step. The kinetic of oxidation is different in the two cases. The figure 4.15 is an overlapping of the two experiments. Apart from the time shift, is evident how the mass increase in the CO_2 oxidation is higher than in the air. The CO_2 oxidation did not arrive

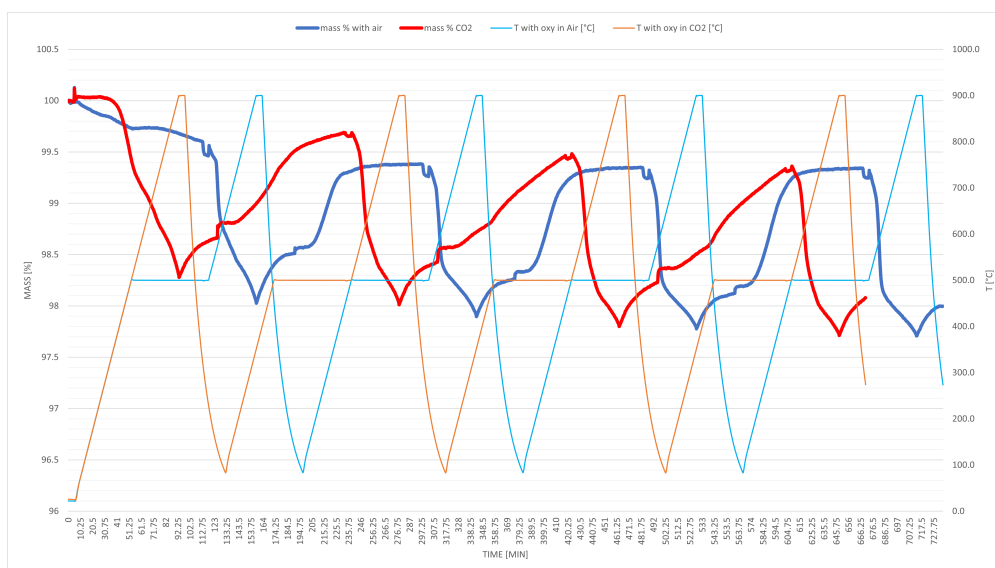


Figure 4.15: Comparison of the 4th and 5th TGA test by overlay the mass-change curves. The CO_2 oxidation curve is shifted with respect to the air oxidation ones because of the different behaviour performed. red sample mass was already pre-treated before the TG experiment, while the blue sample mass has seen firstly a pre-treatment in air at $500^\circ C$.

at the same plateau as the air oxidation does, this is sign that different reaction occurs during the CO_2 environment with respect to the air ones. The shape of the red curve is less tilted and at the end of the time step of the oxidation the plateau is never reached for all the re-oxidation segments. Subsequent investigation on these behavior with other analysis will reveal what could be happened in the CO_2 section. However, the reduction of the material is possible in both cases, and repeatable in each cycle. With the hypothesis that the reverse Boudouard reaction is performed and carbon deposition is not happening at least at the initial part of the oxidation, then figure 4.16 show the result of the DTG calculated in at the beginning of the oxidation. This corresponds to a certain CO production calculated from the same DTG analysis. The first peak in almost the double with respect to the second and third ones. A clear signal that the fresh material has different performance compared to the subsequent steps where the CO_2 has already reacted with the material at least once. The stability of the 3rd cycle demonstrate that the material reach a certain stability in CO_2 environment with curve very similar to

the one of the second cycle. Also the kinetic is different from the 1st cycle: the time needed for the peak during first oxidation is about 30 seconds, while from the second oxidation on, the time is almost doubled. From this could be said that CO_2 in some way interact with the material and not only creating CO by loosing an oxygen ions inside the lattice of the perovskite, instead something different could be possible, with some deposition from the carbon containing species on the surface of the material, that as consequence change the reactivity of the splitting reaction. These experiments has set the foundation for further analysis. More cycle

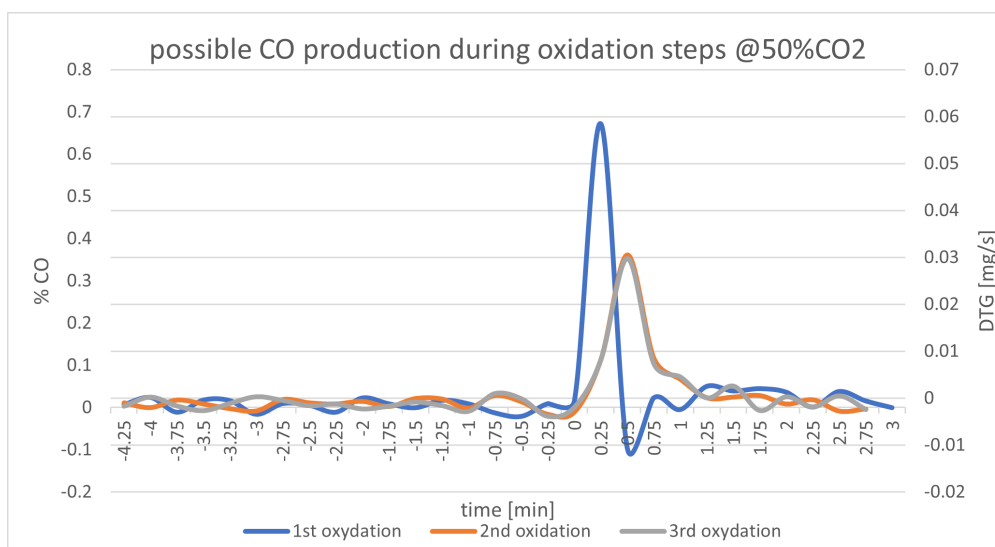


Figure 4.16: Peak of possible CO production taking as hypothesis that the change of mass is indeed oxygen lattice acquisition by CO_2 splitting.

with different CO_2 concentration has been assessed, to evaluate the stability of the material with different conditions.

4.2.6 Test TPR10: 10 consecutive cycles after pre-treatment of a new sample

After the 4 cycle with CO_2 oxidation the next test we decided to perform was a 10-cycles test to see the response of the material on a longer time scale operation. Before doing that the SFNM sample was pre-treated to ensure that the 10-loop test start would be in oxidation state already performed with CO_2 as oxidant. The

different segments of this experiment have been:

- Start in ambient temperature with only Ar 80ml/min;
- Dynamic step at 10 K/min until 900°C with $H_2(1\%)/N_2$ flow 40 ml/min + Ar 40 ml/min;
- Isothermal step at 900°C for 30 min maintaining the same gas flow;
- Another 5 minutes at 900°C but changing flow with only Ar protective 80 ml/min;
- Cool down at 10 K/min with $CO_2@20\%$ until ambient temperature.

Figure 4.17 shows the mass changes in % of the SFNM sample during the pre-treatment phase, together with the temperature. This time a constant increase of temperature from ambient to 900°C with steps of 10 K/min was selected and a consecutive 30 min of isothermal step at 900°C. It is clear that some event in a

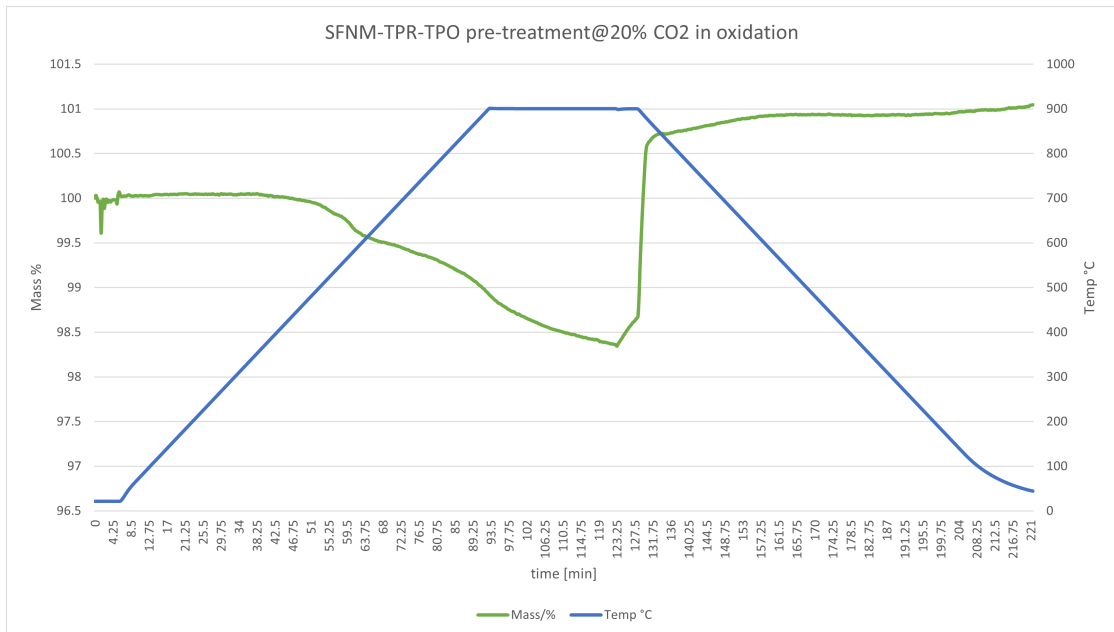


Figure 4.17: Pre-treatment of the sample mass before the 10 cycles test. The sample gain 1% in mass after the TPO in CO_2 environment.

decreasing ramp of temperature the CO_2 influence the material, as is possible to

notice from the slight increase of the sample mass. This has been the first hint for a possible carbon deposition phenomenon. After this treatment, the 10 cycles test has been performed. Is possible to refer the following list for the different segment performed in the 10-loop test:

- Start from ambient temperature to 900°C at 10 K/min in $H_2(1\%)/N_2$ 40 ml/min + Ar 40 ml/min;
- Isothermal state for 30 min at 900°C still in H_2/N_2 flow + protective;
- 5 min isothermal 900°C changing flow to only argon protective 80 ml/min;
- Cool down until 500°C at 10 K/min with argon protective 80 ml/min;
- Remaining at 500°C for 5 min with only Argon 80 ml/min;
- Isothermal step at 500°C for 90 min with 20% CO_2 oxidant gas flow;
- 5 min still 500°C replacing CO_2 with only Argon flow;
- From here restart from the first point but with an initial temperature of the dynamic ramp of 500°C instead of 25°C. Repeat the entire process 10 times.

In Figure 4.18 are shown the cycles for the 10-loop test. Moving forward with the cycles the mass tend to decrease after every reduction and oxidation with respect to the previous condition; also, viewing at the end of each reduction step is possible to notice that the curve tend to stabilize as the subsequent cycles proceed, for this reason the reduction steps seem to be performed quite totally arriving at the end of every cycle with a sample mass completely reduced. Conversely, the end of the oxidation is not evident: possible causes can be that the time needed for the complete oxidation is longer than that performed into the cycles or that in the sample starts a carbon deposition phenomenon which leads to a continuous increase in the sample mass never reaching the expected plateau. The Table 4.3 reports the delta of mass (%) calculated for each section of reduction and oxidation. The delta referred to the reduction steps slowly decreases moving forward through the steps, while is not possible to assert the same in the case of oxidation steps, with the last 2 delta of mass that are bigger than the previous ones. Moreover, the number have the same order of magnitude, and let assuming that the reduction

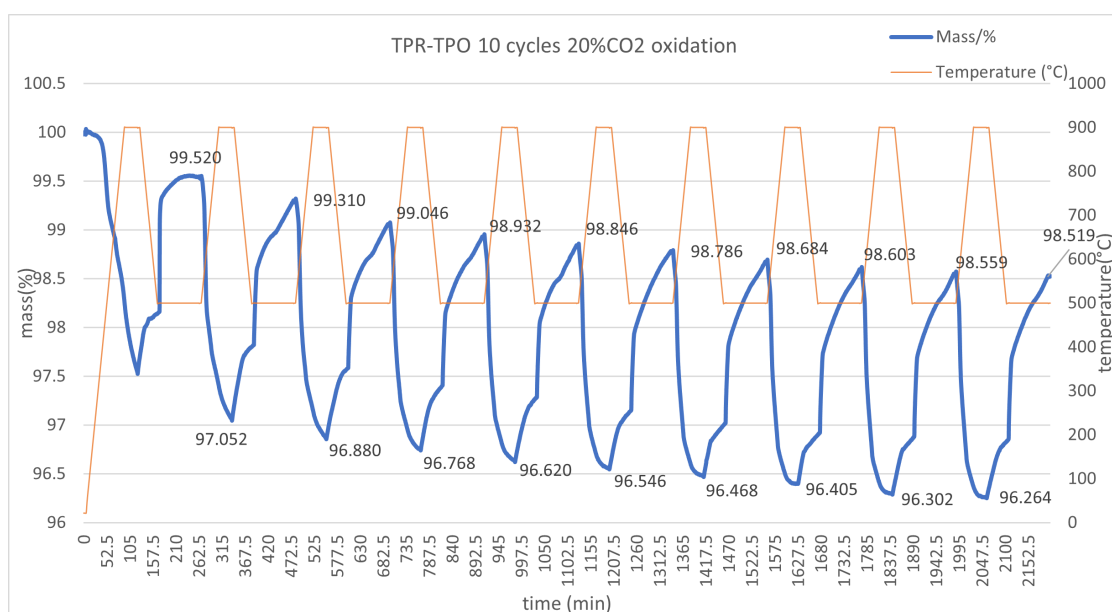


Figure 4.18: Mass variation during the 10 cycles test performed in TGA. The number refers to the % of mass evaluated in each end of reduction and oxidation, with respect to the initial sample mass.

and oxidation occur with the same quantity of material. Nevertheless, this says nothing about where the material enters in contact with the gas flow. In fact, with this preliminary data-set is not possible to assert if the reactions take place both on the surface and in the bulk of the SFNM-04 or, conversely, if only the first layer of sample is subjected to these variation leaving intact the deeper tier.

The raw data taken from the derivative of the mass change can be manipulated in order to calculate the total hydrogen reacted in each cycle. Figure 4.19 show the ml of H_2 that have been participated to the reaction in each reduction step. From the data is not possible to evidence an increase or decrease trend. The numbers in fact oscillate between a minimum of 1,264 ml and 1,512 ml, neglecting the first reduction that is strongly less with respect to other hydrogen consumption, probably due to a need for stabilization by the material from the reductive point of view. The good feature that is possible to notice, is that until the last reduction there are no obvious signs of loss of reductivity. The material does not hint at losing its ability to reduce in the presence of hydrogen allowing a good reproducibility of the cycles. The raw data taken from the derivative of the mass change can be

segment number	Sample mass [mg] Δm reduction [mg]	16.864 Δm oxidation [mg]
1	/	/
2	0,416	0,381
3	0,409	0,365
4	0,384	0,365
5	0,389	0,375
6	0,388	0,378
7	0,391	0,374
8	0,384	0,371
9	0,388	0,381
10	0,387	0,380

Table 4.3: Resume of the values of mass change during the reduction and oxidation steps of the 10-loop test. The first reduction and oxidation has not been considered.

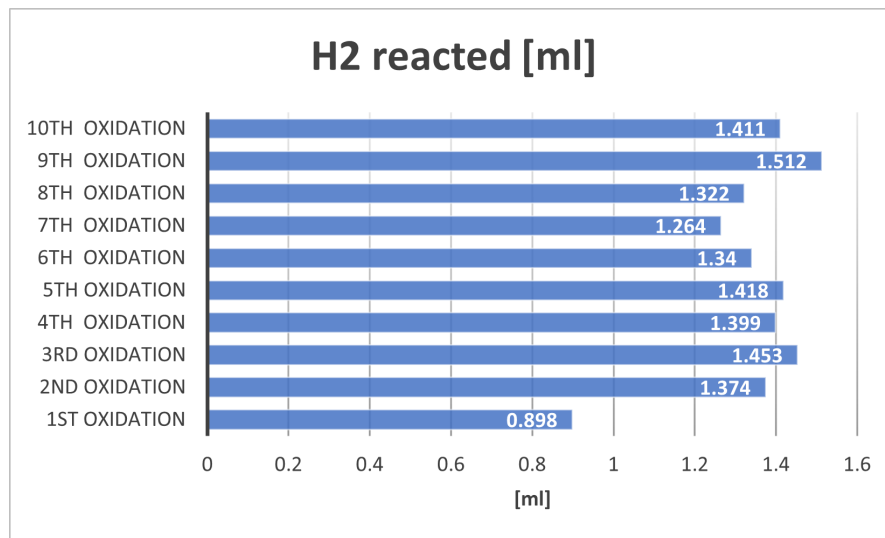


Figure 4.19: Total hydrogen reacted in [ml] for each reduction segment of the 10 cycles test.

manipulated in order to calculate the total hydrogen reacted in each cycle. Figure 4.20 and figure 4.21 are the graphs of the hydrogen reacted in in all the cycle. Each cycle is displayed individually with a double vertical axis graph to show the possible oxygen lost (raw derivative data) and the resulting hydrogen consumption (calculated from derivative data). Figure 4.20 shows the overlapping hydrogen

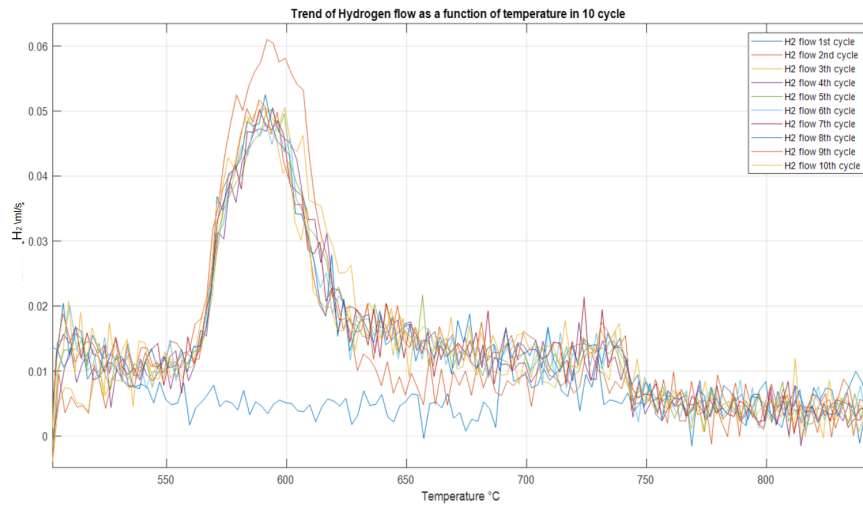


Figure 4.20: H_2 reacted in all the 10 cycles. Curves are superposed to evidence the difference between the reduction segments.

consumption peaks. Since they were derived from the raw mass derivative data, the results show up to be very fluctuating. The similarity of the peaks is thus once again highlighted. In this picture the value of the hydrogen flux consumed in the first cycle is not displayed because it is included in a lower temperature range than all the others. It is also visible the difference between the second peak, with greater intensity and all subsequent cycles that follow a trend almost identical. For this experiment the first cycle starts in different condition with respect to the other ones, in fact the first dynamic temperature increase start from 25°C to 900°C already with $H_2(1\%)/N_2$ flow; for this reason the first reduction is performed in a temperature range that is different and lower with respect to the other cycles: is also possible to notice the different kinetics of the reaction from the different behavior of the curve.

Presentation and discussion of the results

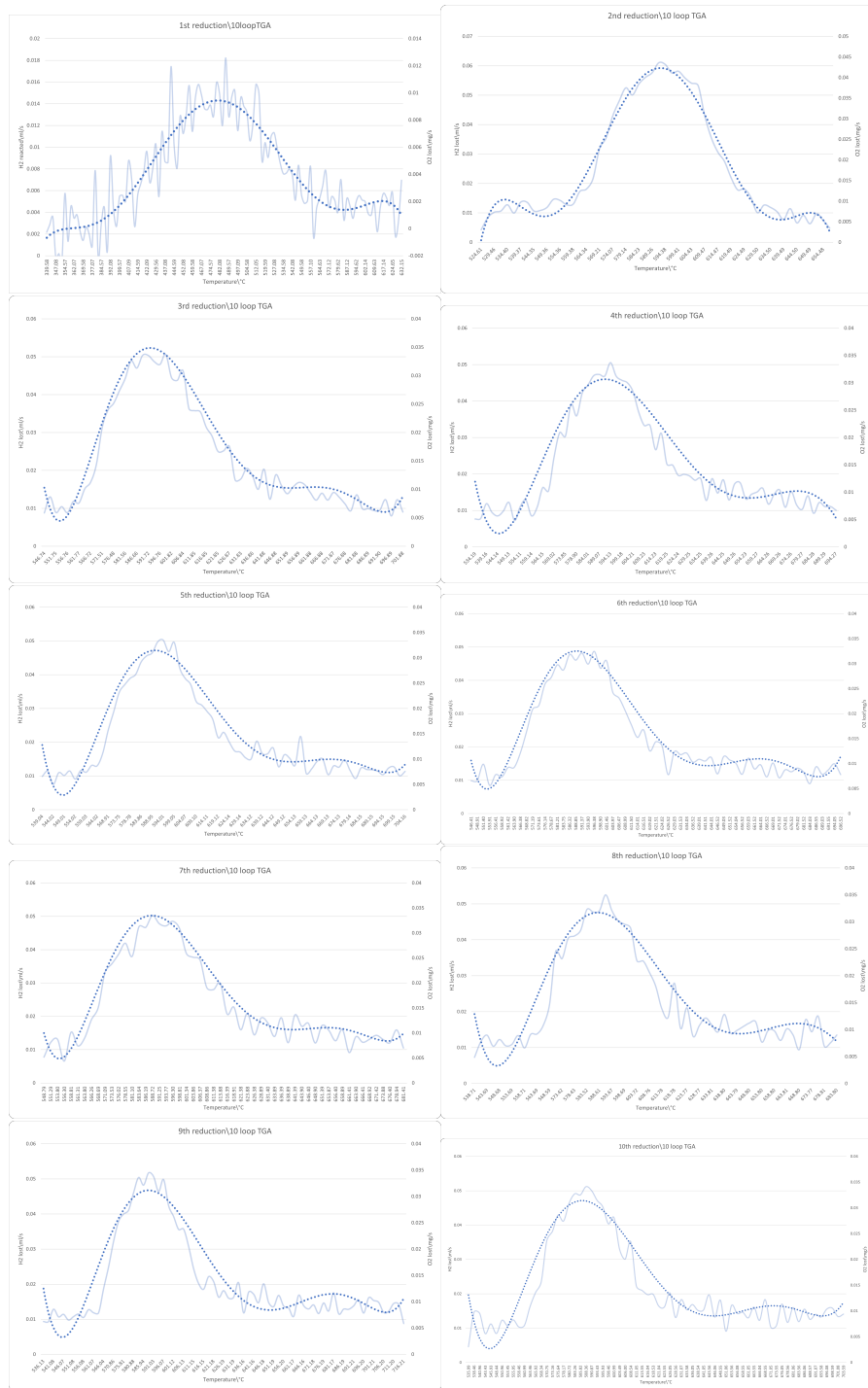


Figure 4.21: Hydrogen reacted in each reduction step of the 10-loop cycle test with 20% CO_2 in oxidizing environment.

The first curve presents a maximum peak of hydrogen consumption that is lower compared to all the further cycle, where conversely the consumption seems to reach a stabilization of its trend. Moreover, the first cycles tend to have a more symmetrical curve, while continuing after the third cycle the curve stabilizes with a ramp of consumption up to the maximum peak and then a slower descent characterized in the final part by a consumption that tends to the initial zero value. It can be seen how the consumption trend in the various cycles stabilizes towards values of maximum peaks with same values. This is better described through figure

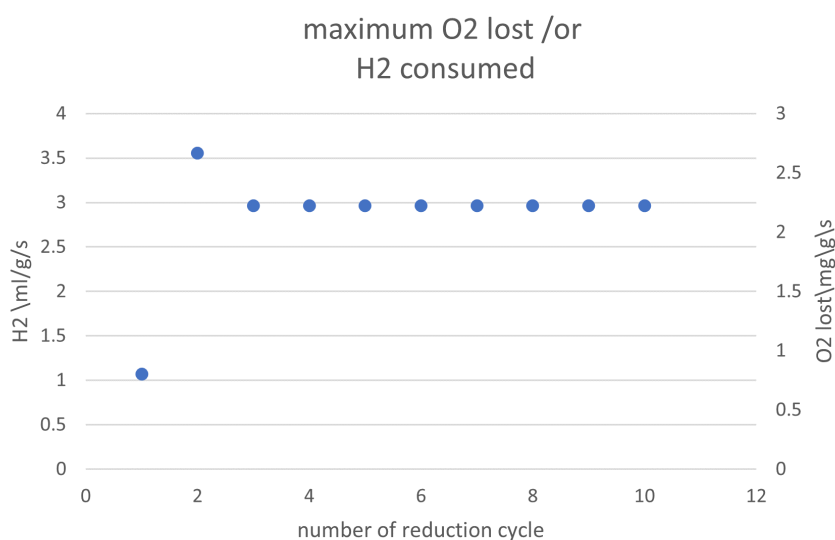


Figure 4.22: Estimation of the maximum rate of oxygen lost for each gram of perovskite material. On the left y-axis there is the corresponding maximum rate of hydrogen consumed, again per unit mass of the sample. Data refers to the sixth TGA test with 10 cycles.

4.22 where for each cycle, the maximum delta of mass has been chosen and reported as a point in the graph. The left axis represents the hydrogen consumed, calculated starting on the raw data of the derivative that is a real measure taken in the output from the TGA data. In particular, the derivative shows the decrease or the increase of the sample mass in each time step. Assuming that the hydrogen sent in the line is able to reduce the material and take away some oxygen by performing the

reaction 4.1:



In this way we can consider that the derivative data corresponds to the oxygen lost in the time unit. Since the derivative is expressed in [mg/s] we can calculate the $\mu\text{mol}/s$ of oxygen lost dividing by the molar weight of O_2 . Then, by multiplying by two the number is possible to retrieve the $\mu\text{mol}/s$ of H_2 since for each mol of oxygen we will have two moles of hydrogen. In order to obtain a flow rate of hydrogen as represented in the graphs, is necessary to further multiply the number for $22.4 \text{ ml}/\mu\text{mol}$ and after that is possible to obtain the ml/s of hydrogen consumed. The peak of each consumption has been considered as the best SFNM reduction rate, and the figure 4.22 report this trend. The hydrogen consumption stabilizes after the second cycle to a value of 3 ml/s consumed for each gram of SFNM. This value is stable until the end of the test, showing again the great reproducibility of the reduction set on the sample. As estimated in the fifth TGA test, again the

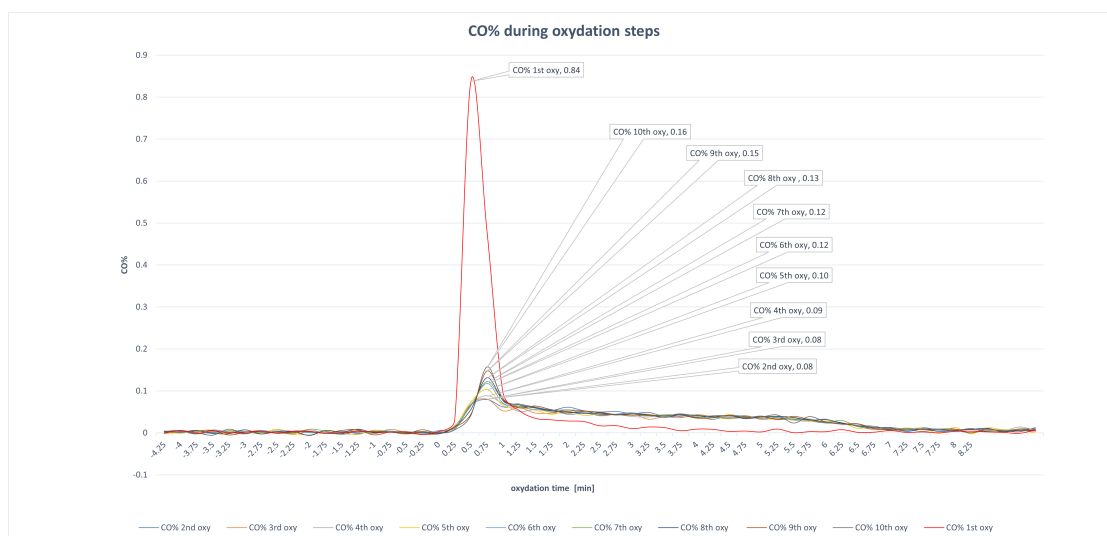


Figure 4.23: Estimation of peak CO production in each oxidation of the 10-cycle redox cycles. Calculation determined by the assumption that all of the initially acyused mass is driven by an accumulation of oxygen in the lattice.

possible peak of carbon monoxide production has been estimated. The hypothesis remains the same as in the previous test. That is, all the mass initially acquired by the sample during the first moments of oxidation is assumed to be all due to a

re-acquisition of oxygen in the lattice. The filling of oxygen vacancies is therefore assumed to take place thanks to the split of CO_2 and the consequent production of the CO peak. The trend seems to follow well the results previously obtained during the fifth test. The first oxidation results in a much larger derivative, i.e. an increase in the mass of the sample more quickly. The maximum peak is reached with a production of 0.8%. Next, as with other previously determined results, production drops dramatically to 0.08. Also, for this trend, the material sees its stabilization. The estimated production of CO rise again from the second cycle onward. Kinetics, however, is noticeable very slow compared to the first cycle with a long production time that ends after about 7 minutes, unlike the first that after less than 2 minutes already seems to be practically at the end. Figure 4.23 shows the phenomenon just described.

4.2.7 Test TPR6-oxy: 6 cycle with a final longer oxidation

Since from the 10-loop test the oxidation reaction curve seems not to reach a plateau. Another test with 6 cycles and 1 longer final oxidation has been carried out to see in which point the mass plateau would have been reached. The shape of the curves is typical for that material and for the gases used. A minimum fluctuation given by the switch with argon is always visible but at the same time well distinguished with respect to the other gas flows, thus making it possible to determine at which points the re-oxidation starts to occur which always occurs after a stage of pure argon for the cleaning of the lines from the previous step. From figure 4.24 is possible to notice that the mass in the last oxidation increase. In particular, it reach 17.7506 mg at the end of the oxidation, with an increment with respect to the initial mass that was 17.519 mg. This suggest that a strong carbon deposition phenomenon appear during the oxidation step and could explain the fact that also in the other previous cycles the oxidation did not reach a stable plateau of the curve. In table 4.4 are calculated all the delta of mass performed in both reduction and oxidation steps during the 6 cycle and is also calculated the additional mass acquired thanks to carbon deposition. The cycles follow the typical trend for the material well, again reproducing the curves seen for the 10-cycle test. Quantitatively, the reproducibility from the previous test was also maintained with similar deltas of mass lost and acquired. Also, in this case the oxidation never

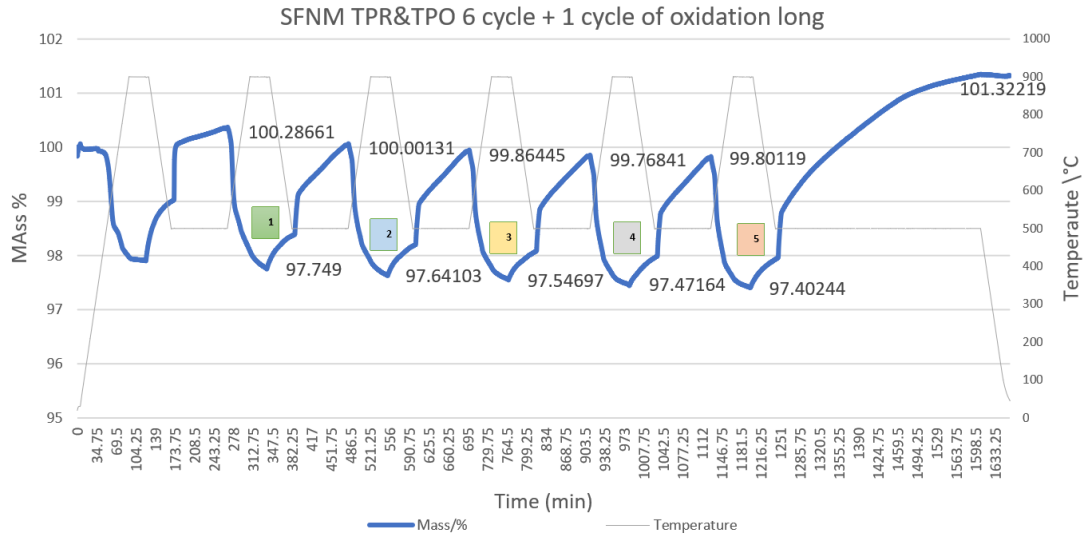


Figure 4.24: Mass % as function of time in the 6 cycles test with longer final oxidation (Seventh TGA experiment). The curve increase finally with the longer exposure of the sample in the oxidising environment. The number are captured at the end of each segment both reduction and oxidation ones.

segment number	Sample mass [mg]	17.519
	Δm reduction [mg]	Δm oxidation [mg]
1	0.444	0.395
2	0.413	0.389
3	0.406	0.389
4	0.402	0.408
5	0.420	0.687

Table 4.4: Delta of mass in [mg] of reduction and oxidation steps. Is included the final longer oxidation in segment 5 with a noticeable higher number.

reaches a flattening of the curve. Therefore, a long final oxidation is maintained where a plateau is finally reached with a maximum mass limit of 101,32%. This test proved the evident deposition of carbon on the surface of the sample when exposed in an oxidizing atmosphere with CO_2 .

4.2.8 Test TPR6-oxy/red: 6 cycle with a final longer oxidation and subsequent reduction

To verify the reversibility of the last condition in the log oxidation test, another experiment with the same conditions of the previous one has been performed, adding as final segment an increment of temperature again from 500°C to 900°C in $H_2(1\%)/N_2$ 40 ml/min + Ar 40 ml/min and then leaving the reduction flow-rate for more than 6 hours. Figure 4.25 shows clearly that as in the previous test, the

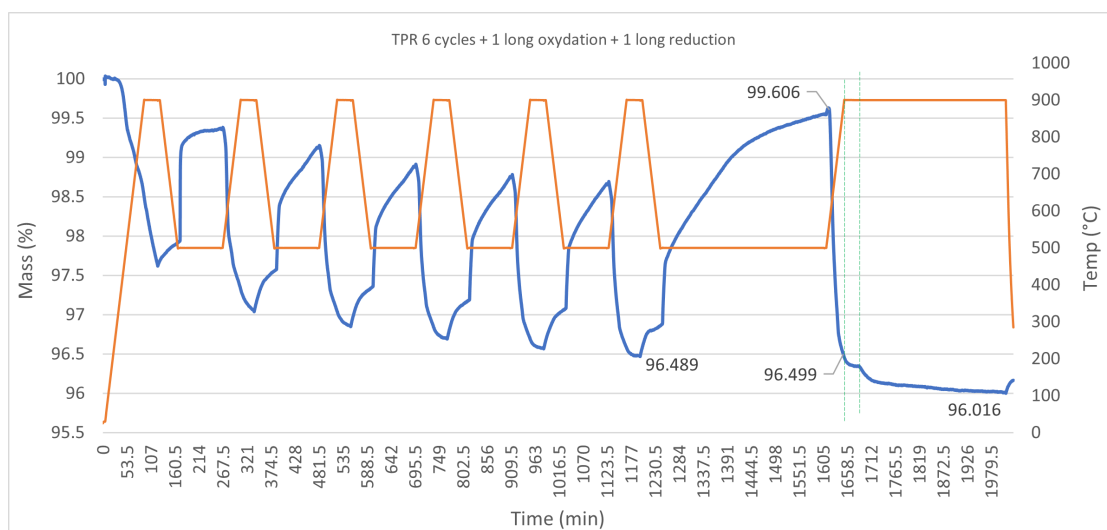


Figure 4.25: 6 cycles of TPR and TPO followed by a long oxidation always with $CO_2@20\%$ at 500°C and a last reduction in $H_2(1\%)/N_2$ flow in temperature ramp until 900°C. Picture refers to the Eighth TGA experiment.

sample mass keep increasing during the oxidation segment at 500°C and once the gas flow has been changed from oxidant to the reductive one, the reduction starts with also a faster kinetics bringing back the mass to its complete reduced state, then the reduction segment keep going on for 6 hours at 900°C showing that the decrease of mass still continue during this time, but with very few slope of the curve. A note can be made about the final reduction curve which is divided into two different segments. At first the reduction seems to reach a stable value settling, with respect to the initial mass, at 96,5%. Then another short increase of the reduction activity creates a second downward ramp of the sample mass to then return to lower derivative values of the mass curve. The material at the end of

the last reduction sees a decrease in mass of about 4% with respect to the initial value. This characterization of the final curve could be due to a true difference in activity from previous tests. The higher ramp is definitely due to the surface activity between hydrogen and material. Once the reaction is completed at the outer boundaries, it is likely that nickel will move from the bulk B-sites to the boundary zones allowing the release of oxygen ions from the matrix. It is possible that the phenomenon consists of a reduction performed in two different stages, the first superficial involving the deposition of carbon created previously, the second into the bulk involving nickel and iron that will create a new alloy on the surface. In Table 4.5 is shown that the total delta of mass after the 6 hours of reduction

Sample mass		15.340 mg
Δm reduction [mg]	Δm oxidation [mg]	
0.477	0.478	at the end of rump-up (1st vertical green dashed line)
	0.551	end of isothermal segment at 900°C

Table 4.5: Variation of mass in the last oxidation and subsequent reduction segments.

time is bigger than the delta of increase of mass due to the previous oxidation step; nevertheless, the bigger amount of mass loss is performed in the dynamic temperature ramp of 10 K/min while only a residual mass loss belongs to the isothermal step of reduction. This shows how the time needed to remove all the anchored compound and recreate oxygen vacancies is longer than the time used in the normal step of reduction. This gives also a good prospect with the assumption that the material can be reused for further cycles and is perfectly regenerable. Another deduction from this reduction is that the temperature of reducibility of the material is located below 900 °C. However, this does not mean that the material is experiencing the desired nickel exsolution phenomena. XRD studies have been introduced for this analysis, which will be clarified later.

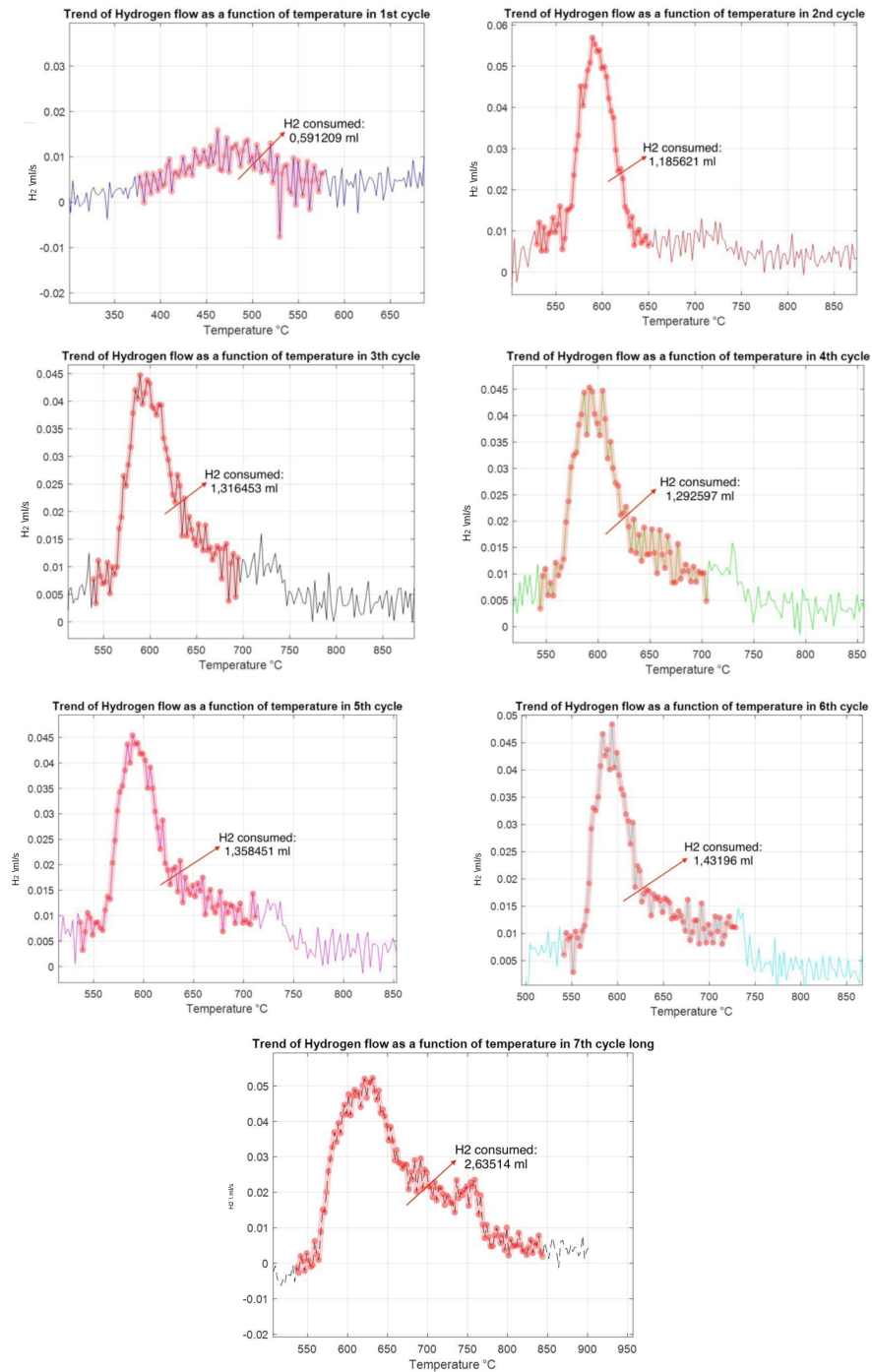


Figure 4.26: Hydrogen reacted in each reduction step of the 6-cycles test with last longer oxidation and subsequent reduction with 20% CO_2 in oxidizing flow. The last picture shows almost doubled consume of the H_2 by the sample mass.

The total amount of H_2 reacted seems to remain swinging from 1,1 up to 2,5 ml for each cycle, a part the last reduction where the calculated hydrogen consumption amounts to 2,6 ml in total. In figure 4.26 are represented the graphs of the hydrogen reacted in in all the cycle. In figure 4.27 all the cycles are plotted overlapping the H_2 reacted, this show how the last reduction consume more Hydrogen due to the bigger amount of mass and also how the reduction is extended for a longer amount of time. Note that the first reduction result outside of the temperature range of the figure 4.27 and so the blue curve representing this cycle remain flat and without major variation. Is possible to see the reducing temperature range of the 1st cycle in figure 4.26.

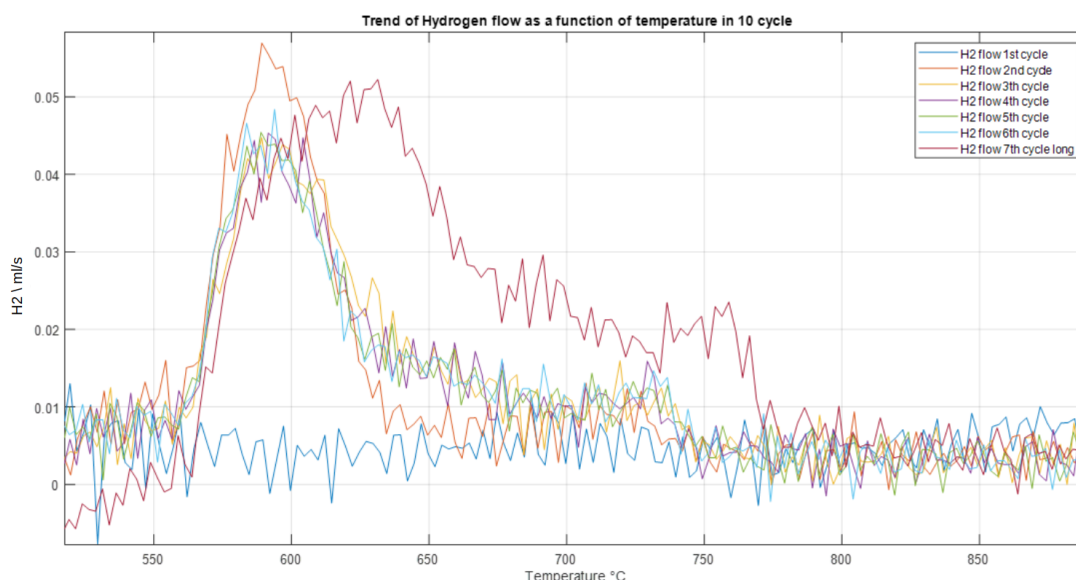


Figure 4.27: H_2 reacted in all the cycles of the eighth TGA test. The overlay shows how the first cycle is out of temperature range compared to the following ones. The last reduction lasts for a longer time and consequently for a much higher temperature range reaching almost 800°C before the reaction tail.

4.3 XRD analysis post-mortem of the TG tested samples

In order to determine the changes in material structure in the various TGA tests, the samples were analysed by the University of Udine using XRD analysis. With these analyses for each sample it was possible to determine which negative factors occurred during the tests and which were positive elements to consider for future studies. First, the structural characteristics of the fresh material were evaluated,

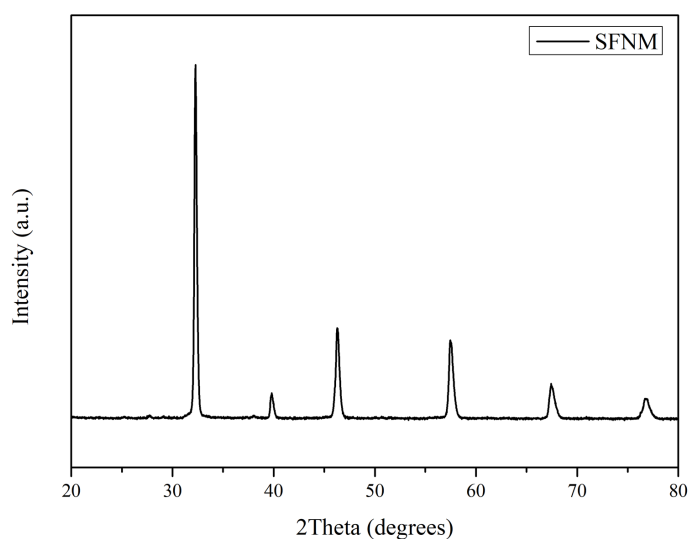


Figure 4.28: XRD peaks of the fresh SFNM-04 sample as synthesized.

again to confirm that over time the samples had not been contaminated and had not seen major changes in their morphology. Figure 4.28 shows that the material has not changed even in the presence of air during the period of time elapsed between its synthesis and the end of the TGA tests. This is an excellent starting point because it allows to make more reliable comparisons between the differences with the samples that have carried out thermochemical cycles in the presence of other atmospheres other than air. Subsequently, the first term of materials released from the thermogravimetry tests has been tested. In particular, the following were considered:

- The sample 1 that saw one single cycle in TPR;
- The sample 2 that saw 4 reoxidation cycles in the air;
- The sample 3 that saw a full cycle of TRP and then a TPO with 20% CO_2 .

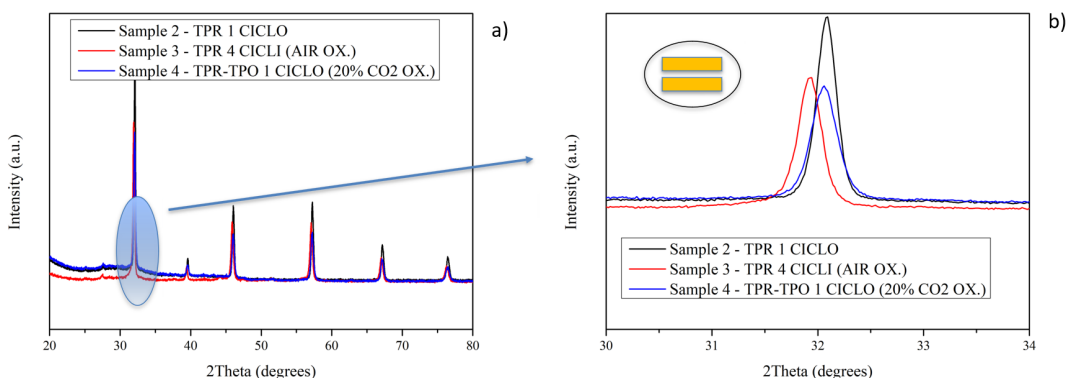


Figure 4.29: XRD curves of the first trio of samples tested. On the right is highlighted the peak of the main perovskite structure common to every sample. This indicates that the primary structure is maintained and does not change during testing.

The results of the trio of samples listed above are shown in the figure 4.29(left). It is important to note that for all three samples, the same structure has been formed, that is, the material always performs the same phase transition, whether it is oxidation in air or oxidation with CO_2 . This is clearly visible in the figure 4.29(right) which shows that the same peak occurred for both air-treated and CO_2 sample. Oxidizing gas does not therefore seem to have influenced the transformation process, presumably it is the temperature that could therefore have the greatest impact in diversifying structures by acting with one type of gas rather than another.

Continuing the analysis of these three samples we can see from the figure 4.30 that instead the phenomenon of exsolution of nickel and the consequent formation of the surface Fe-Ni alloy occurred only in the case of oxidation in air. The zoom on angle 2θ shows how you notice a variation with a peak of the red line corresponding to the sample treated in the air. Consequently, it can be said that for the TPR of 1 cycle and the TPR-TPO in CO_2 the new Ruddlesden Popper (RP) phase

fails to manifest itself, making the material less active from a catalytic point of view as the Ni remains inside the bulk of the matrix and does not bring to the surface facilitating the process of filling the oxygen holidays created during the material reduction step. In fact, this effect of the RP phase had previously occurred in perovskite only at much higher treatment temperatures and with even longer reduction times. The fact is that the air, not containing high concentrations of carbon, certainly helps to inhibit the formation of strontium carbonate and consequently make it easier to reduce as a result of oxidation, which does not thus provide for the splitting of an additional surface compound before the phenomenon of vacancies formation can take place.

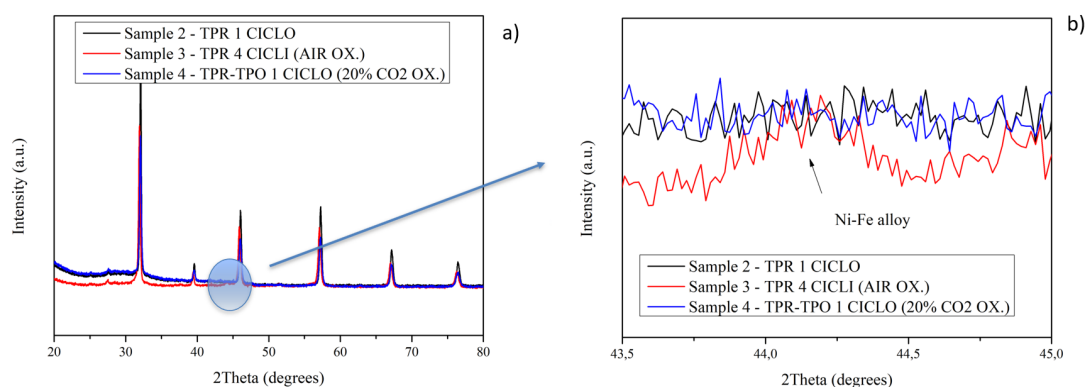


Figure 4.30: XRD curves of the first trio of samples tested a). While b) is a zoom on the $44\text{-}45^\circ$ where peak attributed to Ni-Fe alloy should present.

A final precaution then highlights the formation of $SrMoO_4$ as already seen in preliminary analysis of these tests. The figure 4.31, again, shows the spectrum of X-rays seen from 20 to 80 degrees at the angle of the instrument, this time zooming in on the section corresponding to the peak that determines the presence of the strontium molybdate. The presence of this new compound is revealed for all three samples. This is seen as one of the causes of poor operation of CO_2 splitting material. $SrMoO_4$ segregates in a reducing environment and therefore determines a layer that isolates the perovskite phase from the gas by not allowing the desired interaction between the two components. In addition, it also leads to a favorable path to the formation of strontium carbonate $SrCO_3$ which is formed

by trapping the whole CO_2 molecule without leaving space for the formation of syngas. $SrMoO_4$ would also be a problem when using material for electrochemical reactions. However, presenting this phase in the presence of reducing gases, it then has the function of insulation not allowing even excellent performance from the point of view of electron mobility.

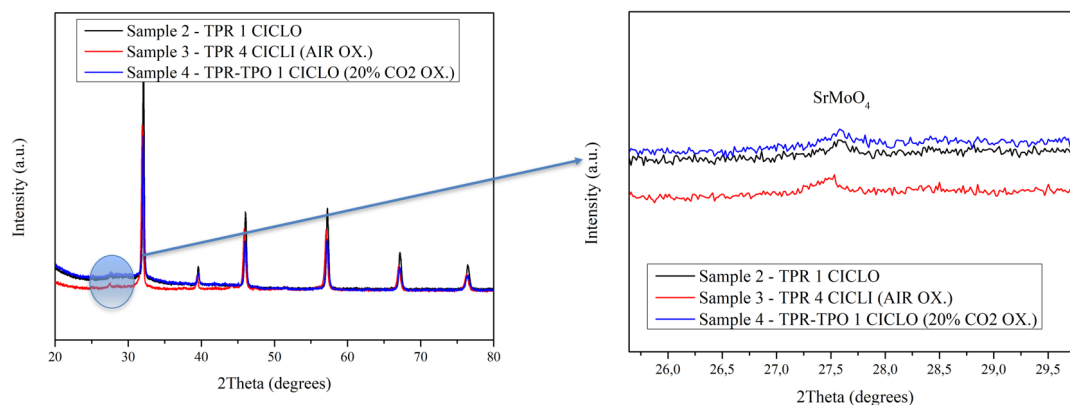


Figure 4.31: XRD curves of the first trio of samples tested a). While b) is a zoom on degrees where strontium molybdate should be seen.

A final analysis on a different sample tern was made. This time the masses analyzed belonged to the following list of tests conducted previously:

- Sample 5: 10-cycles TPR;
- Sample 6: TPR of six cycles with oxidation maintained for a longer time;
- Sample 7: TPR of six cycles with both oxidation and a subsequent reduction both maintained for longer periods of time.

The figure 4.32 again shows the results obtained with the overlapping plot of the last three samples tested. The part concerning the formation of $SrMoO_4$ once again is present in all samples assuming the same drawbacks that occur for the previous sample masses, is highlighted with minus sign in red. The green-plus sign indicates the portion of the graph where there are peaks regarding the formation of the new FeNi alloy. To give a strong difference compared to the previous tests is this time the blue line corresponding to the sample treated with 6 redox cycles

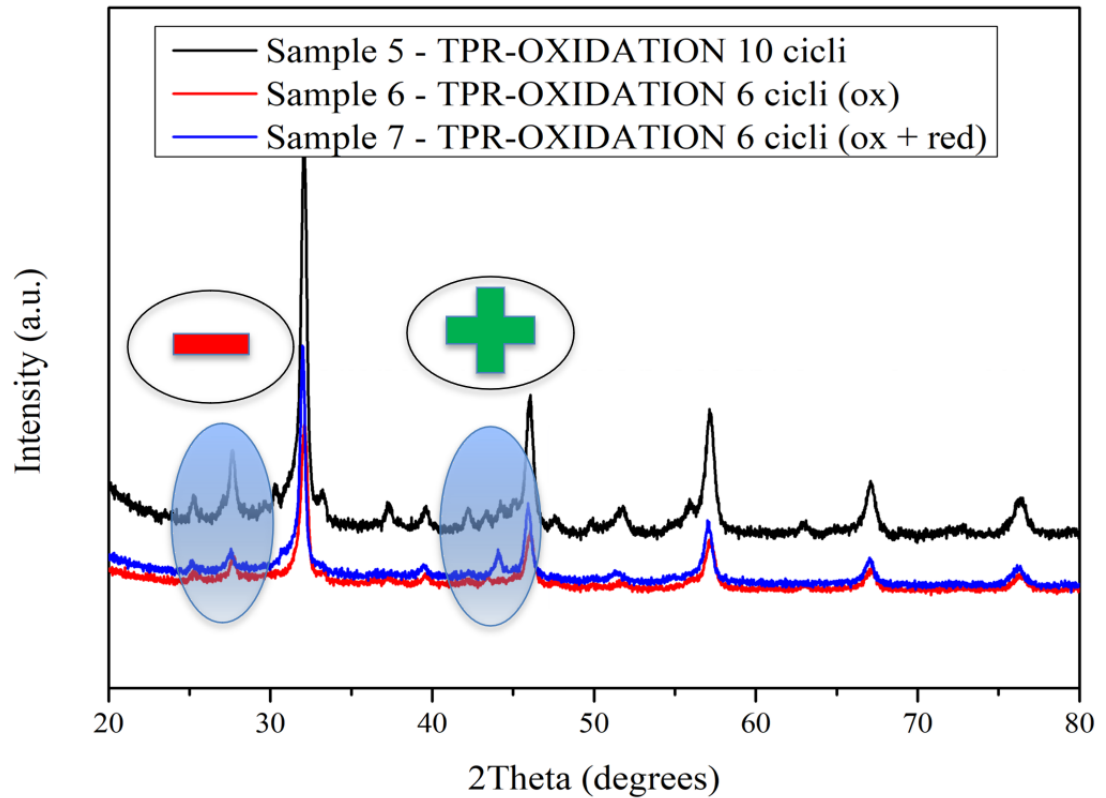


Figure 4.32: XRD curves of the second trio of sample analyzed. With the (+) sign is highlighted the good behavior of the material corresponding to the formation of FeNi alloy. Unlike, the (-) sign shows the formation of $SrMoO_4$ in all the three sample showed.

plus a long oxidation followed by a further long reduction. For this sample it is evident the formation of the FeNi alloy with a much more pronounced peak than the other lines of the other two samples. Indeed, it can be said that at the end of this reduction the RP phase is evident and that the sample behaves as per preliminary results with the creation of surface rock salt.

4.4 Experimental analysis: microreactor characterization

In a second step, the material was prepared and tested in a microreactor to determine whether the conditions in TGA could provide comparable results in a different setup, in which the characterization is based on the measure of the variation on the composition of the gas mixture that is reacting with the sample. To this purpose, a spectrometer was connected inline to the microreactor to determine the gas composition at the outlet for the following tests. In this way, the possible production of CO is determined directly by means of an SEM detector. Each microreactor test was preceded by a calibration of the gas concentration measuring instrument. A quantity closer to the expected one was fluxed to determine the instrument readings compared to the actual ones. From the data obtained above showed in figure 4.16 and 4.23, one would expect at most a CO peak close to 1% for the first oxidation followed by concentrations below 0.2% for the other cycles. A calibration with a CO concentration of 0 to 2% was selected as the best candidate for the detection of such peaks. The table 4.6 names the three tests conducted in microreactor with three different IDs. A brief description of the procedure adopted and the subsection to refer to in the text is also added.

Test ID	Description	subsection n°
S1	TPR with isothermal CO_2 oxidaiton	4.4.1
S2	850°C isothermal redox. 20% CO_2 /Ar oxidation flow	4.4.2
S3	850°C isothermal redox. 50% H_2O /Ar oxidation flow	4.4.3

Table 4.6: Summary table of the three microreactor tests conducted.

4.4.1 Test S1: TPR with isothermal CO_2 oxidation

For the first microreactor test, an attempt was made to simulate the 10-cycles TGA test (see section 4.2.6). In this case the total concentration of hydrogen in the reductive mixture was 0.5%, being already 1% argon inside the cylinder, further mixed at 50% with pure argon. As the estimated CO production would occur in the first moments of oxidative flux, it may be difficult to distinguish it from

the background signal of the instrument. In fact, this signal does not stabilise immediately but takes time to reach its stabilised value. This means that the peak of CO production could be included in the concentration rise curve that the instrument detects for the presence of CO_2 alone. In fact when these two gases are present at the same time the readings of one are strongly influenced by the presence of the second gas. For this reason, when the gas switch is made from a protective argon to an oxidative mixture, the concentration of CO_2 and CO rise together with a rapid slope in the concentration curve which only then tends to stabilise. To overcome this problem, it was decided to send the oxidative flow initially to the reactor bypass, entering the instrument first to allow the signal to stabilise. Only then the flow was redirected back to the reactor, interacting with the material placed inside the crucible and allowing possible CO_2 splitting reactions to occur. On the spectrometer side, the signal, which has been stabilised at certain readings of CO drops back to 0 since in the reactor, during the bypass, remains stuck in pure argon atmosphere. The signal then rises again once the argon has been completely expelled and the new CO_2 mixture is detected again by the spectrometer. If a CO peak occurs, it should be readable just after the zero signal of the instrument. Following the possible peak, the monoxide reading should then return close to the values read during the flow step at the bypass. Unfortunately, it seems that the CO peak does not occur at all or at least is so insignificant that it can be confused with the zero of the instrument. In fact, it cannot be said that conditions of increased CO have occurred. The meter reading before and after the bypass remains within the 0% carbon monoxide range. This first test leads to the conclusion that the variation of derivative predicted in TGA cycles is not actually related to syngas production but totally due to the formation of new compounds that do not include carbon monoxide. It is therefore expected that strontium molybdate predominantly influences the formation of carbonates which act by completely capturing the CO_2 molecule present in the fluxed gas, without releasing any intermediate compounds. In other words, the material is behaving as a perfect capturer of carbon dioxide, but without acting as a producer of syngas.

4.4.2 Test S2: Isothermal redox at 850°C with CO_2 oxidizing environment at 20% vol

It was therefore decided to move away from the conditions used in thermogravimetry, bringing the reduction and oxidation temperatures to values more favorable to the formation of iron-nickel alloys to encourage the capture of oxygen in the oxidizing environment. The following test has therefore foreseen an isothermal situation at 850 °C. Two complete cycles of reduction and oxidation were performed. First, the furnace temperature was brought to the set point. The 50 mg perovskite sample was placed in the furnace beforehand. In this way the air atmosphere was already flushed during the ascent. After reaching 850 °C in the furnace, the air flow was maintained for 60 min to pre-oxidize the sample, favoring the following reduction in hydrogen and ensuring oxidation conditions similar to all other tests performed. The following list organize the steps done in the isothermal experiment.

- Ramp up segment from 25°C to 850°C in air flow of 200 Nml/min;
- Pre-oxidation in air flow for 1 hour;
- Argon purge (100% Ar flow) for 10 min to clean the lines from the air/or CO_2 stream and give a gap from the reductive flow for security reasons;
- Reductive flow of 5% H_2 /Ar for 1 hour;
- Argon purge 10 min to remove the remaining hydrogen into the line;
- Argon purge 5 min into the bypass to clean the bypass stream from possible residual gases;
- 10 min of 20% CO_2 /Ar at the bypass;
- Switch from bypass to furnace with the same CO_2 concentration stream and oxidation for 1 hour of the sample;
- Restart from the purge segment before the hydrogen stream.

This cycle was repeated twice. By avoiding the temperature swing between the reductive and oxidative sections, it was possible to shorten the cycle time, in

addition to having much cleaner instrument readings. The temperature leads to partially influence the reading of the gas concentrations at the outlet. By keeping the oven temperature constant at 850 °C, the exit gas temperature is also constant and allows the entry of the spectrometer without oscillations. In this way, the reading is even cleaner and any changes in the concentration of CO produced are more visible. In this experiment, conditions were increased as much as possible to promote carbon monoxide production. In addition to maintaining a stable temperature optimal for the exsolution phenomenon of iron and nickel, the concentration of H_2 in the mixture was also increased. With a flux of 5% H_2 in argon, in fact, the reduction should be even more encouraged and lead to the maximum formation of FeNi alloy after 60 minutes of dwelling. In the same way the oxidation temperature is kept higher than in the previous tests, from 500 to 850°C allowing better kinetics. The figure 4.33 shows how, despite all the improvements

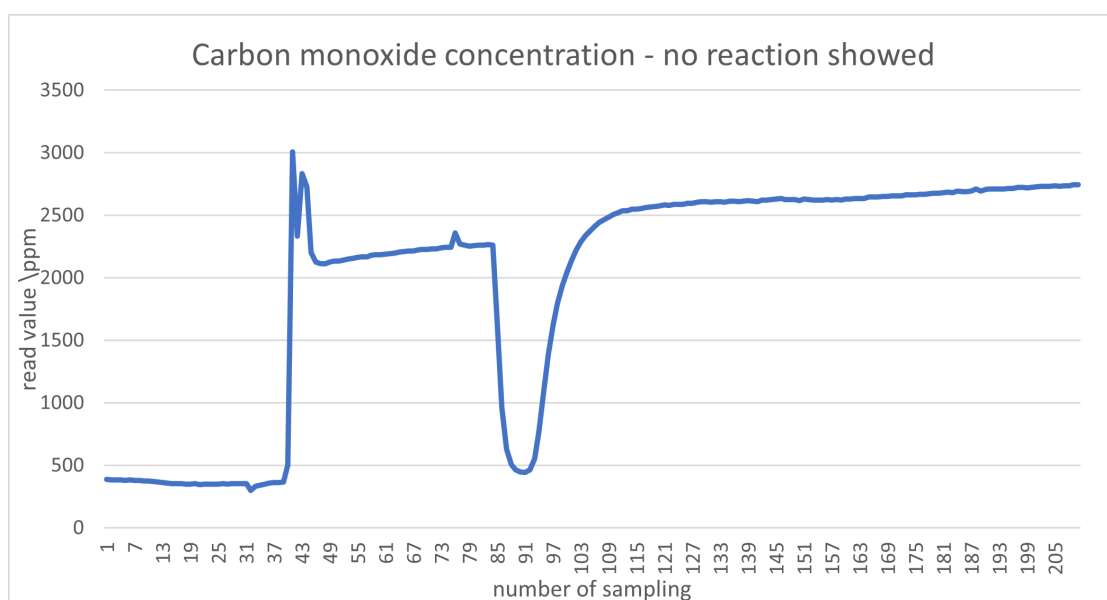


Figure 4.33: Reading value from spectrometer in ppm. the sampling from 40 to 85 regards the bypass section of the gas and the stabilization of the signal near 2200 ppm taken as 0 value. The convexity of the curve indicates the time when the flow returns to the reactor where only Argon atmosphere had previously remained. After sampling 97, one would expect a spike in CO produced.

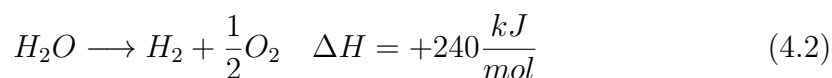
made to the cycle, the expected CO peak does not occur. The extrapolated curve shown belongs in fact to the first oxidation. It should be the most favorable to the

production of CO, coming from a pre-oxidation in air and a strong reduction in hydrogen. Highlighting the details of the concentration curve shown, it can be seen that at the closing of the reactor valve the mixture in bypass sees a peak resulting from the sudden change in pressure without a volume that can dissipate the sudden change. At the bypass afterwards the curve stabilizes with a slightly increasing trend, typical of the instrument drift. When the bypass valve closes, there is a slight oscillation, and then the signal collapses in the presence of the argon that has remained stationary in the furnace section. Once the spectrometer detects the 20% CO_2 oxidizing mixture again, the signal starts to grow again. A peak is expected near samplings 103 onwards, where the signal should have reached its background value. The curve instead stabilizes without showing particular oscillations. No obvious CO production is shown by the instrument. If a minimum yield is present, it is so insignificant to be confused with the instrumental zero.

4.4.3 Test S3: Isothermal test with oxidation in wet environment with 50% H_2O molar fraction

A further test was subsequently performed to verify which phase predominated in deactivating the material for CO production. So far it could be either strontium carbonate formed by the interaction of SrO and CO_2 , or strontium molybdate (segregated in a reductive step) to block CO production. By acting in a water mixture, without the presence of carbon compound, carbonate formation is avoided. In this way it is possible to check if the material undergoes deactivation due to the presence of CO_2 or if the formation of carbonates is just another side effect. The setup was again prepared for two isothermal cycles at the same temperature conditions previously chosen. The only difference from the previous experiment is the different mixture sent to oxidation. This time we opted for a 50% molar mixture of H_2O always carried by a flow of Argon. In this case the water was vaporized and then mixed at room pressure. What is expected as syngas this time is a flow with a H_2 peak during the first oxidation phase. The water, reacting with the perovskite, should give up its oxygen atom to the sample giving birth to molecular hydrogen. The reaction is endothermic therefore favored at high

temperatures. In general, the reaction can be expressed as the equation 4.2.



The water is detected only in trace amounts because upstream of the instrument there is a condenser in order to have a dry stream at the output. The hydrogen reading is even more easily visible from the instrument. Since there are no carbon compounds that can give overlapping readings, it is certain that the density of the signal detected is purely due to the presence of hydrogen. Argon does not alter the H_2 reading. The test was developed according to different segments:

- Ramp up in temperature until 850 °C with air to start the pre-treatment of the sample;
- Dwelling in air for 1 hour to a complete pre-oxidation of the sample before the first reduction occur;
- 10 min in argon purge flow to clean the line and separate the air stream from the hydrogen reductive flow rate;
- 1 hour of reduction in 5% H_2 /Ar flow;
- 10 min of argon purge both for safety reasons and to let the hydrogen signal to stabilize near the background value;
- 30 min of oxidizing flow with water at 50% molar concentration with a carrying gas composed again of pure argon;
- 10 min of cleaning in argon;
- Restart from reduction section.

Again the 5% hydrogen concentration should help the material reduction step along with the 850 °C temperature optimal for the Ni exsolution phenomenon. Moreover, the support given by the bypass line is no longer necessary as it is not necessary to let any signal stabilize before the actual oxidation. Figure 4.34 shows the results of the two consecutive runs. The sampling shown in figure starts at the end of the pre-treatment phase. The hydrogen curve rises abruptly, settling at around

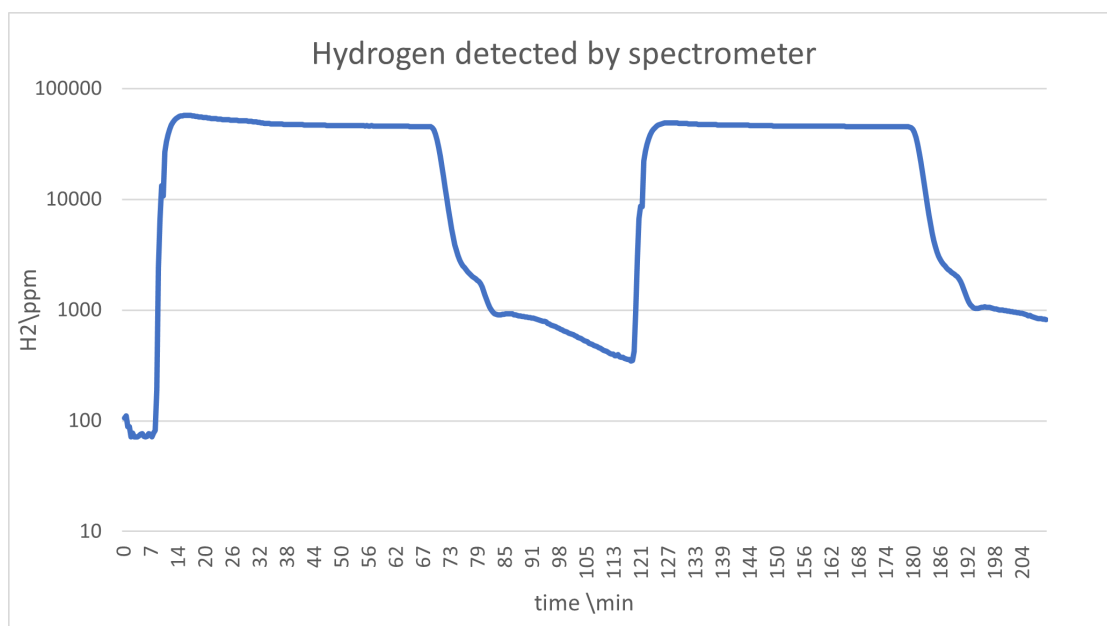


Figure 4.34: sampling of two successive reductions and oxidations at 5% H_2/N_2 and 50% mol of H_2O , respectively. One can see the reductive steps where hydrogen settles at about 5000 ppm. No particular hydrogen production activity due to water splitting was detected in oxidation.

5% concentration (expressed in ppm in the figure). At the end of the reduction, the concentration curve drops in the presence of only fluxed Argon in the reactor. The gas change from Argon to water mixture at 50% molar does not allow even this time to see peaks of H_2 production. In fact, one could expect an abrupt change of slope and the presence of a peak shortly after the 5% concentration drop, when the argon flow ended, the water begins to see the perovskite sample. This seems not to react again leaving the curve without the presence of relevant variations. The signal tends to drift towards lower and lower values, this is due to the stabilization of the instrument that after seeing higher concentrations of hydrogen, it is difficult to return to the initial value detected before the reduction. Following this experiment one can begin to draw inferences about the main cause of deactivation of the material. Strontium molybdate, segregated in the reduction step, completely inhibits the reactivity of the material. The insulating layer that is created on the surface not only stimulates the production of carbonates in the presence of carbon compounds, but also blocks the splitting reaction of the oxidizing

gas and does not allow the reinsertion of oxygen atoms into the matrix of the material. From the syngas production point of view these $Sr_2FeNi_{0.4}Mo_{0.6}O_{6-\delta}$ perovskites do not provide good results being subjected to strong deactivation due to recombination of the atoms composing the material into new phases. Ultimately, although the creation of Fe-Ni alloys should boost syngas production, these alloys are practically never in contact with the gas since a larger phase isolates the active layer from the water present in the fluxing mixture.

4.5 XRD analysis of samples tested in micro-reactor

As for the TGA tests, XRD analyses were also performed for the samples treated in micro-reactor. Four analyses belonging to four different treatments are presented below. The first three samples correspond to the three tests described in the previous section. The last sample tested corresponds to a mass of perovskite only reduced in a 5% H_2/N_2 hydrogen atmosphere. This was done to test whether the material is active to the exsolution phenomenon even after only one reduction step. The four XRD analyses are described in more detail below:

- Sample S1. 50 mg of perovskite which has performed 4 cycles in TPR with isothermal re-oxidation. Trying to emulate the condition of the 10-loop TGA test. So, the concentration of H_2 in the reduction step was set at the 0.5% on the total volume with a set point temperature of 900 °C. The oxidation step instead was set at 500°C with 20% of CO_2 in the flowrate. The sample has been analyzed after the last oxidation.
- Sample S2. 50 mg of perovskite treated in the isothermal test at 850°C both for the reduction and the oxidation segment. As described in section 4.4.1 to enhance the reduction 5% of hydrogen concentration has been set in the reductive segment. The sample was oxidised again at the end of the test.
- Sample S3. 50 mg of perovskite that has seen 2 isothermal cycles at 850°C leaving the reducing hydrogen concentration at 5%, as with Sample S2. This time the oxidation was taking place in the 50% molar environment of H_2O .

Section 4.4.2 refers to this test.

- Sample S4. 50 mg of perovskite only reduced at 850°C in H_2 5%/Ar. During the rump-up in temperature of the furnace the sample has seen Air environment so that a pre-treatment with an initial pre-oxidation could occur.

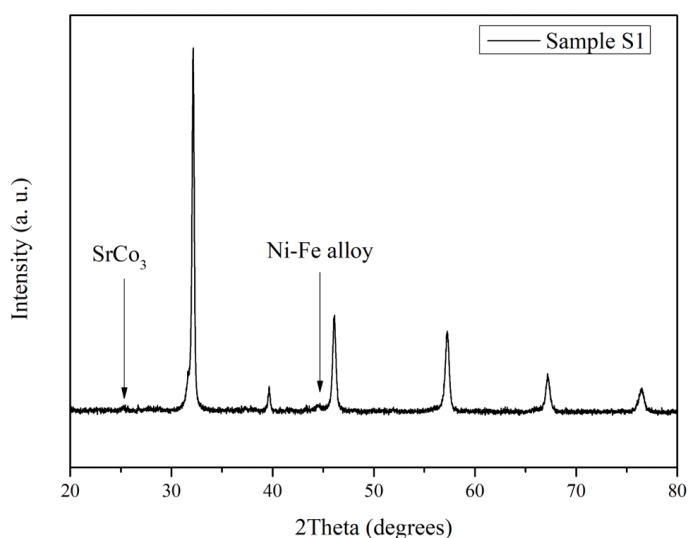


Figure 4.35: XRD signal of the Sample S1 after the emulation of the TGA condition in the micro-reactor setup.

In figure 4.35 the positive aspects are found in the presence of iron-nickel alloy formation highlighted with an arrow in the figure. The main peaks from 20 to 80° are then characteristic of double perovskite with some alterations due to the formation of the RP phase. In particular, a slight malformation of the major peak is noted after 30°. This is due precisely to the RP phase which results in a slight peak partly superimposed on the typical peak of the cubic phase. The figure then shows the carbonates formed by the interaction of CO_2 with the material. This last aspect is just to reconfirm the previous considerations. The material is therefore active in the presence of CO_2 , but interacts in an undesired way, forming the new $SrCO_3$ phase instead of splitting the carbon dioxide molecule. The analysis of the second sample (Sample S2), which had seen an isothermal

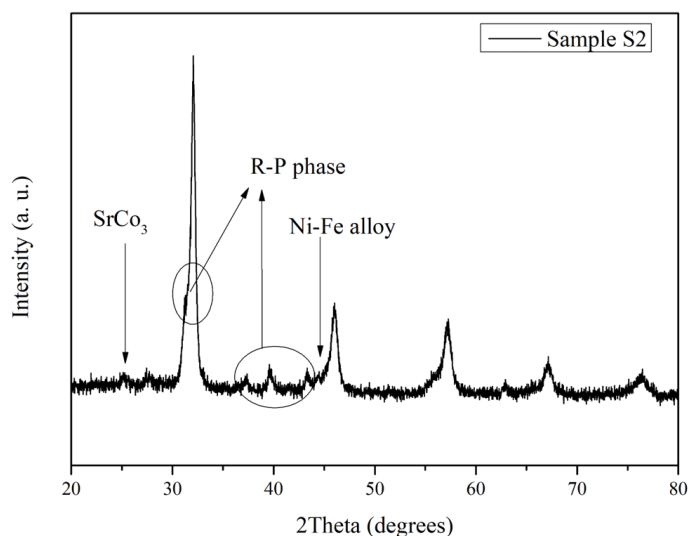


Figure 4.36: XRD data of the Sample S2. This sample has seen 2 isothermal redox loop at 850°C with oxidation in CO_2 environment at 20%.

test with higher hydrogen concentration, turns out to be similar to Sample S1. The same FeNi alloys are created on the surface as well as $SrCO_3$ segregation. Figure 4.36 shows the results in detail. The characteristic deviations from the cubic structure towards the RP phase are highlighted. Thus, it can be deduced that even with the increase in oxidation temperature and the increased amount of hydrogen in reduction, carbonate formation cannot be inhibited. This therefore, could confirm the result obtained in section 4.4.1 in figure 4.33, where no peak in CO production had occurred. Sample S3 and S4 manifest themselves with totally different characteristics seen together in figure 4.37. The characteristics of the peaks in XRD are typical of cubic perovskite and are the same as those of the fresh sample. That is, in these last two analyses it appears that the presence of the two different environments has not altered the material in the least. The water does not act activating the material, it also seems that the presence of a wet flow inhibits the formation of alloys through exsolution phenomena. By not activating the material from the point of view of the mobility of ions in the B-sites, consequently it is not encouraged the formation of the RP phase. The fact that

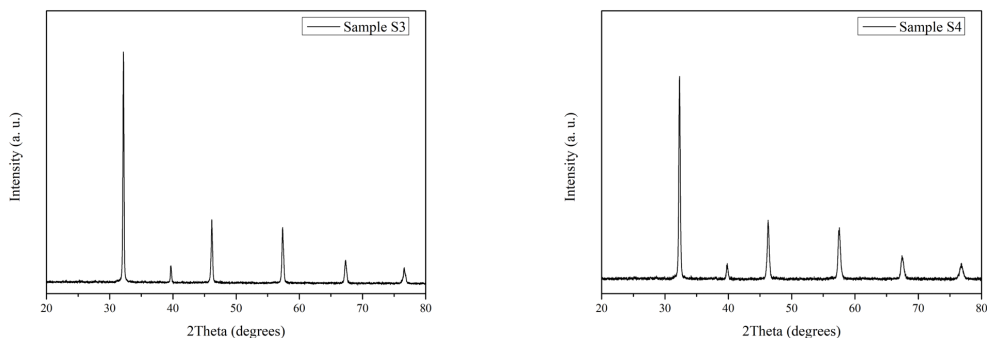


Figure 4.37: XRD analysis of Sample S3 and S4. Both present similar trend of the data-curves which correspond to the peaks of the fresh-SFNM sample as synthesized.

the material in section 4.4.2 figure 4.34 did not see hydrogen production in the oxidizing phase is certainly due to this un-alteration of the perovskite structure. It is obvious that no carbonate formation is present, since there were, in neither of these last two tests, gases containing carbon molecules that could interact with the Sr ions of the A-sites.

Regarding the reduction of Sample S4 alone, this result runs counter to previous results. Indeed, one would expect strong FeNi alloy formation. This is because analyzing a totally reduced sample, the exsolution of nickel should be manifested by bringing to the surface a good amount of material. Nothing happened here, and can be determined by the fact that at least one cyclic oxidation is needed before having a movement of ions from the bulk. Another hypothesis is that the treatment time was not sufficient to ensure nickel movement. In the other tests in fact the material remained at the set-point temperature for a much longer total amount of time. In this case, having performed only one reduction, the perovskite was at the set-point temperature for maximum 1 hour. It is possible that the exsolution of nickel needs more time to begin to manifest itself, which occurred during the tests that included at least two complete cycles at temperature.

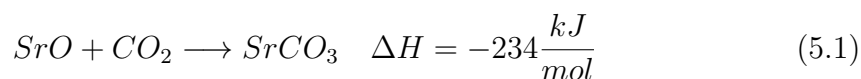
Chapter 5

Summary of the results and further considerations

5.1 Resume of the result obtained

The results obtained through TGA analysis have shown that the material is able to perform repeated thermochemical cycles with good replicability characteristics from the point of view of reduction and oxidation reactions. An analysis in temperature-programmed-reduction shows how the starting temperature reduction of this material settles at about 550 °C with the maximum peak of hydrogen consumption by reaching 600 °C while maintaining an ascent ramp of 20 °C/min. This value is maintained for all tests carried out, both in the presence of subsequent oxidation in air and when the oxidizing gas contains CO_2 . A specific consumption of hydrogen is calculated when at the highest point of the consumption curve of 3 ml/s for each gram of perovskite, corresponding to the lost oxygen value of 2 mg/s per gram of perovskite. This value is seen to remain constant once settled in comparison to the first cycles that can result in slightly higher consumption. In the case of 50% CO_2 oxidation by volume, the value is slightly lower at about 1.7 mg/s of oxygen lost for each gram of material. As seen in Chapter 4, an estimate of CO production in oxidation with CO_2 was initially thought to peak at 0.8% for the first cycle and then fall below 0.2% for the remaining 9 cycles of the full 10-cycle test. Combining the data obtained by the TGA with post-experiment XRD analyses

shows that the formation of strontium carbonate and strontium molybdate plays the primary role in the transformation of the material, attributing the capture of the entire CO_2 molecule for the creation of carbonate. In fact, peaks are displayed at the angle $2\Theta = 27.5^\circ$ to be attributed to the presence of the two species mentioned above. Strontium molybdate ($SrMoO_4$) segregates manifesting itself in a reducing environment, creating an insulating layer at the interface between perovskite and gas thus preventing the correct interaction of perovskite. In addition, it increases the creation of strontium carbonate ($SrCO_3$) that favors the absorption of CO_2 contained in the oxidizing gas, trapping the whole molecule, and not allowing to have a syngas containing CO at the exit. Equation 5.1 shows how the reaction is endothermic. Consequently, it is well favored at the chosen temperatures when the CO_2 flux is present.



For further proof of the phenomena triggered during the various steps of material treatment, similar experiments are also carried out in the microreactor. Results do not show any syngas peak production in the oxidation step, maintaining the constant carbon monoxide detection curve with values that return to calibration indicate a percentage close to zero. The presence of the new iron-nickel alloy is manifested exclusively clearly by the prolonged reduction in H_2 during TGA tests. Confirmed by the presence of the characteristic peak in XRD analysis, it is precisely this alloy that makes the function of catalyst of the reaction leading to a greater yield of syngas at the output. There is also a greater reduction of the material in the prolonged presence of hydrogen in mixture to 900 °C. This leads to the deduction that surely greater exposure to reducing environment would significantly promote the catalytic activity of nickel that is generated on the surface through exsolution processes. The most recent microreactor tests have shown that even in the case of exposure to isothermal cycles at 850°C it is still not possible to obtain CO production in appreciable amount, although the reduction conditions should be closer to those ideal for the formation of exsolved Fe-Ni on the surface, also considering the higher concentration of hydrogen mixed in the microreactor corresponding to 5% by volume compared to the mixture used in TGA which was

only 0.5% in mixture. From these preliminary tests it is evident that the material does not react well in the presence of carbon compound and suffers from a strong deactivation due to the presence of CO_2 .

5.2 Comparison with similar material tested in literature

Du et al. [89] in a study of the electrochemical characteristics of $Sr_2FeMo_{1-x}Ni_xO_{6-\delta}$ perovskite (with $x = 0.25$ and 0.35) found similar molybdate creation phenomena. In particular, the lower nickel concentration further promotes the formation of an additional phase. Precisely, in order to avoid this phenomenon, the study focused on the analysis of the concentration of nickel with $x = 0.35$. The results with higher concentration of nickel were more positive with a stabilization of the sample to a single perovskite phase after the treatment in air. Furthermore, in the same study the effects of nickel exsolution were also investigated. It is assumed the presence of a solid $FeNi_3$ metal phase with floating Fe and Ni contents. Clearly most of the nickel continues to be in the bulk with Ni^{2+} valence, only a small fraction leads to metal formation from the substrate. The data provided by Du et al. study also agree with those obtained during the experimental tests in this thesis. From XPS analysis provided in the work of Du et al. it is also evident that the rate of adsorbed oxygen relative to that of $O_{ad}/O_{lattice}$ matrix is high. That is, there is a strong component due to the formation of adsorbed species (a concrete and more obvious example is the formation of surface carbonates). As a final analysis one can refer to the crystal structure acquired during reduction. A further agreement as the reference mentioned above allows to affirm the presence of a Ruddlesden Popper phase. In order to give an idea of the transformations of the various phases one can refer to the figure 5.1 where the separation of the bulk phase from the external phase is shown. The RP phase, as already introduced in the previous chapters, presents in this specific case a stratification composed of a perovskite $SrFe_{0.5}Mo_{0.5}O_{3-\delta}$ interspersed with a rock salt (in this case SrO). The phase demonstrates good fuel oxidation capabilities due to the $Mo(V)/Mo(VI)$ and $Fe(II)/Fe(III)$ redox couples in octahedral (Fe)O6 and (Mo)O6 structures capable of accepting electrons while losing oxygen at the same time. In addition, the new $SrFe_{1-y}Mo_yO_{3-\delta}$

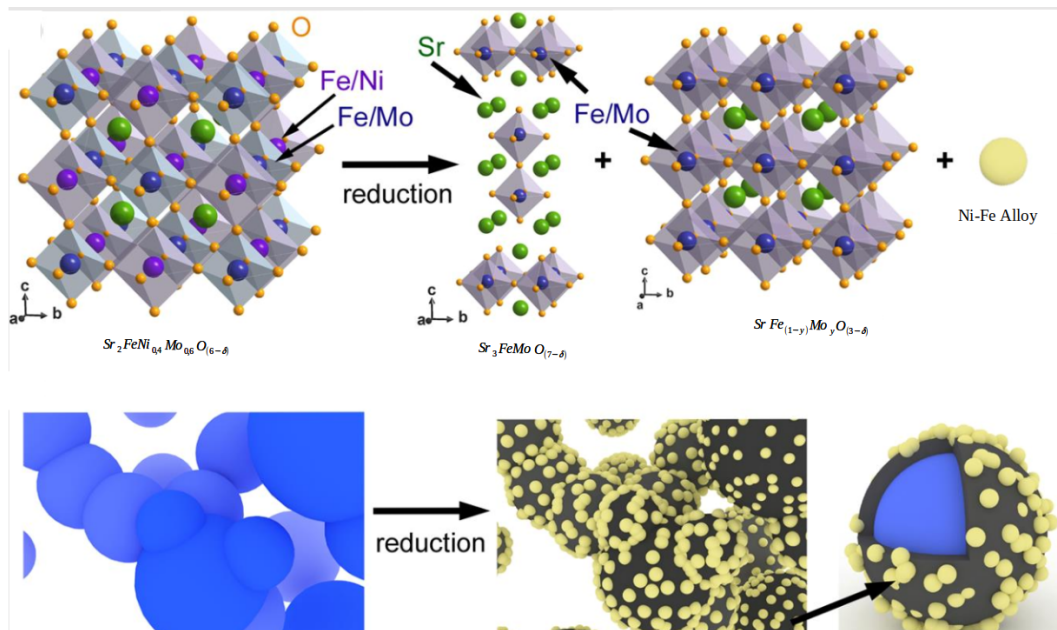


Figure 5.1: Diagram of the transformations that occurred in the material in the reducing phase. The segregation of molybdate is not considered.

phase is also a mixed conductor with excellent structural stability. The structural stability of this sample appears to be very much related to the concentration of nickel present. As the presence of nickel increased, Dai et al. [90] saw a shift in the peaks detected by XRD analysis. In particular, detections with higher nickel concentrations were shifted toward larger 2θ angles, indicating that the elementary cell of SFNM has seen a shrinkage. This according to the literature may be due to two factors in particular. The first factor relates to the smaller ionic radius of the nickel ions compared to those of the material they replace, while the second relates to the conduction orbits of Fe and Mo coming closer to each other again due to the partial replacement of the B-sites [90]. From these good structural characteristics and the adequate reproduction of thermochemical cycles, despite the low carbon monoxide production capacity, the results of the main experiments in TGA can be compared with the literature. Arrivé et al. [91] was chosen because of the similarity present between the material tested by the researchers and that of the present work. In the work present in the literature were considered perovskites of the type LSTN or with the presence of lanthanum, strontium, titanium

and nickel. The structures considered are $La_{2x}Sr_{1-2x}Ti_{1-x}Ni_xO_{3-\delta}$ (LSTN) and $La_{7x/4}Sr_{1-7x/4}Ti_{1-x}Ni_xO_{3-\delta}$ (25LSTN). The starting structure of these compounds is a typical cubic perovskite. RP phase formation in the reducing phase was also not seen. However, the formation of exsolved nickel on the surface with classical $FeNi_3$ alloying was presented. Different nickel concentrations were tested from $x=0.1$ up to $x=0.5$. At lower nickel concentrations, however, agglomeration of oxides (NiO) occurred immediately, which led to the consequent rejection of materials with too low Ni concentration. At nickel concentrations equal to $x=0.3, 0.4$ and 0.5 instead nickel exsolves as expected without agglomerating into oxide. The results of 3 different 2% H_2 reductions in TPR are compared with the data obtained from the experiments in the present work. The figure 5.2 sees the comparison of the

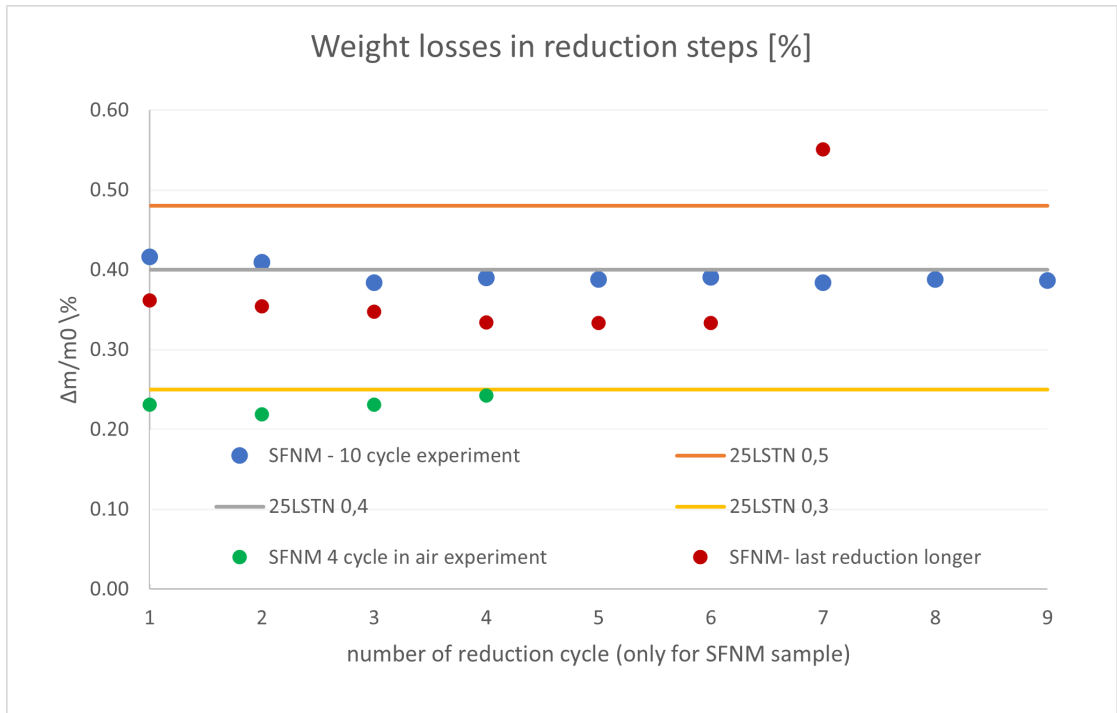


Figure 5.2: Comparison of weight lost in TPR by materials tested in [91] versus tests performed in TGA in this thesis work. The 10-cycle test, the 4-cycle test (both with oxidation in the presence of CO_2), and the 4-cycle test with oxidation in air were chosen.

mass loss in the reducing phase of the 3 samples of 25LSTN at three different nickel concentrations (horizontal lines) compared to the data obtained during each

cycle of the different tests in TGA (colored dots). The temperature ranges are also comparable considering only data of temperatures below 1000C. It can be seen that the mass loss obtained from the tests with reoxidation in CO_2 is very close to the loss of the material 25LSTN with $x=0.4$ (blue circles compared to the gray line), that is the same concentration of Ni present in SFNM. It can be seen then, how the formation of carbonates is also highlighted in this case, for this reason the Δm obtained with reoxidation in air is almost half of the previous ones, arriving at values comparable with perovskite 25LSTN with $x=0.3$ (green circles compared to the yellow line). The red circles concern instead the test with a prolonged reduction. The loss of mass is also clearly greater compared to perovskite 25LSTN with $x=0.5$. This indicates how hydrogen even if present in low concentration in the mixture allows a very strong removal of carbonates previously formed in oxidizing phase with CO_2 . A positive factor of the sample therefore lies in the possibility of reproducing repeatable cycles with all the different mixtures of gases tested. In fact, the material manages to free the surface layer of carbonates by repositioning its mass to the initial reduced state and returning to the original structure of double perovskite.

The latest microreactor tests show no improvement even when increasing the portion of material used (from about 15 mg up to about 50 mg). Carbon monoxide production remains inactive. In addition, the production of H_2 from a wet flow is not stimulated as seen in the previous chapter. This phenomenon is also seen in the 25LSTN material studied by Arrivé et al. [91], where even with the increase in water content in oxidation no particular impact on the hydrolysis phenomena was seen. Although the material did not react to create the desired products, the temperatures chosen for the reductive step seem optimal. In fact at higher temperatures it is true that the reduction of nickel is favored, but the formation of vacancies in the B-sites destabilizes the structure of perovskite and the high temperature also favors the consequent segregation of the A-sites that lead to the decomposition of the structure.

Chapter 6

Conclusion and future prospects

With this thesis a first experimental analysis has been made on a perovskite never tested before in the chemical looping field. The tests conducted so far through thermogravimetric analysis and then with the support of a microreactor have allowed us to begin to outline the first hypothesis on the oxidation-reduction behavior of the sample. The first tests in TGA have essentially demonstrated the reproducibility of the redox cycles and the different behavior of the perovskite $Sr_2FeNi_{0,4}Mo_{0,6}O_{6-\delta}$ in an oxidizing environment in the presence of CO_2 rather than air. In particular it was seen that the air favors in a greater way the reoxidation of the material while the presence of CO_2 does not allow the achievement of a stabilization of the mass regained in the predetermined time of the segments of the different tests. This characteristic is maintained both in the case of concentrations of 20% CO_2 by volume and with larger quantities such as 50% CO_2 by volume. The mass regain in CO_2 mixture is then attributed to carbon deposition due to the formation of new surface carbonates. XRD analysis demonstrated the presence of strontium carbonate ($SrCO_3$) and strontium molybdate ($SrMoO_4$) in the samples. This confirms the deactivation of the material by the presence of carbon compounds and raises new questions about what influence $SrMoO_4$ may have in blocking the re-injection of oxygen into the vacancies generated during the reduction step. The perovskite $Sr_2FeNi_{0,4}Mo_{0,6}O_{6-\delta}$ occurs as a double perovskite structure. During

reduction this structure goes to change giving rise to a new Ruddlesden-Popper phase. This is due to the phenomenon of nickel exsolution that segregating on the surface creates together with iron a new Fe-Ni alloy very active from the catalytic point of view for the capture of oxygen from the oxidizing gas. The following microreactor analysis showed that the insulating phase prevails over the catalytic one, completely inhibiting not only the production of CO from CO_2 , but also a possible splitting of H_2O with the possible generation of H_2 . Ultimately, it appears that with these composition characteristics, even with a Nickel concentration of 0.4 relative to Molybdenum (resulting in $Mo_{0.6}$), this perovskite fails to work optimally with respect to molecule splitting of water and carbon dioxide.

The positive aspects of this analysis are, however, the excellent regeneration capacity of the initial double perovskite phase which can be reconstituted by treating the sample in air at 800 °C for 1 hour. Secondly it generates a strong capture of CO_2 , in fact for the generation of strontium carbonate is the entire CO_2 molecule to be involved in the reaction, without splitting in carbon monoxide. Surely a future step could be to further test for isothermal conditions also in TGA analysis in order to verify more accurately possible differences in mass loss and mass regain with following gas concentrations at the outlet. It has been shown that at certain temperatures and with characteristic gas concentrations, the structure of the material can undergo numerous modifications unfavorable to its operation. With this in mind, research is focused on determining which materials allow for maximum stability during cycling combined with the greatest possible activity towards the generation of oxygen vacancies and ion reacquisition during the following phases. At the same time, materials and compositions are desired that include as many elements as possible that are easy to obtain, economically favorable, and that present characteristics of non-toxicity and easy disposal.

Regarding the future of the chemical looping technology is certainly a promising means for the management of various gas streams and their subsequent transformation through an active material. Obviously, from a theoretical point of view, the ideal future solution is represented by a purely thermal reduction with the use of a solar concentrator. However, this technology suffers from multiple disadvantages. Among the main ones are the strong discontinuity of irradiance, which combined with the large inertia present to reach optimal temperatures greatly limit the field of

application and make the choice of installation site even more fundamental. Other disadvantages are also linked to the realistic temperatures that can be reached with current technologies, which are between 500 and 800 °C. Current materials are not yet sufficiently conducive to reduction to allow changes in their matrix to be seen at such relatively low temperatures. By using a fuel as a reductant many of these problems are eliminated. In addition, hydrogen is one of the "greenest" fuels currently on the market, and hypothetically it could be produced in the same place where the chemical looping plant would be located. Unlike the solar component, hydrogen can be stored and used when needed. For these and other determining factors, the idea of untying from the constraints derived from solar energy could be, if not an alternative, certainly an option to be developed in a synergistic way. So we can think of coupling the production of hydrogen, possibly from solar sources, with a system that can use it directly on site helping to remove CO_2 from the atmosphere and at the same time allowing to have a useful product at the end of the process. This is a concept that fits very well with the most recent policies that aim at an increasingly circular economy. There are many variables yet to be considered before approaching the look toward possible large-scale installations. The technology readiness level (TRL) value of chemical looping using perovskites can be said to be at level 3. In fact, this work has been carried out to experimentally prove the basic concept of this technology. To go to the next level, it will be necessary to validate the technology in the laboratory by finding the best possible material that provides better yields than those that today's metal oxides can provide. Once a promising material for these processes, capable of producing certain syngas yields, is determined, the next step sees a detailed thermodynamic study. In this way it is possible to simulate a stream and determine the flows and the ideal conditions of operation in order to find, in theory, a flow as pure as possible containing a maximum concentration of carbon monoxide. Then the idea is to be able to mix the CO produced with H_2 to have a syngas mixed according to the needs of future uses. The production of chemicals is a way that goes very well with this approach. One can think of ethylene production, methanol, DME or other fischer tropes processes.

In conclusion, we are at the dawn of the discovery of new methods to treat CO_2 and obtain a usable and cost-effective product. Although the road to a mature technology is still long, works like the one carried out in this thesis are necessary

and essential to define which of the many can be the winning technology. Surely in the near future will be discovered many other materials capable of working in these processes and it will come to outline the most favorable path to follow to bring these systems on the market.

Bibliography

- [1] IEA. *Global Energy & CO₂ Status Report 2017*. Paris, 2018. URL: <https://www.iea.org/reports/global-energy-co2-status-report-2017> (cit. on p. 1).
- [2] Intergovernmental Panel on Climate Change. «Summary for Policymakers». In: *Climate Change 2014 Mitigation of Climate Change*. June. Cambridge: Cambridge University Press, 2014, pp. 1–30. ISBN: 9781107415416. DOI: 10.1017/CB09781107415416.005. arXiv: arXiv:1011.1669v3. URL: http://ebooks.cambridge.org/ref/id/CB09781107415416A011%20https://www.cambridge.org/core/product/identifier/CB09781107415416A011/type/book_part (cit. on p. 1).
- [3] Masha Menhat and Y. Yusuf. «Factors influencing the choice of performance measures for the oil and gas supply chain – exploratory study». In: *IOP Conference Series: Materials Science and Engineering* 342.1 (Apr. 2018), p. 012091. ISSN: 1757-8981. DOI: 10.1088/1757-899X/342/1/012091. URL: <https://iopscience.iop.org/article/10.1088/1757-899X/342/1/012091> (cit. on p. 2).
- [4] IEA. *World Energy Model*. Tech. rep. October. Paris: IEA, 2020. URL: <https://www.iea.org/reports/world-energy-model> (cit. on p. 2).
- [5] G. Liu, J. A. Sorensen, J. R. Braunberger, R. Klenner, J. Ge, C. D. Gorecki, E. N. Steadman, and J. A. Harju. «CO₂-Based Enhanced Oil Recovery from Unconventional Reservoirs: A Case Study of the Bakken Formation». In: *Day 2 Wed, April 02, 2014*. SPE, Apr. 2014, pp. 210–216. ISBN: 9781632663177. DOI: 10.2118/168979-MS. URL: <http://www.onepetro.org/doi/10.2118/>

- 168979-MS%20https://onepetro.org/SPEGTS/proceedings/14URC/2-14URC/The%20Woodlands,%20Texas,%20USA/211038 (cit. on p. 2).
- [6] P. L. Spath and D. C. Dayton. «Preliminary Screening – Technical and Economic Assessment of Synthesis Gas to Fuels and Chemicals with Emphasis on the Potential for Biomass-Derived Syngas». In: *National Renewable Energy Laboratory* December (2003), pp. 1–160. ISSN: 0926860X. DOI: 10.2172/15006100. URL: <http://www.dtic.mil/cgi-bin/GetTRDoc?AD=ADA436529&Location=U2&doc=GetTRDoc.pdf%5Cnhttp://www.osti.gov/servlets/purl/15006100-UpKNFn/native/> (cit. on p. 2).
- [7] D.J Wilhelm, D.R Simbeck, A.D Karp, and R.L Dickenson. «Syngas production for gas-to-liquids applications: technologies, issues and outlook». In: *Fuel Processing Technology* 71.1-3 (June 2001), pp. 139–148. ISSN: 03783820. DOI: 10.1016/S0378-3820(01)00140-0. URL: <https://linkinghub.elsevier.com/retrieve/pii/S2542435117300351%20https://linkinghub.elsevier.com/retrieve/pii/S0378382001001400> (cit. on p. 2).
- [8] B. Bulfin, J. Vieten, C. Agrafiotis, M. Roeb, and C. Sattler. «Applications and limitations of two step metal oxide thermochemical redox cycles; a review». In: *Journal of Materials Chemistry A* 5.36 (2017), pp. 18951–18966. ISSN: 2050-7488. DOI: 10.1039/C7TA05025A. URL: <http://xlink.rsc.org/?DOI=C7TA05025A> (cit. on p. 2).
- [9] Christopher Graves, Sune D. Ebbesen, Mogens Mogensen, and Klaus S. Lackner. «Sustainable hydrocarbon fuels by recycling CO₂ and H₂O with renewable or nuclear energy». In: *Renewable and Sustainable Energy Reviews* 15.1 (Jan. 2011), pp. 1–23. ISSN: 13640321. DOI: 10.1016/j.rser.2010.07.014. URL: <http://dx.doi.org/10.1016/j.rser.2010.07.014%20https://linkinghub.elsevier.com/retrieve/pii/S1364032110001942> (cit. on p. 2).
- [10] Seyed Ehsan Hosseini and Mazlan Abdul Wahid. «Hydrogen production from renewable and sustainable energy resources: Promising green energy carrier for clean development». In: *Renewable and Sustainable Energy Reviews* 57 (May 2016), pp. 850–866. ISSN: 13640321. DOI: 10.1016/j.rser.2015.12.112. URL: <http://dx.doi.org/10.1016/j.rser.2015.12.112%20https://>

- [//linkinghub.elsevier.com/retrieve/pii/S1364032115014951](https://linkinghub.elsevier.com/retrieve/pii/S1364032115014951) (cit. on p. 3).
- [11] Dimitrios A. Dimitrakis. «Thermochemical Water and Carbon Dioxide Redox Splitting for Neutral Carbon Footprint Solar Fuels: From Material to Reactor». PhD thesis. 2017, pp. 1–122 (cit. on p. 3).
- [12] IEA. *Transforming Industry through CCUS*. Tech. rep. International Energy Agency, 2019, p. 62. DOI: 10.1787/09689323-en. URL: https://www.oecd-ilibrary.org/energy/transforming-industry-through-ccus%7B%5C_%7D09689323-en (cit. on pp. 3, 4).
- [13] Y. KAYA. «Impact of carbon dioxide emission control on GNP growth : Interpretation of proposed scenarios». In: *Intergovernmental Panel on Climate Change/Response Strategies Working Group, May* (1989). URL: <https://ci.nii.ac.jp/naid/10021966297/en/> (cit. on p. 4).
- [14] M. Muntean, D. Guizzardi, E. Schaaf, M. Crippa, E. Solazzo, J.G.J. Olivier, and E. Vignati. *Fossil CO₂ emissions of all world countries - 2018 Report*. Luxembourg, 2018. ISBN: 978-92-79-97240-9. DOI: 10.2760/30158, JRC113738 . URL: <https://edgar.jrc.ec.europa.eu/overview.php?v=booklet2018> (cit. on p. 6).
- [15] IEA (2019). *Transforming Industry through CCUS*. Ed. by IEA. Paris: OECD, June 2019, p. 62. ISBN: 9789264912557. DOI: 10.1787/09689323-en. URL: https://www.iea.org/reports/transforming-industry-through-ccus%20https://www.oecd-ilibrary.org/energy/transforming-industry-through-ccus_09689323-en (cit. on p. 5).
- [16] Joseph H. Montoya, Linsey C. Seitz, Pongkarn Chakthranont, Aleksandra Vojvodic, Thomas F. Jaramillo, and Jens K. Nørskov. «Materials for solar fuels and chemicals». In: *Nature Materials* 16.1 (Jan. 2017), pp. 70–81. ISSN: 1476-1122. DOI: 10.1038/nmat4778. URL: <http://dx.doi.org/10.1038/nmat4778%20http://www.nature.com/articles/nmat4778> (cit. on p. 8).
- [17] Harry L. Tuller. «Solar to fuels conversion technologies: A perspective». In: *Materials for Renewable and Sustainable Energy* 6.1 (2017). ISSN: 21941467. DOI: 10.1007/s40243-017-0088-2 (cit. on p. 8).

- [18] Christos Agrafiotis, Martin Roeb, and Christian Sattler. «A review on solar thermal syngas production via redox pair-based water/carbon dioxide splitting thermochemical cycles». In: *Renewable and Sustainable Energy Reviews* 42 (2015), pp. 254–285. ISSN: 18790690. DOI: 10.1016/j.rser.2014.09.039 (cit. on pp. 8, 26–28).
- [19] Kevin J. Albrecht, Gregory S. Jackson, and Robert J. Braun. «Evaluating thermodynamic performance limits of thermochemical energy storage subsystems using reactive perovskite oxide particles for concentrating solar power». In: *Solar Energy* 167. September 2017 (2018), pp. 179–193. ISSN: 0038092X. DOI: 10.1016/j.solener.2018.03.078. URL: <https://doi.org/10.1016/j.solener.2018.03.078> (cit. on p. 8).
- [20] Hui Zhao, Nicolas Guillet, Françoise Valdivieso, and Michèle Pijolat. «Preparation and electrical properties of a pyrochlore-related $\text{Ce}_2\text{Zr}_2\text{O}_8\text{-x}$ phase». In: *Solid State Ionics* 160.3-4 (2003), pp. 317–326. ISSN: 01672738. DOI: 10.1016/S0167-2738(03)00207-8 (cit. on p. 8).
- [21] Qingqing Jiang, Guilin Zhou, Zongxuan Jiang, and Can Li. «Thermochemical CO_2 splitting reaction with $\text{CexM}_{1-x}\text{O}_{2-\delta}$ ($\text{M}=\text{Ti}^{4+}$, Sn^{4+} , Hf^{4+} , Zr^{4+} , La^{3+} , Y^{3+} and Sm^{3+}) solid solutions». In: *Solar Energy* 99 (2014), pp. 55–66. ISSN: 0038092X. DOI: 10.1016/j.solener.2013.10.021 (cit. on p. 8).
- [22] Global CCS Institute. «Global Status of CCS 2020». In: *Global CCS Institute* June (2020). URL: <https://www.globalccsinstitute.com/resources/global-status-report/> (cit. on p. 10).
- [23] Dennis Y.C. Leung, Giorgio Caramanna, and M. Mercedes Maroto-Valer. «An overview of current status of carbon dioxide capture and storage technologies». In: *Renewable and Sustainable Energy Reviews* 39 (Nov. 2014), pp. 426–443. ISSN: 13640321. DOI: 10.1016/j.rser.2014.07.093. URL: <http://dx.doi.org/10.1016/j.rser.2014.07.093><https://linkinghub.elsevier.com/retrieve/pii/S1364032114005450> (cit. on pp. 10, 12).
- [24] Tim C. Merkel, Haiqing Lin, Xiaotong Wei, and Richard Baker. «Power plant post-combustion carbon dioxide capture: An opportunity for membranes». In: *Journal of Membrane Science* 359.1-2 (Sept. 2010), pp. 126–139. ISSN: 03767388. DOI: 10.1016/j.memsci.2009.10.041. URL: <http://dx.doi.org/10.1016/j.memsci.2009.10.041>

- org/10.1016/j.memsci.2009.10.041%20https://linkinghub.elsevier.com/retrieve/pii/S0376738809007832 (cit. on p. 11).
- [25] P CHIESA, G LOZZA, A MALANDRINO, M ROMANO, and V PICCOLO. «Three-reactors chemical looping process for hydrogen production». In: *International Journal of Hydrogen Energy* 33.9 (May 2008), pp. 2233–2245. ISSN: 03603199. DOI: 10.1016/j.ijhydene.2008.02.032. URL: <https://linkinghub.elsevier.com/retrieve/pii/S0360319908002085> (cit. on p. 11).
- [26] Mohamed A. Habib, Medhat Nemitallah, and Rached Ben-Mansour. «Recent Development in Oxy-Combustion Technology and Its Applications to Gas Turbine Combustors and ITM Reactors». In: *Energy & Fuels* 27.1 (Jan. 2013), pp. 2–19. ISSN: 0887-0624. DOI: 10.1021/ef301266j. URL: <https://pubs.acs.org/doi/10.1021/ef301266j> (cit. on p. 11).
- [27] Imo Pfaff and Alfons Kather. «Comparative thermodynamic analysis and integration issues of CCS steam power plants based on oxy-combustion with cryogenic or membrane based air separation». In: *Energy Procedia* 1.1 (Feb. 2009), pp. 495–502. ISSN: 18766102. DOI: 10.1016/j.egypro.2009.01.066. URL: <http://dx.doi.org/10.1016/j.egypro.2009.01.066%20https://linkinghub.elsevier.com/retrieve/pii/S1876610209000678> (cit. on p. 11).
- [28] Medhat A. Nemitallah, Mohamed A. Habib, Hassan M. Badr, Syed A. Said, Aqil Jamal, Rached Ben-Mansour, Esmail M. A. Mokheimer, and K. Mezghani. «Oxy-fuel combustion technology: current status, applications, and trends». In: *International Journal of Energy Research* 41.12 (Oct. 2017), pp. 1670–1708. ISSN: 0363907X. DOI: 10.1002/er.3722. arXiv: arXiv:1011.1669v3. URL: <http://doi.wiley.com/10.1002/er.3722> (cit. on pp. 11, 12).
- [29] Maciej Chorowski and Wojciech Gizicki. «Technical and economic aspects of oxygen separation for oxy-fuel purposes». In: *Archives of Thermodynamics* 36.1 (Mar. 2015), pp. 157–170. ISSN: 2083-6023. DOI: 10.1515/aoter-2015-0011. URL: <http://journals.pan.pl/dlibra/publication/109103/edition/94731/content> (cit. on p. 12).

- [30] Charles R. Jenkins et al. «Safe storage and effective monitoring of CO₂ in depleted gas fields». In: *Proceedings of the National Academy of Sciences* 109.2 (Jan. 2012), E35–E41. ISSN: 0027-8424. DOI: 10.1073/pnas.1107255108. URL: <http://www.pnas.org/cgi/doi/10.1073/pnas.1107255108> (cit. on p. 12).
- [31] Zhihong Yuan, Mario R. Eden, and Rafiqul Gani. «Toward the Development and Deployment of Large-Scale Carbon Dioxide Capture and Conversion Processes». In: *Industrial & Engineering Chemistry Research* 55.12 (Mar. 2016), pp. 3383–3419. ISSN: 0888-5885. DOI: 10.1021/acs.iecr.5b03277. URL: <https://pubs.acs.org/doi/10.1021/acs.iecr.5b03277> (cit. on p. 12).
- [32] James M. Tour, Carter Kittrell, and Vicki L. Colvin. «Green carbon as a bridge to renewable energy». In: *Nature Materials* 9.11 (Nov. 2010), pp. 871–874. ISSN: 1476-1122. DOI: 10.1038/nmat2887. URL: <http://dx.doi.org/10.1038/nmat2887> (cit. on p. 13).
- [33] Chih Hung Huang and Chung Sung Tan. «A review: CO₂ utilization». In: *Aerosol and Air Quality Research* 14.2 (2014), pp. 480–499. ISSN: 16808584. DOI: 10.4209/aaqr.2013.10.0326 (cit. on p. 13).
- [34] Michele Aresta. «Carbon Dioxide: Utilization Options to Reduce its Accumulation in the Atmosphere». In: *Carbon Dioxide as Chemical Feedstock*. Weinheim, Germany: Wiley-VCH Verlag GmbH & Co. KGaA, 2010, pp. 1–13. ISBN: 9783527324750. DOI: 10.1002/9783527629916.ch1. URL: <http://doi.wiley.com/10.1002/9783527629916.ch1> (cit. on p. 13).
- [35] Niklas von der Assen, Johannes Jung, and André Bardow. «Life-cycle assessment of carbon dioxide capture and utilization: avoiding the pitfalls». In: *Energy & Environmental Science* 6.9 (2013), p. 2721. ISSN: 1754-5692. DOI: 10.1039/c3ee41151f. URL: <http://xlink.rsc.org/?DOI=C5TC02043C%20http://xlink.rsc.org/?DOI=c3ee41151f> (cit. on p. 14).
- [36] Samuel C. Bayham, Andrew Tong, Mandar Kathe, and Liang Shih Fan. «Chemical looping technology for energy and chemical production». In: *Wiley Interdisciplinary Reviews: Energy and Environment* 5.2 (2016), pp. 216–241. ISSN: 2041840X. DOI: 10.1002/wene.173 (cit. on pp. 14, 16).

- [37] Ann J. Traynor and Reed J. Jensen. «Direct Solar Reduction of CO₂ to Fuel: First Prototype Results». In: *Industrial & Engineering Chemistry Research* 41.8 (Apr. 2002), pp. 1935–1939. ISSN: 0888-5885. DOI: 10.1021/ie010871x. URL: <https://pubs.acs.org/doi/10.1021/ie010871x> (cit. on p. 15).
- [38] Peter T. Krenzke and Jane H. Davidson. «Thermodynamic Analysis of Syngas Production via the Solar Thermochemical Cerium Oxide Redox Cycle with Methane-Driven Reduction». In: *Energy & Fuels* 28.6 (June 2014), pp. 4088–4095. ISSN: 0887-0624. DOI: 10.1021/ef500610n. URL: <https://pubs.acs.org/doi/10.1021/ef500610n> (cit. on p. 21).
- [39] Hadi Ebrahimi and Mohammad Rahmani. «Modeling chemical looping syngas production in a microreactor using perovskite oxygen carriers». In: *International Journal of Hydrogen Energy* 43.10 (2018), pp. 5231–5248. ISSN: 03603199. DOI: 10.1016/j.ijhydene.2018.01.108. URL: <https://doi.org/10.1016/j.ijhydene.2018.01.108> (cit. on pp. 21, 22).
- [40] Ion Iliuta, Raul Tahoces, Gregory S. Patience, Sebastien Riffart, and Francis Luck. «Chemical-looping combustion process: Kinetics and mathematical modeling». In: *AIChE Journal* 59.4 (2010), NA–NA. ISSN: 00011541. DOI: 10.1002/aic.11967. URL: <http://doi.wiley.com/10.1002/aic.11967> (cit. on pp. 23, 26).
- [41] L. García. «Hydrogen production by steam reforming of natural gas and other nonrenewable feedstocks». In: *Compendium of Hydrogen Energy*. 2015. Elsevier, 2015, pp. 83–107. ISBN: 9781782423614. DOI: 10.1016/B978-1-78242-361-4.00004-2. URL: <https://linkinghub.elsevier.com/retrieve/pii/B9781782423614000042> (cit. on pp. 23, 24).
- [42] Prabir Basu. «Gasification Theory». In: *Biomass Gasification, Pyrolysis and Torrefaction*. Elsevier, 2018, pp. 211–262. ISBN: 9780128129920. DOI: 10.1016/B978-0-12-812992-0.00007-8. URL: <https://linkinghub.elsevier.com/retrieve/pii/B9780128129920000078> (cit. on p. 25).
- [43] Azharuddin Farooqui, Archishman Bose, Marta Boaro, Jordi Llorca, and Massimo Santarelli. «Assessment of integration of methane-reduced ceria chemical looping CO₂/H₂O splitting cycle to an oxy-fired power plant». In: *International Journal of Hydrogen Energy* 45.11 (2020), pp. 6184–6206.

- ISSN: 03603199. DOI: 10.1016/j.ijhydene.2019.12.182. URL: <https://doi.org/10.1016/j.ijhydene.2019.12.182> (cit. on p. 26).
- [44] Deepak Yadav and Rangan Banerjee. «A review of solar thermochemical processes». In: *Renewable and Sustainable Energy Reviews* 54 (2016), pp. 497–532. ISSN: 18790690. DOI: 10.1016/j.rser.2015.10.026. URL: <http://dx.doi.org/10.1016/j.rser.2015.10.026> (cit. on pp. 26, 27).
- [45] Mingchen Tang, Long Xu, and Maohong Fan. «Progress in oxygen carrier development of methane-based chemical-looping reforming: A review». In: *Applied Energy* 151 (2015), pp. 143–156. ISSN: 03062619. DOI: 10.1016/j.apenergy.2015.04.017. URL: <http://dx.doi.org/10.1016/j.apenergy.2015.04.017> (cit. on p. 26).
- [46] Greg P. Smestad and Aldo Steinfeld. «Review: Photochemical and thermochemical production of solar fuels from H₂O and CO₂ using metal oxide catalysts». In: *Industrial and Engineering Chemistry Research* 51.37 (2012), pp. 11828–11840. ISSN: 08885885. DOI: 10.1021/ie3007962 (cit. on p. 26).
- [47] Irina Vishnevetsky, Alexander Berman, and Michael Epstein. «Features of solar thermochemical redox cycles for hydrogen production from water as a function of reactants' main characteristics». In: *International Journal of Hydrogen Energy* 36.4 (2011), pp. 2817–2830. ISSN: 03603199. DOI: 10.1016/j.ijhydene.2010.11.027. URL: <http://dx.doi.org/10.1016/j.ijhydene.2010.11.027> (cit. on p. 27).
- [48] William C. Chueh and Sossina M. Haile. «A thermochemical study of ceria: Exploiting an old material for new modes of energy conversion and CO₂ mitigation». In: *Philosophical Transactions of the Royal Society A: Mathematical, Physical and Engineering Sciences* 368.1923 (2010), pp. 3269–3294. ISSN: 1364503X. DOI: 10.1098/rsta.2010.0114 (cit. on p. 29).
- [49] Michael Welte, Kent Warren, Jonathan R. Scheffe, and Aldo Steinfeld. «Combined Ceria Reduction and Methane Reforming in a Solar-Driven Particle-Transport Reactor». In: *Industrial and Engineering Chemistry Research* 56.37 (2017), pp. 10300–10308. ISSN: 15205045. DOI: 10.1021/acs.iecr.7b02738 (cit. on p. 29).

- [50] H. Evan Bush and Peter G. Loutzenhiser. «Solar electricity via an Air Brayton cycle with an integrated two-step thermochemical cycle for heat storage based on Fe₂O₃/Fe₃O₄ redox reactions: Thermodynamic and kinetic analyses». In: *Solar Energy* 174. September (2018), pp. 617–627. ISSN: 0038092X. DOI: 10.1016/j.solener.2018.09.043. URL: <https://doi.org/10.1016/j.solener.2018.09.043> (cit. on p. 29).
- [51] G. Voitic and V. Hacker. «Recent advancements in chemical looping water splitting for the production of hydrogen». In: *RSC Advances* 6.100 (2016), pp. 98267–98296. ISSN: 20462069. DOI: 10.1039/c6ra21180a. URL: <http://dx.doi.org/10.1039/C6RA21180A> (cit. on pp. 30, 32).
- [52] Alexandra Navrotsky. «Energetics and Crystal Chemical Systematics among Ilmenite, Lithium Niobate, and Perovskite Structures». In: *Chemistry of Materials* 10.10 (Oct. 1998), pp. 2787–2793. ISSN: 0897-4756. DOI: 10.1021/cm9801901. URL: <https://pubs.acs.org/doi/10.1021/cm9801901> (cit. on pp. 31, 32).
- [53] Qingqing Jiang, Jinhui Tong, Guilin Zhou, Zongxuan Jiang, Zhen Li, and Can Li. «Thermochemical CO₂ splitting reaction with supported La_xA_{1-x}FeyB_{1-y}O₃ (A=Sr, Ce, B=Co, Mn; 0≤x, y≤1) perovskite oxides». In: *Solar Energy* 103 (2014), pp. 425–437. ISSN: 0038092X. DOI: 10.1016/j.solener.2014.02.033 (cit. on pp. 33, 34).
- [54] Chih Kai Yang, Yoshihiro Yamazaki, Aykut Aydin, and Sossina M. Haile. «Thermodynamic and kinetic assessments of strontium-doped lanthanum manganite perovskites for two-step thermochemical water splitting». In: *Journal of Materials Chemistry A* 2.33 (2014), pp. 13612–13623. ISSN: 20507496. DOI: 10.1039/c4ta02694b. URL: <http://dx.doi.org/10.1039/C4TA02694B> (cit. on pp. 35, 36).
- [55] Sunita Dey, B. S. Naidu, A. Govindaraj, and C. N.R. Rao. «Noteworthy performance of La_{1-x}CaxMnO₃ perovskites in generating H₂ and CO by the thermochemical splitting of H₂O and CO₂». In: *Physical Chemistry Chemical Physics* 17.1 (2015), pp. 122–125. ISSN: 14639076. DOI: 10.1039/c4cp04578e. URL: <http://dx.doi.org/10.1039/C4CP04578E> (cit. on pp. 35, 37).

- [56] C. N.R. Rao and Sunita Dey. «Generation of H₂ and CO by solar thermochemical splitting of H₂O and CO₂ by employing metal oxides». In: *Journal of Solid State Chemistry* 242 (2016), pp. 107–115. ISSN: 1095726X. DOI: 10.1016/j.jssc.2015.12.018. URL: <http://dx.doi.org/10.1016/j.jssc.2015.12.018> (cit. on pp. 37, 43).
- [57] Qiongqiong Jiang, Hao Zhang, Yali Cao, Hui Hong, and Hongguang Jin. «Solar hydrogen production via perovskite-based chemical-looping steam methane reforming». In: *Energy Conversion and Management* 187.March (2019), pp. 523–536. ISSN: 01968904. DOI: 10.1016/j.enconman.2019.01.112. URL: <https://doi.org/10.1016/j.enconman.2019.01.112> (cit. on pp. 37, 39, 40).
- [58] Kun Zhao, Anqing Zheng, Haibin Li, Fang He, Zhen Huang, Guoqiang Wei, Yang Shen, and Zengli Zhao. «Exploration of the mechanism of chemical looping steam methane reforming using double perovskite-type oxides La_{1.6}Sr_{0.4}FeCoO₆». In: *Applied Catalysis B: Environmental* 219 (2017), pp. 672–682. ISSN: 09263373. DOI: 10.1016/j.apcatb.2017.08.027. URL: <http://dx.doi.org/10.1016/j.apcatb.2017.08.027> (cit. on pp. 39, 41).
- [59] Bryan J. Hare, Debtanu Maiti, Swetha Ramani, Adela E. Ramos, Venkat R. Bhethanabotla, and John N. Kuhn. «Thermochemical conversion of carbon dioxide by reverse water-gas shift chemical looping using supported perovskite oxides». In: *Catalysis Today* 323.February 2018 (2019), pp. 225–232. ISSN: 09205861. DOI: 10.1016/j.cattod.2018.06.002. URL: <https://doi.org/10.1016/j.cattod.2018.06.002> (cit. on pp. 39, 42).
- [60] Hartley et al. «CO₂ to Syngas: Metal Oxides on Stainless Steel 316L for micro-channel reactor application». In: *International Conference on Chemical and Biochemical Engineering* 20-22 (July 2015), pp. 8–11. URL: https://www.researchgate.net/profile/Mahdi_Belguidoum/publication/289540155_AbstractsBook_ICCBE2015/links/5690232b08aec14fa557e115/AbstractsBook-ICCBE2015.pdf (cit. on pp. 42, 43).
- [61] Qingqing Jiang, Zhenpan Chen, Jinhui Tong, Min Yang, Zongxuan Jiang, and Can Li. «Catalytic Function of IrO_x in the Two-Step Thermochemical CO₂-Splitting Reaction at High Temperatures». In: *ACS Catalysis* 6.2 (2016),

- pp. 1172–1180. ISSN: 21555435. DOI: 10.1021/acscatal.5b01774 (cit. on p. 43).
- [62] Nobuyuki Gokon, Toshinori Suda, and Tatsuya Kodama. «Oxygen and hydrogen productivities and repeatable reactivity of 30-mol%-Fe-, Co-, Ni-, Mn-doped CeO₂- δ for thermochemical two-step water-splitting cycle». In: *Energy* 90 (2015), pp. 1280–1289. ISSN: 03605442. DOI: 10.1016/j.energy.2015.06.085. URL: <http://dx.doi.org/10.1016/j.energy.2015.06.085> (cit. on p. 43).
- [63] Martin Roeb et al. «Solar hydrogen production by a two-step cycle based on mixed iron oxides». In: *Journal of Solar Energy Engineering, Transactions of the ASME* 128.2 (2006), pp. 125–133. ISSN: 01996231. DOI: 10.1115/1.2183804 (cit. on p. 43).
- [64] Martin Roeb, Martina Neises, Nathalie Monnerie, Friedemann Call, Heike Simon, Christian Sattler, Martin Schmücker, and Robert Pitz-Paal. «Materials-related aspects of thermochemical water and carbon dioxide splitting: A review». In: *Materials* 5.11 (2012), pp. 2015–2054. ISSN: 19961944. DOI: 10.3390/ma5112015 (cit. on p. 43).
- [65] L. S. Darken and R. W. Gurry. «The System Iron-Oxygen. II. Equilibrium and Thermodynamics of Liquid Oxide and Other Phases». In: *Journal of the American Chemical Society* 68.5 (1946), pp. 798–816. ISSN: 15205126. DOI: 10.1021/ja01209a030 (cit. on p. 43).
- [66] Alex Le Gal and Stéphane Abanades. «Catalytic investigation of ceria-zirconia solid solutions for solar hydrogen production». In: *International Journal of Hydrogen Energy* 36.8 (2011), pp. 4739–4748. ISSN: 03603199. DOI: 10.1016/j.ijhydene.2011.01.078 (cit. on p. 43).
- [67] Anthony H. McDaniel, Elizabeth C. Miller, Darwin Arifin, Andrea Ambrosini, Eric N. Coker, Ryan O’Hayre, William C. Chueh, and Jianhua Tong. «Sr- and Mn-doped LaAlO₃- δ for solar thermochemical H₂ and CO production». In: *Energy and Environmental Science* 6.8 (2013), pp. 2424–2428. ISSN: 17545692. DOI: 10.1039/c3ee41372a (cit. on pp. 43, 44).

- [68] M. E. Gálvez, R. Jacot, J. Scheffe, T. Cooper, G. Patzke, and A. Steinfeld. «Physico-chemical changes in Ca, Sr and Al-doped La-Mn-O perovskites upon thermochemical splitting of CO₂ via redox cycling». In: *Physical Chemistry Chemical Physics* 17.9 (2015), pp. 6629–6634. ISSN: 14639076. DOI: 10.1039/c4cp05898d. URL: <http://dx.doi.org/10.1039/C4CP05898D> (cit. on p. 45).
- [69] Sunita Dey, B. S. Naidu, and C. N.R. Rao. «Beneficial effects of substituting trivalent ions in the B-site of La_{0.5}Sr_{0.5}Mn_{1-x}AxO₃ (A = Al, Ga, Sc) on the thermochemical generation of CO and H₂ from CO₂ and H₂O». In: *Dalton Transactions* 45.6 (2016), pp. 2430–2435. ISSN: 14779234. DOI: 10.1039/c5dt04822b (cit. on p. 46).
- [70] Antoine Demont and Stéphane Abanades. «Solar thermochemical conversion of CO₂ into fuel via two-step redox cycling of non-stoichiometric Mn-containing perovskite oxides». In: *Journal of Materials Chemistry A* 3.7 (2015), pp. 3536–3546. ISSN: 20507496. DOI: 10.1039/c4ta06655c (cit. on p. 47).
- [71] Nathan L. Galinsky, Yan Huang, Arya Shafiefarhood, and Fanxing Li. «Iron oxide with facilitated O₂- transport for facile fuel oxidation and CO₂ capture in a chemical looping scheme». In: *ACS Sustainable Chemistry and Engineering* 1.3 (2013), pp. 364–373. ISSN: 21680485. DOI: 10.1021/sc300177 (cit. on p. 48).
- [72] Sravanthi Loganathan, Ravi Babu Valapa, Raghvendra Kumar Mishra, G. Pugazhenthii, and Sabu Thomas. «Thermogravimetric Analysis for Characterization of Nanomaterials». In: *Thermal and Rheological Measurement Techniques for Nanomaterials Characterization*. Vol. 3. Elsevier, 2017, pp. 67–108. ISBN: 9780323461450. DOI: 10.1016/B978-0-323-46139-9.00004-9. URL: <http://dx.doi.org/10.1016/B978-0-323-46139-9.00004-9>
<https://linkinghub.elsevier.com/retrieve/pii/B9780323461399000049> (cit. on pp. 51, 54).
- [73] NETZSCH. *Sta 2500 Regulus Brochure*. 2020. URL: <https://www.netzsch-thermal-analysis.com/it/prodotti-soluzioni/termogravimetria-calorimetria-differenziale-a-scansione-in-simultanea/sta-2500-regulus/> (cit. on p. 52).

- [74] Jaroslaw Kita, Sven Wiegärtner, Ralf Moos, Peter Weigand, Adele Pliscott, Marc H. La Branche, and Howard D. Glicksman. «Screen-printable type S thermocouple for thick-film technology». In: *Procedia Engineering* 120 (2015), pp. 828–831. ISSN: 18777058. DOI: 10.1016/j.proeng.2015.08.692 (cit. on p. 54).
- [75] Jerry Czarnecki. «Precision thermogravimetry». In: *Journal of Thermal Analysis and Calorimetry* 120.1 (2015), pp. 139–147. ISSN: 15882926. DOI: 10.1007/s10973-014-4384-0 (cit. on p. 56).
- [76] Prof Marta Boaro and Andrea Felli. «PRIN17 Project “ Direct Biopower ”». In: (2020) (cit. on pp. 61, 75, 78).
- [77] A. Pohar and I. Plazl. «Process intensification through microreactor application». In: *Chemical and Biochemical Engineering Quarterly* 23.4 (2009), pp. 537–544. ISSN: 03529568 (cit. on p. 61).
- [78] Carbolite Gero Ltd. *Carbolite Gero 3000°C, furnace brochure catalogue* (cit. on p. 65).
- [79] Xiao Liu, Sitian Cheng, Hong Liu, Sha Hu, Daqiang Zhang, and Huansheng Ning. «A survey on gas sensing technology». In: *Sensors (Switzerland)* 12.7 (2012), pp. 9635–9665. ISSN: 14248220. DOI: 10.3390/s120709635 (cit. on p. 66).
- [80] Harry Budiman, Nuryatini, and Oman Zuas. «Comparison between GC-TCD and GC-FID for the determination of propane in gas mixture». In: *Procedia Chemistry* 16 (2015), pp. 465–472. ISSN: 18766196. DOI: 10.1016/j.proche.2015.12.080 (cit. on p. 67).
- [81] Keith L. Bristow. «5.3 Thermal Conductivity». In: Sept. 2018, pp. 1209–1226. DOI: 10.2136/sssabookser5.4.c50. URL: <http://doi.wiley.com/10.2136/sssabookser5.4.c50> (cit. on p. 68).
- [82] Hewlett-Packard Company. *Reference Manual HP 5890 Series II and HP 5890 Series II Plus* (cit. on pp. 68, 69).
- [83] Arnold Toonen and Remko van Loon. *Hydrogen Detection with a TCD using Mixed Carrier Gas on the Agilent Micro GC*. Tech. rep. Agilent Technologies, Inc., 2013, p. 4. URL: www.agilent.com/chem/microgc (cit. on p. 69).

- [84] S. B. Twiss, D. M. Teague, J. W. Bozek, and M. V. Sink. «Application of Infrared Spectroscopy to Exhaust Gas Analysis». In: *Journal of the Air Pollution Control Association* 5.2 (Aug. 1955), pp. 75–83. ISSN: 0002-2470. DOI: 10.1080/00966665.1955.10467692. URL: <http://www.tandfonline.com/doi/abs/10.1080/00966665.1955.10467692> (cit. on pp. 70, 71).
- [85] H Jagodzinski. «H. P. Klug und L. E. Alexander: X-ray Diffraction Procedures for Polycrystalline and Amorphous Materials, 2. Auflage. John Wiley & Sons, New York-Sydney-Toronto 1974, 966 Seiten, Preis: £ 18.55.» In: *Berichte der Bunsengesellschaft für physikalische Chemie* 79.6 (June 1975), pp. 553–553. ISSN: 00059021. DOI: 10.1002/bbpc.19750790622. URL: <https://onlinelibrary.wiley.com/doi/abs/10.1002/bbpc.19750790622%20http://doi.wiley.com/10.1002/bbpc.19750790622> (cit. on p. 74).
- [86] B D Cullity. *Elements of X-ray Diffraction*. Addison-Wesley series in metallurgy and materials. Addison-Wesley Publishing Company, 1978. ISBN: 9780201011746. URL: <https://books.google.it/books?id=WpxpAAAAMAAJ> (cit. on p. 74).
- [87] C. V. Jeans. «M OORE , D. M. & R EYNOLDS , R. C., Jr. 1997. X-Ray Diffraction and the Identification and Analysis of Clay Minerals , 2nd ed. xviii + 378 pp. Oxford, New York: Oxford University Press. Price £27.95 (spiral-bound paperback). ISBN 0 19 508713 5.» In: *Geological Magazine* 135.6 (Nov. 1998), pp. 819–842. ISSN: 0016-7568. DOI: 10.1017/s0016756898501501. URL: https://www.cambridge.org/core/product/identifier/S0016756898501501/type/journal_article (cit. on p. 74).
- [88] Xiaomin Xu, Yangli Pan, Yijun Zhong, Ran Ran, and Zongping Shao. «Ruddlesden-Popper perovskites in electrocatalysis». In: *Materials Horizons* 7.10 (2020), pp. 2519–2565. ISSN: 20516355. DOI: 10.1039/d0mh00477d (cit. on pp. 75, 76).
- [89] Zhihong Du et al. «High-Performance Anode Material Sr₂FeMo_{0.65}Ni_{0.35}O_{6-δ} with in Situ Exsolved Nanoparticle Catalyst». In: *ACS Nano* 10.9 (2016), pp. 8660–8669. ISSN: 1936086X. DOI: 10.1021/acsnano.6b03979 (cit. on p. 127).

- [90] Ningning Dai, Jie Feng, Zhenhua Wang, Taizhi Jiang, Wang Sun, Jinshuo Qiao, and Kening Sun. «Synthesis and characterization of B-site Ni-doped perovskites $\text{Sr}_{2}\text{Fe}_{1.5-x}\text{Ni}_x\text{Mo}_{0.5}\text{O}_{6-\delta}$ ($x = 0, 0.05, 0.1, 0.2, 0.4$) as cathodes for SOFCs». In: *Journal of Materials Chemistry A* 1.45 (2013), pp. 14147–14153. ISSN: 20507488. DOI: 10.1039/c3ta13607h (cit. on p. 128).
- [91] Charline Arrivé, Thibaud Delahaye, Olivier Joubert, and Gilles H. Gauthier. «Study of $(\text{La},\text{Sr})(\text{Ti},\text{Ni})\text{O}_{3-\delta}$ materials for symmetrical Solid Oxide Cell electrode - Part B: Conditions of Ni exsolution». In: *Ceramics International* 46.5 (2020), pp. 5841–5849. ISSN: 02728842. DOI: 10.1016/j.ceramint.2019.11.034. URL: <https://doi.org/10.1016/j.ceramint.2019.11.034> (cit. on pp. 128–130).